The iron spin crossover in ferropericlase and its seismic effects in Earth's lower mantle

Viktoria E. Trautner

A thesis submitted for the degree of

Doctor of Philosophy

Department of Earth Sciences

University of Oxford

2025

Primary supervisor:

Professor Hauke Marquardt

Secondary supervisor:

Associate Professor Paula Koelemeijer

This work was funded by the European Union's Horizon 2020 Research and Innovation Programme (ERC Grant 864877, awarded to Hauke Marquardt)

To my grandfather Friedrich Gölly "Friedl Opa" (3. 3. 1939 – † 27. 5. 2023),*
whose love and labour for his family knew no bounds.

Acknowledgements

As with any DPhil, this thesis might bear my name on the title page, but it is the product of many people's efforts; it would not exist, were it not for the work, help and support of the people that I would like to express my gratitude to in this section.

First and foremost, I would like to thank my primary supervisor Hauke Marquardt for bringing this project to my attention in the first place and taking me on despite me having no prior experience with mineral physics whatsoever, for guidance and support throughout the DPhil and for giving me the freedom and opportunity to explore my scientific interests beyond the project. I am also deeply grateful to Paula Koelemeijer, who stepped in as my second supervisor halfway through the DPhil and provided me with much-needed and -appreciated help and guidance on the seismological aspects of the project. I sincerely appreciate my examiners, Claire Nichols and Sébastien Merkel, dedicating their time and energy to evaluating my thesis.

A big thank you to Niccolò Satta, Egor Koemets and Johannes Buchen, for taking me under their wing and teaching me all I know about preparing Diamond-Anvil Cells, performing high-pressure synchrotron experiments and analysing X-ray diffraction patterns, and also for making beamtimes a fun experience. Special thanks to Biao Wang for sharing his data analysis codes and being my DPhil buddy throughout these four years.

I'm grateful to everyone who helped to acquire the experimental data for this thesis: The Oxford group for participating in beamtimes; Alba San José Méndez, Giacomo Criniti and Alex Kurnosov for helping out when we were not allowed to travel ourselves during the pandemic; the beamline scientists at P02.2, Nico Giordano, Konstantin Glazyrin, Timofey Fedotenko and Hanns-Peter Liermann, for providing support during beamtimes. A further thank you to Andrew Matzen, Estelle Ledoux, Gareth Davies and Katharina Marquardt for assistance with micro-analysis of samples.

I also want to thank Ashim Rijal, Stephen Stackhouse, Ben Fernando, Adrian Mag and Andrew Walker for help with their respective areas of expertise in the computational Earth sciences. Not only did they provide me with insightful conversations and practical support in the aspects of my

DPhil I was least adept at, they also helped me overcome a dread of anything to do with coding – probably one of the proudest achievements of my DPhil.

A huge thank you to Nikki, Bei Bei and Annika. From providing a listening ear whenever I need it, to always being up for an adventure, I couldn't have wished for better friends to share the DPhil journey with. A heartfelt thanks also to all my other Oxford friends in- and outside the Earth Science department, who have made the last four years some of the best of my life.

Dankjulliewel lieve blubjes, voor een vriendschap die een rots is in mijn leven en ook met de Noordzee ertussen niets minder is geworden.

An meine Eltern, Silvia und Roland: Danke für eure bedingungslose Liebe und Unterstützung und euren steten Glauben an mich.

Finally, to my partner Sjef Baas – the biggest thank you of all. For leaving job, friends and family (and the EU) behind to join me in the adventure of moving to the UK (and in the middle of a pandemic at that). For experiencing all the things with me that have made our time in Oxford so special. For your patience and support during the moments of doubt and minor crises that come with doing a DPhil. For letting me go off on beamtimes and conferences and fieldtrips, and always being there when I come back home. For sharing your life with me, whatever the future may hold for us.

Abstract

In the study of Earth's deep interior, mineral physics and seismology are two principal and closely linked disciplines. Seismology allows us to image the interior structure of our planet, but the interpretation of such observations requires a detailed understanding of the elastic properties of deep Earth materials, which govern the propagation velocity of seismic waves. Experimental and computational mineral physics provide constraints on the physical properties of minerals existing at the extreme pressure and temperature conditions of Earth's interior. The second most abundant mineral in the lower mantle is the magnesium-iron oxide ferropericlase. Iron in ferropericlase undergoes a pressure-induced spin crossover, where its electronic configuration changes from a high-spin to a low-spin state, leading to marked changes to elastic properties. The objectives of this thesis are twofold: firstly, to constrain the elastic properties of ferropericlase across the iron spin crossover as a function of temperature and iron content, and secondly, to characterize the signal of the spin crossover in seismic observations.

The compressibility of ferropericlase at ambient and high temperatures is determined using novel high-pressure, high-temperature diamond-anvil cell experiments in combination with synchrotron X-ray diffraction measurements. New experimental results for different compositions are combined with literature data and machine learning techniques are utilized to predict the relationship between pressure, iron content and ferropericlase properties. In addition, the compression behaviour of ferropericlase in a multi-phase assemblage approximating lower mantle rocks is investigated. The seismic expression of the spin crossover in seismic tomography models and travel-time measurements is characterized using synthetic models and wave propagation simulations, thus providing tools for mapping of the spin crossover in the lower mantle in future studies. Evidence for the occurrence of the spin crossover in Earth's deep interior is presented through comparison of synthetic results to observational seismic data.

Table of Contents

Nomenclature

List of acronyms

AFM	Antiferromagnetic
Bg	Bridgmanite
BS	Brillouin Spectroscopy
CMB	Core-Mantle Boundary
1D/3D	1-/3-Dimensional
DAC	Diamond-Anvil Cell
dDAC	dynamic DAC
EDS	Energy Dispersive X-ray Spectroscopy
EoS	Equation of State
FIB	Focussed Ion Beam
FM	Ferromagnetic
FWHM	Full-Width at Half-Maximum
Fp	Ferropericlase
HS	High-Spin
ISLS	Impulsive Stimulated Light Scattering
IXS	Inelastic X-ray Scattering
LDA	Local Density Approximation
LLVP	Large Low Velocity Province
LS	Low-Spin
MDN	Mixture Density Network
MORB	Mid-Oceanic Ridge Basalt
MS	Mixed-Spin
MSTM	Multiple Spin Transition Method
PCA	Principal Component Analysis
pdf	probability density function
ppv	post-perovskite
PREM	Preliminary Reference Earth Model
PTM	Pressure -Transmitting Medium
RH-dDAC	Resistive-Heated dDAC
SEM	Scanning Electron Microscope
SSTM	Single Spin Transition Method
ULVZ	Ultra-Low Velocity Zone
XES	X-ray Emission Spectroscopy
XRD	X-Ray Diffraction

List of symbols

α_V	volumetric thermal expansion
C_{ij}	elastic constants
Δc	crystal field splitting parameter
δT	differential travel-time measurement
ε	normalized volume strain
E_P	spin-pairing energy
F	normalized stress
f	Eulerian strain
$\#Fe$	iron number
γ	Grüneisen parameter
G	shear modulus
ΔG	Gibbs free energy
ΔH	enthalpy difference
ΔH_{mix}	enthalpy of mixing
k_B	Boltzmann constant
K_D	partition coefficient
K_S	adiabatic bulk modulus
K_T	isothermal bulk modulus
K_0	bulk modulus at ambient P and T
m	electronic configuration degeneracy
n	low-spin fraction
P	pressure
P_{th}	thermodynamic thermal pressure
ρ	density
R; S/P	ratio of V_S and V_P variations
r	correlation coefficient
s	spin quantum number
S_{ij}	elastic compliances
S	elastic anisotropy factor
S–C	correlation between V_S and V_C variations
ΔS/ΔP	ratio of travel-time residuals of S- and P-waves
T	temperature
t	uniaxial stress component
V	unit-cell volume
V_C	bulk sound velocity
V_P	compressional/P-wave velocity
V_S	shear/S-wave velocity
V_0	unit-cell volume at ambient P and T
X	composition
X_{Fe}	iron content
x_{Fe}	iron fraction

Chapter 1. Introduction to the thesis

Earth is a dynamic, interconnected system, shaped by closely linked processes governing its interior and exterior. Mantle convection and plate tectonics control fluxes of heat and material between Earth's deep interior and the surface and atmosphere over time. After the philosophy of Herakleitos: πάντα χωρεῖ καὶ οὐδὲν μένει", δὶς ἐς τὸν αὐτὸν ποταμὸν οὐκ ἂν ἐμβαίης – *'Everything is in motion and nothing remains still, you could not step twice into the same stream'*[1]. To comprehend the evolution of our planet since its formation to its present state and how it might change in the future, understanding the dynamic processes working deep inside Earth is fundamental.

Mantle dynamics are strongly influenced by the chemical and physical properties of deep Earth materials. However, the inaccessibility of the deep interior and consequent lack of samples means that remote-sensing techniques, such as seismology, are the primary and most detailed source of information about the physical properties and structure of the mantle. The propagation velocity of seismic waves depends on the density and elastic moduli of the material through which they are passing. It follows that the interpretation of seismic observations to constrain the thermochemical structure of the deep Earth hinges on a detailed understanding of the physical properties of candidate materials at the high pressures and temperatures relevant to Earth's interior. Quantitative knowledge of such properties can be obtained through experiments or theoretical calculations (e.g. molecular dynamics and first principle (*ab initio*) methods based on density functional theory), where experimental data serve as a crucial benchmark to computations. *In situ* measurements of mineral properties at the extreme conditions prevailing in the deep interiors of planets are facilitated by ingenious high-pressure devices like diamond anvil cells (DACs), often combined with synchrotron radiation.

In this work, I investigate the elastic behaviour of the mantle mineral ferropericlase in pressure-temperature-composition (*P-T-X*) space, using high-pressure experiments in DACs combined with

[1] From Plato's *Cratylus* 402a, where he paraphrases Herakleitos. The original wording is more lyric, evoking the rhythm and sound of a flowing river: ποταμοῖσι τοῖσιν αὐτοῖσιν ἐμβαίνουσιν, ἕτερα καὶ ἕτερα ὕδατα ἐπιρρεῖ - 'On those stepping into rivers staying the same, other and other waters flow' (Fragment 12)

synchrotron X-ray diffraction (XRD), as well as machine learning methods. Particular focus lies on how the physical properties of ferropericlase are affected by the pressure-induced spin transition occurring in its iron atoms, a phenomenon I will refer to as the *spin crossover*. I further seek to characterize the seismic signature of the spin crossover and identify its signal in seismic observations, to find evidence for its occurrence in Earth's interior. This chapter serves as both introduction to the thesis and literature review. In the following sections, I provide a background on the structure and mineralogy of Earth's mantle (1.1), iron spin transitions in ferropericlase (1.2) and the spin-crossover induced changes in the elastic (1.3) and other properties of ferropericlase (1.4). In section 1.5, I state the research aims of this thesis and provide a roadmap outlining the topics covered in each chapter.

1.1. Structure and composition of Earth's mantle

The structure of Earth's mantle is commonly defined by major seismic discontinuities, with the lower mantle spanning the region between the base of the transition zone at the 670 km discontinuity and the Core-Mantle Boundary (CMB) at 2891 km (Dziewonski & Anderson, 1981). It is the largest layer of the Earth, encompassing over half of the planet by both volume and mass. As such, its compositional and thermal state and dynamic regime are of broad interest. The upper mantle is commonly accepted to consist primarily of a variety of peridotite rocks (i.e., fertile llherzolite, depleted harzburgite and cumulate-derived dunite), crosscut by subducting slabs containing oceanic crust of a Mid-Oceanic Ridge Basalt (MORB)-like composition. Conversely, the chemical composition (and compositional heterogeneity) of the lower mantle is less well-constrained and therefore a more controversial topic (Irifune & Tsuchiya, 2015).

Seismic velocity gradients of one-dimensional models for the Earth increase smoothly across the lower mantle (e.g. Dziewonski & Anderson, 1981). Only the lowermost few hundred kilometres above the CMB showing strong vertical and lateral velocity variations (the *D"* region) (Lay, 2015). As a result, the lower mantle was long considered to be largely chemically homogeneous, but growing evidence from geophysical (e.g. Garnero et al., 2016; Li et al., 2017; Rudolph et al., 2015; Waszek et al., 2018) and geochemical (e.g. Day et al., 2022; Jackson et al., 2020; Mukhopadhyay

& Parai, 2019; Walter et al., 2022) studies indicate significant lateral and vertical variations in its chemical and/or physical properties. A hypothetical primitive material coined 'pyrolite', consisting of four parts dunite to one part basalt, was proposed by Ringwood (1962) and is still considered a representative bulk composition for the mantle. Based on considerations of chemical diffusion rates and stirring times in a convecting mantle, a mechanical mixture of slab-derived basalt and harzburgite (marble-cake mantle) has been proposed as an alternative to a chemically equilibrated pyrolitic lower mantle (Allègre & Turcotte, 1986; Xu et al., 2008). Reservoirs that have remained relatively isolated since the early Hadean and preserve some primordial materials may be present at the base of the lower mantle, where they are sampled by deep mantle plumes (Day et al., 2022; Jackson et al., 2020; Mukhopadhyay & Parai, 2019). Furthermore, it has been speculated that SiO_2-rich chondritic materials, originating from intrinsically strong primordial material that resisted entrainment by mantle convection, may be present in the mid-mantle (Ballmer et al., 2017).

The phase transitions and mineral proportions in candidate compositions for lower mantle rocks (fig. 1.1) have been studied through experiments at *P-T* conditions relevant to the lower mantle. Pyrolite was found to transform from ringwoodite and majorite garnet to bridgmanite (Bg), ferropericlase (Fp) and calcium-perovskite at the top of the lower mantle (Irifune & Tsuchiya, 2015). For a pyrolitic bulk composition, ferropericlase would be the second most abundant mineral in the mantle, constituting about 18% by volume (Irifune et al., 2010). The proportion of ferropericlase in harzburgite at lower mantle depths is expected to be even greater at about 24%, while chondritic materials should host less than 10% ferropericlase and none at all is present in a MORB composition (Irifune & Tsuchiya, 2015; Valencia-Cardona et al., 2017). Bridgmanite, the most abundant phase in each of these compositions, transforms into the post-perovskite (ppv) phase near the base of the lower mantle (Murakami et al., 2004; Oganov & Ono, 2004). The complex velocity structures in the *D"* layer are commonly linked to this phase transition (e.g. Cobden et al., 2015; Hirose et al., 2017).

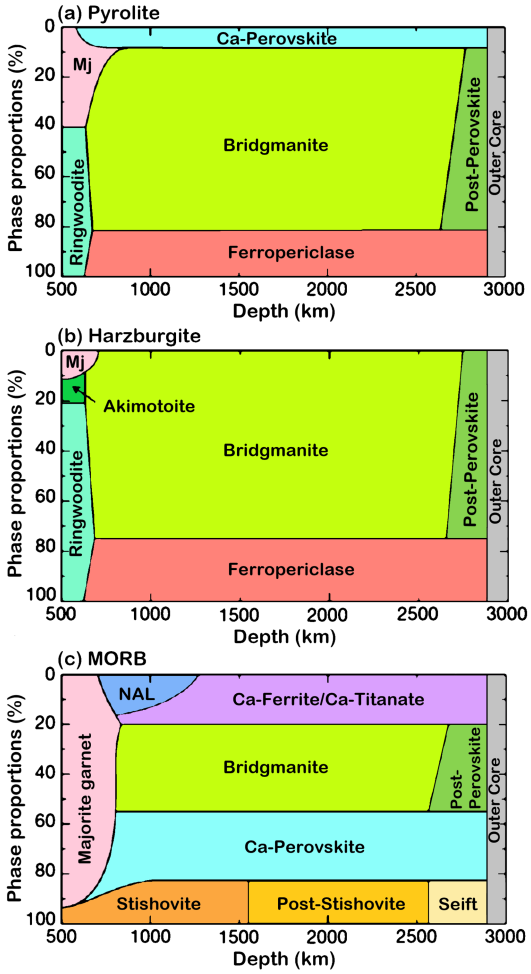

Figure 1.1 Changes in mineral proportions with depth for the compositions of a) Pyrolite, b) Harzburgite, and c) Mid-Oceanic Ridge Basalt (MORB) along a possible adiabatic geotherm. See Irifune and Tsuchiya (2015) for the chemical compositions of these three different materials, which are likely candidates for the bulk composition of lower mantle rocks and their mineralogy. *Mj* majorite garnet; *NAL* hexagonal new aluminous phase; *Seift* Seifertite. Modified from Irifune and Tsuchiya (2015).

While one-dimensional seismic velocity models of the lower mantle suggest a simple seismological structure compared to the upper mantle, increasingly detailed imaging of three-dimensional velocity variations has revealed a more complex picture (Lay, 2015). While lateral velocity variations in the lower mantle are small (a few percent), seismic tomography models have identified two antipodal large-scale seismic structures called Large Low Velocity Provinces (LLVPs) at the base of the lower mantle (Garnero et al., 2016; Koelemeijer et al., 2016). These structures are characterized by anomalously low S-wave velocities and less pronounced reductions in P-wave velocities compared to the surrounding ambient mantle. They cover about 30% of the

core surface and extend up to 1200 km above the CMB. Ultra-Low Velocity Zones (ULVZs) are smaller, localized seismic anomalies with strongly reduced S- and P-wave velocities and an increased density contrast with the ambient mantle (Li et al., 2017; Yu & Garnero, 2018). They are located just above the CMB, are commonly tens of kilometres thick and often occur on the edges of LLVPs. In addition, abundant globally discontinuous seismic reflectors have been observed in the mid-lower mantle (Waszek et al., 2018). While changes in temperature or chemistry are most often invoked to explain seismic features like LLVPs, ULVZs and mid-mantle reflectors, a number of mineralogical processes occur in lower mantle phases that may significantly affect seismic velocities and contribute to seismic heterogeneity in the lower mantle (Marquardt & Thomson, 2020). One such mineralogical feature leading to changes in seismic properties is the iron spin crossover in ferropericlase. Understanding these changes is key to a successful inversion of seismic observations to constrain the compositional and thermal state of the lower mantle.

1.2. Iron spin transition in ferropericlase

Ferropericlase refers to the solid solution series between the endmembers MgO (periclase) and $Fe_{1-\chi}O$ (wüstite), where χ indicates the non-stoichiometry of the compound (Lin et al., 2013). The name ferropericlase is often used only for the MgO-rich composition of $(Mg_{1-x}Fe_x)O$, while compositions with $x > 0.5$ are referred to as magnesiowüstite. Throughout this thesis, I will use *ferropericlase* for any intermediate composition in the solid solution series of $(Mg_{1-x}Fe_x)O$, using x_{Fe} to denote the iron fraction where relevant. At ambient pressure, ferropericlase has a B1 cubic rock-salt structure (space group $Fm\bar{3}m$), where the octahedral site is occupied by magnesium or iron atoms (fig. 1.2b). Under high pressures the cubic structure distorts to a rhombohedral state (space group $R\bar{3}m$) with lower symmetry by compression of the three cubic body diagonals (Mao et al., 2002). The distortion is more prominent in iron-rich compositions and sensitive to non-hydrostaticity (e.g. Finkelstein et al., 2017; Kantor et al., 2006). An iron content of approximately $x_{Fe} = 0.2$ is considered representative for ferropericlase in most of the lower mantle (Irifune et al., 2010; Murakami, 2005; Sinmyo & Hirose, 2013). With the concentration of Fe^{3+} typically below 1% for this composition (McCammon et al., 1998), most of the iron is expected to be ferrous. However,

the $Fe^{3+}/\sum Fe$ of ferropericlase is a function of pressure, temperature, composition and oxygen fugacity and is generally higher in iron rich compositions (Jacobsen et al., 2002; Otsuka et al., 2013). Iron partitioning with bridgmanite and post-perovskite may result in ferropericlase Fe^{3+} concentrations of 7-11% at lower mantle *P*,*T*-conditions (Sinmyo et al., 2008a).

Iron is the only transition metal out of the major elements of the bulk silicate earth, with the 3*d* orbitals partially filled by five or six electrons in Fe^{3+} and Fe^{2+}, respectively. An iron ion in the octahedral site of cubic ferropericlase is surrounded by six oxygen anions positioned along a Cartesian axis. According to crystal field theory (Burns, 1993), the five degenerate *d* orbitals of the iron ion split into two sets with different energies in this atomic environment (fig. 1.2). Two orbitals, d_{z^2} and $d_{x^2-y^2}$, are referred to as e_g and lie along the Cartesian axes. The repulsion caused by their proximity to the oxygen atoms causes them to experience an increase in energy. Contrarily, the d_{xy}, d_{xz} and d_{zy} orbitals, referred to as t_{2g}, are lower in energy, because they lie in the planes between the oxygen atoms instead of directly along a Cartesian axis (see Lin et al., 2013). The energy difference between the t_{2g} and e_g orbitals is Δc (the crystal field splitting parameter). Distribution of the available electrons over these orbitals is determined by the minimization of the competing quantities Δc and the spin-pairing energy E_p (see Badro, 2014 for a detailed discussion). At ambient conditions, Δc is low compared to E_p and it is energetically favourable for the 3*d* electrons to occupy different orbitals with the same electronic spin. Fe^{2+} will then have four unpaired electrons and two paired electrons of opposite spin, with a total spin quantum number (*s*) of 2 (since each electron has $s = ½$). Fe^{3+} will have one unpaired electron in each orbital, with $s = 2½$. This is referred to as the high-spin (HS) state, see figure 1.2b. With increasing pressure, the iron-oxygen bond length decreases, resulting in an increase of Δc, while E_p is largely independent of pressure. Once Δc becomes large enough with respect to E_p, pairing of electrons with opposite spin in the lower energy t_{2g} orbitals becomes more favourable. This is referred to as the low-spin (LS) state, where Fe^{2+} has $s = 0$ with all electrons paired, while Fe^{3+} will have $s = ½$ with one unpaired electron remaining.

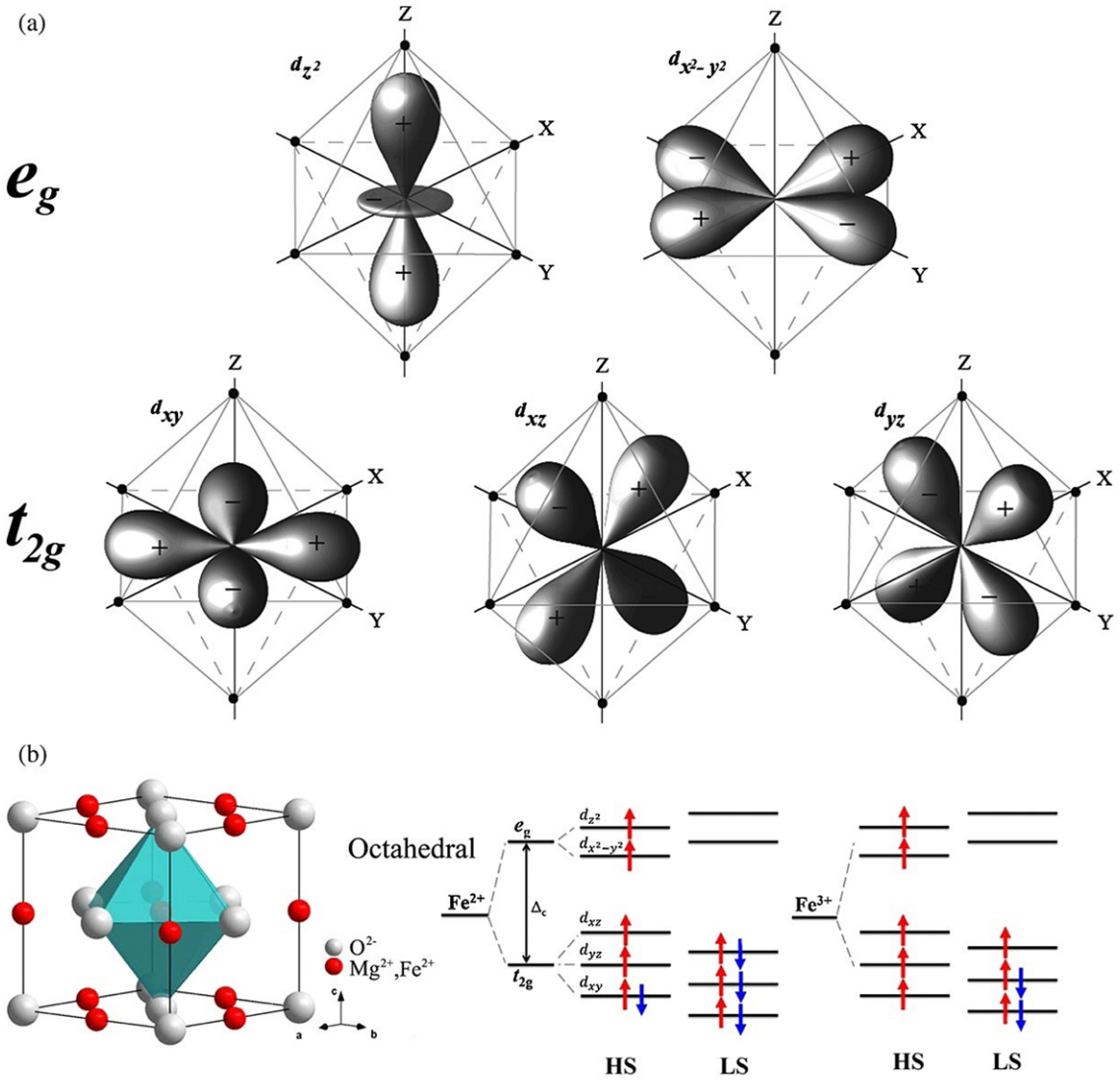

Figure 1.2 Atomic environment of iron in the octahedral site of (Mg,Fe)O ferropericlase. a) Configurations of the five partially filled *d*-orbitals of an iron ion in the octahedral site of ferropericlase, with respect to the six oxygen anions along the Cartesian axes. b) The octahedral site in the B1 face-centred cubic crystal structure with crystal field splitting diagrams for Fe^{2+} and Fe^{3+} in high-spin (HS) and low-spin (LS) state. Figure from Lin et al. (2013).

The pairing of the 3*d* electrons in an iron ion is referred to as an electronic spin pairing transition, or spin transition for short. It is coupled to a volume reduction, since the ionic radius of LS iron is smaller than that of HS iron (Shannon, 1976). The possibility of iron spin transitions in mantle minerals was first proposed by Fyfe (1960) and then observed experimentally in ferropericlase for the first time by Badro et al. (2003) with X-ray emission spectroscopy (XES). The spin transition in ferropericlase from HS to LS state occurs at pressures relevant to Earth's lower mantle, but it is not a sharp transition. As opposed to all iron atoms in ferropericlase undergoing the spin change simultaneously at a certain pressure, the fraction of LS iron increases gradually with increasing

pressure (e.g. Lin et al., 2007a; Sturhahn et al., 2005; Tsuchiya et al., 2006). We refer to the pressure range where HS and LS iron atoms coexist as the mixed-spin (MS) region and because of its continuous nature, the transition of a ferropericlase crystal from full HS to full LS state is described as a spin crossover.

To determine where in Earth's lower mantle the spin crossover is expected to occur, it is key to understand how the onset pressure and width of the spin crossover vary as a function of iron content X_{Fe} and temperature. Since the pioneering work of Badro et al. (2003) many studies have tried to shed light on these questions through high-pressure experimental investigations, as well as first principles calculations. Theoretical computations predict that the spin crossover shifts to higher pressures with increasing iron content (Muir & Brodholt, 2015; Persson et al., 2006), in agreement with experimental results from Mössbauer spectroscopy (Speziale et al., 2005). The driving force behind this effect is thought to be the smaller ionic radius of Mg^{2+} compared to HS Fe^{2+} (Shannon, 1976), resulting in an effective chemical pressure on the Fe atoms in ferropericlase, which decreases as the proportion of iron atoms increases (Speziale et al., 2005). High-temperature experimental results from XES and XRD indicate that the spin crossover broadens and shifts to higher pressure with increasing temperatures (Lin et al., 2007a; Mao et al., 2011). This is consistent with computations, which show that finite temperature effects result in a broadening of the spin crossover with temperature (Tsuchiya et al., 2006; Wentzcovitch et al., 2009), with magnetic entropy contributing strongly to a positive Clapeyron slope (Sun et al., 2022).

Holmström & Stixrude (2015) showed that non-ideal mixing of HS and LS iron broadens the spin crossover further, because the MS state is stabilized by a favourable enthalpy of mixing ΔH_{mix}. The volume difference between iron in HS and LS state allows for denser packing of HS and LS iron octahedra, resulting in the favourable ΔH_{mix}. This effect is most significant for on-axis neighbouring iron atoms, where HS iron atoms are stabilized to higher pressures with an increasing number of neighbouring LS iron atoms (Marcondes et al., 2020; Méndez et al., 2022). Consequently, the distribution of iron atoms in the crystal lattice affects the width of the spin crossover, as illustrated by different theoretical calculations for $x_{Fe} = 0.1875$: For a uniform iron

arrangement with periodic Fe-O-Fe-O sequences (i.e., only on-axis neighbours) the spin crossover is very broad (e.g. Holmström & Stixrude, 2015; Sun et al., 2022), while a configuration with only off-axis neighbouring iron atoms produces a much narrower spin crossover, and a random distribution with some on-axis neighbours, but no infinite sequences, produces a spin crossover of intermediate width (Méndez et al., 2022). The short-range ordering of the $(Mg_{1-x}Fe_x)O$ solid solution appears to be P- and T-dependent. Yang et al. (2021) showed that iron clustering occurs at temperatures below 900 K, while entropy-driven randomization of the iron distribution occurs at higher temperatures, in agreement with samples quenched from high temperature and ambient pressure exhibiting random ordering (Waychunas et al., 1994). On the other hand, Kantor et al. (2009) found that pressure strongly stabilizes iron clusters in Fe-poor (below $x_{Fe} \approx 0.2$) ferropericlase, suggesting that significant short-range order may exist at lower mantle conditions. For iron-rich compositions, we expect the favourable ΔH_{mix} to lead to a broadening of the spin crossover, because of the increasing number of on-axis neighbouring iron atoms.

Even though this thesis focusses on the spin crossover in ferropericlase, it should be mentioned that iron spin transitions at lower mantle conditions have also been observed in bridgmanite (Badro et al., 2004), in minor phases like Fe,Al-bearing phase D (Chang et al., 2013; Wu et al., 2016) and ferromagnesite (Lin et al., 2013), and in iron-rich silicate melts (Nomura et al., 2011). The spin state of iron in post-perovskite may also affect its properties, although the post-perovskite stability field in the lower mantle is narrow and spin states are not expected to change in that range (Badro, 2014; Lin et al., 2013). Bridgmanite has multiple crystallographic sites that can be occupied by iron in different valence states, with site occupancy strongly dependent on Al-content (Lin et al., 2013). This makes constraining the spin state of bridgmanite more complex than for ferropericlase (Badro, 2014). Only Fe^{3+} in the smaller octahedral B-site is thought to undergo a spin transition, but whether B-site Fe^{3+} exists in lower mantle bridgmanite is still debated (e.g. Fu et al., 2018; Mao et al., 2015; Mao et al., 2017; Okuda et al., 2020; Sinmyo et al., 2017; Zhu et al., 2020); consequently, it remains an area of active research whether lower mantle bridgmanite undergoes a spin transition and if so, whether this causes any significant changes to its properties. Since

bridgmanite is the most abundant phase in the lower mantle and its properties play a major role in mantle properties and processes, potential effects of spin transitions in bridgmanite must certainly be considered when studying the state of Earth's deep interior. However, iron is expected to preferentially partition into ferropericlase throughout the lower mantle (e.g. Piet et al., 2016), so effects of a spin transition in bridgmanite are likely less pronounced compared to the spin crossover in ferropericlase.

1.3. Spin crossover-induced changes in the elastic properties of ferropericlase

The spin crossover in ferropericlase is pressure-induced and causes a reduction in unit-cell volume, resulting from the decrease in ionic radius of iron atoms as they transition from HS to LS state. Soon after the first experimental detection of the spin transition in ferropericlase with XES (Badro et al., 2003), the accompanying volume-reduction was observed in XRD data (Lin et al., 2005) and has since been reported by numerous studies for a range of iron contents and temperatures (e.g. Chen et al., 2012; Fei et al., 2007b; Glazyrin et al., 2017; Komabayashi et al., 2010; Mao et al., 2011; Marquardt et al., 2009a; Solomatova et al., 2016; Speziale et al., 2005). Because the spin crossover occurs over a broad pressure/depth range, it does not result in a seismic discontinuity like those linked to major phase transitions in the mantle (e.g. the transformation of ringwoodite to Bg and Fp at the base of the transition zone, see fig 1.1). Instead, the effects of the spin crossover on mantle properties are expected to be gradual and spread out over hundreds of kilometres depth. Potential implications for seismological observations and geodynamic processes were considered early on, with a focus on the (relatively small, i.e., a few percent) increase in density and bulk modulus associated with the transition from full HS to full LS state (Fei et al., 2007b; Lin et al., 2007a; Speziale et al., 2007). However, it is the elastic properties of ferropericlase in mixed-spin state that are most notable and may lead to the most significant effects on seismic observables. The isothermal bulk modulus K_T is directly dependent on the unit-cell volume V and its pressure derivative, according to the thermodynamic definition:

$$K_T = -V \cdot \left(\frac{\partial P}{\partial V}\right)_T \tag{1.1}$$

Because the spin crossover occurs over an extended pressure range, the decrease in unit-cell volume is gradual and smooth, resulting in a steeper *V(P)* slope. From equation 1.1 it becomes evident that this can lead to a reduction or softening of K_T in the mixed-spin region. Both experimental (Crowhurst et al., 2008) and theoretical (Wentzcovitch et al., 2009) studies reported such an enhanced compressibility for the adiabatic bulk modulus K_S, which is related to K_T through the volumetric thermal expansion α_V and Grüneisen parameter γ:

$$K_S = (1 + \alpha_V \gamma T) \cdot K_T \tag{1.2}$$

To understand the effects of the spin crossover-induced bulk modulus softening in ferropericlase on the properties of lower mantle materials, it is important to quantify the shape, onset and magnitude of the bulk modulus softening as a function of iron content and temperature.

Theoretical computations indicate that the softening broadens and shifts to higher pressure, but decreases in magnitude with increasing temperature (Wentzcovitch et al., 2009). However, predicted spin state phase diagrams are markedly different depending on assumptions made in the calculations (Sun et al., 2022) and calibration with experimental results is thus crucial. XRD measurements have been used to investigate the effects of temperature (e.g. Mao et al., 2011) and iron content (e.g. Fei et al., 2007b) on the volume reduction of ferropericlase across the spin crossover. While equation 1.1 can in principle be used to determine the bulk modulus from the pressure-volume curve, a limited pressure resolution of *P(V)* measurements in previous studies necessitated fitting the data to fixed functional forms for HS and LS ferropericlase, with inherent biases resulting from *a priori* constraints (e.g. Chen et al., 2012; Lin et al., 2005; Mao et al., 2011; Marquardt et al., 2009a; Solomatova et al., 2016). Direct constraints on the elasticity of ferropericlase from Impulsive Stimulated Light Scattering (ISLS) and Brillouin spectroscopy (BS) have been limited to low iron contents (Crowhurst et al., 2008; Yang et al., 2015) and pressures below the onset of the spin crossover at high temperature (Yang et al., 2016). Consequently, there is a lack of experimental constraints on the bulk modulus softening of ferropericlase at high temperatures and high iron contents that can serve as benchmarks for theoretical predictions. This

is a major source of uncertainty in our understanding of the effects of the spin crossover on lower mantle properties and providing such constraints will thus be pivotal.

Seismic wave velocities, i.e., compressional (V_P), shear (V_S) and bulk sound (V_C) wave velocities, are determined by K_S, the shear modulus G and density ρ:

$$V_P^2 = \frac{K_S + \frac{4}{3}G}{\rho} \tag{1.3}$$

$$V_S^2 = \frac{G}{\rho} \tag{1.4}$$

$$V_C^2 = \frac{K_S}{\rho} \tag{1.5}$$

Since V_P and V_C depend directly on K_{sS}, they are also reduced across the spin crossover depth range, whereas both G and V_S are barely affected (Marquardt et al., 2009a; Murakami et al., 2012; Wu et al., 2013; Yang et al., 2015). Because of these contrasting effects on V_P and V_C compared to V_S, the spin crossover could potentially be detected in seismic observations by high ratios of V_S to V_P and V_S to V_C of MS ferropericlase (Marquardt et al., 2009a; Wu & Wentzcovitch, 2014; Yang et al., 2015). In addition, the maximum shear anisotropy of ferropericlase was found to increase strongly across the spin crossover, which could also significantly affect seismic observations (Marquardt et al., 2009b). Characterizing the effects of the spin crossover on geophysical observables, and using this information to identify its signal in raw seismic data (i.e., travel-time measurements) or seismic tomography are key objectives that will help to constrain the occurrence and effects of the spin crossover in the lower mantle.

Theoretical calculations indicate that the softening in K_S (and consequently V_P and V_C) is related to a softening in the elastic constants c_{11} and c_{12}, but not in c_{44} (Wu et al., 2013). While observations from optical methods, such as ISLS and MS (Crowhurst et al., 2008; Marquardt et al., 2009a; Yang et al., 2015), are consistent with the theoretical results, inelastic X-ray scattering (IXS) measurements show the opposite, i.e., softening of c_{44}, but not c_{11} and c_{12} (Antonangeli et al., 2011). These discrepancies can be traced back to the different frequencies probed by light scattering techniques (GHz) and IXS (THz), to which the spin crossover effects appear to be

sensitive (Fukui et al., 2012; Fukui et al., 2017; Lin et al., 2013). Typical seismic frequencies are much lower (i.e., ~0.01-100 Hz) and Marquardt et al. (2018) conducted pressure oscillation experiments at 1Hz to show that the bulk modulus softening is expected to affect the propagation of compressional waves in the lower mantle at these frequencies. Determining elastic moduli at seismic frequencies is important, since seismic wave velocities have been shown to be frequency-dependent (Jackson et al., 2005).

1.4. Effects of the spin crossover on other physical and chemical properties

In addition to the anomalies in the elastic properties of ferropericlase, the spin crossover leads to changes in iron partitioning and diffusion rates, as well as in rheological and transport properties (see review by Lin et al., 2013). While these effects are not the focus of this thesis, it is worth discussing them briefly to illustrate how multi-faceted and pervasive the implications of the spin crossover are for the geophysics, geochemistry and geodynamics of the deep Earth. There is a general consensus that iron partitioning between ferropericlase and bridgmanite is affected by spin transitions, although contrasting effects have been reported for Al-free versus pyrolite-like compositions (e.g. Muir & Brodholt, 2016; Murakami, 2005; Piet et al., 2016; Sinmyo et al., 2008a; Sinmyo & Hirose, 2013). Electrical conductivity of ferropericlase is sensitive to iron content (Lin et al., 2013) and decreases across the spin crossover (Lin et al., 2007b; Ohta et al., 2007; Schifferle et al., 2024). Iron diffusion is strongly enhanced in MS ferropericlase, while it is lower in the LS state compared to the HS state (Saha et al., 2011; Saha et al., 2013). Diffusion rates are an important factor in the rheology of materials, since they control deformation in both diffusion and deformation creep (Karato, 2008). As a result of a reduction in the effective activation energy for diffusion creep, the spin crossover is expected to produce a viscosity minimum in ferropericlase (Ammann et al., 2011; Wentzcovitch et al., 2009).

The bulk elastic and rheologic properties of lower mantle materials, which are crucial for the interpretation of seismic observations and modelling of geodynamic processes, depend on stress and strain partitioning between ferropericlase, bridgmanite and other constituent minerals (Karato, 2008). We may expect bridgmanite to dominate the rheological properties of lower mantle rocks

because it is the most abundant lower mantle phase (i.e., ~70%, see section 1.1) and experimental investigations suggest that it is mechanically stronger than ferropericlase (Girard et al., 2016; Immoor et al., 2022; Miyagi & Wenk, 2016). However, ferropericlase could control the strength of a polyphase aggregate in high-strain regimes through the formation of an interconnected network or alignment of the weak phase, resulting in rheological weakening and strain localization (Girard et al., 2016; Thielmann et al., 2020). This may play an important role in up- or downwelling regions, like rising plumes or subducting slabs. It should be noted, however, that measuring the strength of minerals at the low strain rates that are expected to occur naturally in the lower mantle is currently not possible. Cordier et al. (2023) used numerical modelling to show that MgO deforms more slowly than bridgmanite under mantle conditions; if this is also the case for ferropericlase, the rheology of the lower mantle is likely governed by that of bridgmanite. Nonetheless, spin-crossover induced changes in viscosity and density might lead to an acceleration in mantle flow at the depths where ferropericlase is present in MS state (Marquardt & Miyagi, 2015).

All this serves to show that, besides quantifying the effects of the spin crossover on ferropericlase properties, understanding where in the lower mantle the spin crossover is expected to occur (i.e., mapping it out as a function of P, T and X_{Fe}) is crucial to understanding the geophysical and geochemical properties of the mantle, to modelling geodynamic processes and to interpreting seismic observables. Seismic observations provide the most detailed information on Earth's deep interior and the anomalous elastic behaviour of ferropericlase across the spin crossover may produce a distinctive signature that could be used to constrain the spin state of the mantle. Therefore, constraining the shape and width of the spin crossover-induced bulk modulus softening in P-T-X space must be considered a priority.

1.5. Aims and roadmap to the thesis

Resolving the thermo-chemical structure of the lower mantle is a complex task, depending on both the quantity and quality of seismic observations, as well as a detailed knowledge of mineral and rock properties. Understanding the effects of the spin crossover in ferropericlase on lower mantle

seismology is a crucial piece of the puzzle, which this thesis aspires to contribute to. To this end, the following aims are formulated:

1) To constrain the effect of temperature on the elastic behaviour of ferropericlase across the iron spin crossover;
2) To constrain the effect of iron content on the elastic behaviour of ferropericlase across the iron spin crossover;
3) To investigate stress-strain partitioning in a polycrystalline aggregate of bridgmanite and ferropericlase and how this affects the iron spin crossover;
4) To characterize the signature of the spin crossover in seismic tomography models and quantify its effect on seismic travel-time measurements;
5) To detect the signal of the spin crossover in seismic observations and provide evidence for its occurrence in Earth's lower mantle.

This thesis contains four data chapters, each addressing one or more of the stated aims. Because this thesis is presented in an integrated format, each chapter has been written as a stand-alone article and the contents have either been published, submitted for publication or are being prepared for submission. Therefore, each chapter contains individual introduction, methodology, results, discussion and conclusion sections and no separate methods chapter is included. A cover page for each chapter provides information on the state of publication and lists author contributions. The final chapter of this thesis is intended as a synthesis chapter, where the key findings from each data chapter are summarized, over-arching conclusions are drawn and directions for future work are outlined.

The topics covered in each data chapter are summarized here:

> **Chapter 2** *Compressibility of ferropericlase at high-temperature: evidence for the iron spin crossover in seismic tomography*

This chapter presents experimental results on the bulk modulus softening in $(Mg_{0.8}Fe_{0.2})O$ at room temperature and high temperatures, which serve as a benchmark for complementary theoretical

computations. The results are used to construct synthetic seismic tomography models, permitting characterisation of the spin crossover signal in global seismic tomography. The synthetic models are compared to data-based models to find evidence for the spin crossover in the Earth's mantle.

Chapter 3 *Seismic signal of the iron spin crossover in travel-time data*

This chapter examines the expected seismic expression of the spin crossover in seismic data using synthetic waveforms. One-dimensional synthetic velocity profiles along different temperature gradients, derived from tomography models presented in Chapter 2, serve as input for global seismic wave propagation simulations. The effect of the spin crossover on travel-times of different seismic phases is characterized and compared to observational data. Furthermore, the temperature sensitivity of the signal is investigated and its potential to map spin state and temperature variations in Earth's mantle is considered.

Chapter 4 *Iron content-dependence of ferropericlase elastic properties across the spin crossover from novel experiments and machine learning*

In this chapter, the effect of iron content on the spin crossover is investigated. New time-resolved compression data on $(Mg_{0.6}Fe_{0.4})O$ and $(Mg_{0.4}Fe_{0.6})O$ are combined with experimental data from literature on $(Mg_{1-x}Fe_x)O$ with x_{Fe} = 0.04–0.6. A neural network-based approach is utilized to infer the relationship between ferropericlase elastic properties, pressure and iron content across the spin crossover. Implications for seismic heterogeneities in the lowermost mantle are considered.

Chapter 5 *Compression behaviour of a polycrystalline assemblage of bridgmanite and ferropericlase at lower mantle temperatures*

This chapter presents compression experiments at ambient and high temperature of a sintered polycrystal of bridgmanite and ferropericlase, that is representative of lower mantle rocks. The elastic behaviour of both minerals in the two-phase aggregate is compared to single phase results to investigate the effects of stress-strain partitioning in multi-phase materials, with a particular focus on the spin crossover in ferropericlase.

Chapter 2. Compressibility of ferropericlase at high-temperature: evidence for the iron spin crossover in seismic tomography

Preface

The contents of this chapter have been published in:

1) Méndez, A. S. J., Stackhouse, S., Trautner, V., Wang, B., Satta, N., Kurnosov, A., Husband, R., Glazyrin, K., Liermann, H. P. & Marquardt, H. (2022). Broad elastic softening of (Mg,Fe)O ferropericlase across the iron spin crossover and a mixed-spin lower mantle. *Journal of Geophysical Research: Solid Earth*, *127*(8), e2021JB023832. https://doi.org/10.1029/2021jb023832
2) Trautner, V. E., Stackhouse, S., Turner, A. R., Koelemeijer, P., Davies, D. R., Méndez, A. S. J., Satta, N., Kurnosov, A., Liermann, H.-P. & Marquardt, H. (2023). Compressibility of ferropericlase at high-temperature: Evidence for the iron spin crossover in seismic tomography. *Earth and Planetary Science Letters*, *618*(118296. https://doi.org/10.1016/j.epsl.2023.118296

In particular, this chapter contains experimental results at room temperature that were reported in Méndez et al. (2022), as well as high-temperature experiments, theoretical computations and synthetic seismic tomography models that were presented in Trautner et al. (2023). My contributions to Méndez et al. (2022) consist of processing and analysis of the experimental data. My contributions to Trautner et al. (2023) include data processing and analysis, data visualization and writing of the original draft. Both sets of experiments were conducted before the start of my DPhil by co-authors. The theoretical computations and the synthetic tomography models, and corresponding figures, were produced by Stephen Stackhouse and Paula Koelemeijer, respectively.

Supplementary material for this chapter is included in Appendix A. Data tables and additional information on the theoretical computations are available through the supplementary material included with the online versions of the publications. Funding bodies and acknowledgements may also be found with the articles.

Abstract

The iron spin crossover in ferropericlase, the second most abundant mineral in Earth's lower mantle, causes changes in a range of physical properties, including seismic wave velocities. Understanding the effect of temperature on the spin crossover is essential to detect its signature in seismic observations and constrain its occurrence in the mantle. Here, we report the first experimental results on the spin crossover-induced bulk modulus softening at high temperatures, derived directly from time-resolved X-ray diffraction measurements during continuous compression of $(Mg_{0.8}Fe_{0.2})O$ in a resistive-heated dynamic diamond-anvil cell. We present new theoretical calculations of the spin crossover at mantle temperatures benchmarked by the experiments. Based on our results, we create synthetic seismic tomography models to investigate the signature of the spin crossover in global seismic tomography. A tomographic filter is applied to allow for meaningful comparisons between the synthetic models and data-based seismic tomography models, like SP12RTS. A negative anomaly in the correlation between S-wave and bulk sound velocity variations (S-C correlation) is found to be the most suitable measure to detect the presence of the spin crossover in tomographic models. When including the effects of the spin crossover, the misfit between the synthetic model and SP12RTS is reduced by 63%, providing strong evidence for the presence of the spin crossover, and hence ferropericlase, in the lower mantle. Future improvement of seismic resolution may facilitate a detailed mapping of spin state using the S-C correlation, providing constraints on mantle temperatures, by taking advantage of the temperature sensitivity of the spin crossover.

2.1. Introduction

$(Mg_{1-x}Fe_x)O$ ferropericlase is the second most abundant mineral in a pyrolitic lower mantle, constituting approximately 18% by volume (Irifune et al., 2010). Under pressures relevant to the lower mantle, the iron atoms in ferropericlase gradually undergo a spin-pairing transition from high-spin (HS) to low-spin (LS) state, where *d* electrons are redistributed over atomic orbitals (Badro et al., 2003). As a result, the ionic radius of iron is reduced and the unit-cell volume of ferropericlase decreases, causing an anomalous softening of the bulk modulus across the spin crossover (Crowhurst et al., 2008; Fei et al., 2007b; Lin et al., 2005; Marquardt et al., 2009a; Marquardt et al., 2018; Méndez et al., 2022; Solomatova et al., 2016; Wentzcovitch et al., 2009; Wu et al., 2013; Yang et al., 2015). The spin crossover-induced bulk modulus softening has been reported to cause major changes in a wide range of properties of ferropericlase that are relevant for large-scale geophysical processes (Lin et al., 2013). Therefore, detecting the signature of the spin crossover in seismic observations and constraining its occurrence and distribution in the lower mantle is of vital importance to improve geodynamic models and constrain chemical heterogeneity in the mantle. In an ideal case, it would be possible to construct three-dimensional (3D) maps of lateral and vertical variations in the spin state of ferropericlase based on seismic tomography.

The enhanced compressibility of ferropericlase in the mixed-spin (MS) region causes a drop in P-wave (V_P) and bulk sound velocities (V_C), while no substantial effect of the spin crossover on the shear modulus (G) and S-wave velocities (V_S) has been reported (Marquardt et al., 2009a; Murakami et al., 2012; Wu et al., 2013; Yang et al., 2015). Consequently, a high ratio of V_S to V_P and negative correlation between V_S and V_C are seen as characteristic features of the spin crossover, that might allow for its detection in seismic observations (Marquardt et al., 2009a). However, the depth, broadness and shape of the iron spin crossover are not yet well-constrained at temperatures of the lower mantle, hampering a robust detection by seismic methods. Previous experimental studies at high temperature did not measure the bulk modulus of ferropericlase directly, but had to rely on assumptions about its behaviour across the spin crossover (Mao et al., 2011) or have been limited to low iron contents and pressures below the onset of the spin crossover (Yang et al., 2016).

While theoretical calculations generally predict that the spin crossover broadens and shifts to higher pressures with increasing temperature (Holmström & Stixrude, 2015; Sun et al., 2022; Tsuchiya et al., 2006; Wentzcovitch et al., 2009; Wu et al., 2013), a verification of different computational predictions has been hampered by the absence of an experimental benchmark. Calculated spin state phase diagrams show major differences depending on the assumptions made, leading to significant uncertainties in any attempt to detect the spin crossover signature in seismic observables (e.g. Sun et al., 2022).

Nevertheless, first efforts to identify the spin crossover signal in seismological models have been reported (Cammarano et al., 2010; Kennett, 2021; Shephard et al., 2021). In particular, recent work by Shephard et al. (2021) takes advantage of the differing effects of the spin crossover on P- and S-wave velocities, suggesting that the spin crossover might be detectable in cold parts of the lower mantle. However, in addition to the current mineral physics uncertainties, the seismic tomography models investigated in the previous work lack internal consistency and realistic seismic resolution has not been accounted for.

Here, we present new experimental results of the bulk modulus softening of $(Mg_{0.8}Fe_{0.2})O$ ferropericlase across the spin crossover at room temperature, as well as the first direct experimental determination at high temperature. We further present a new theoretical model that reproduces both room- and high-temperature experimental results, allowing us to robustly predict the signature of the spin crossover at relevant mantle temperatures. We use these experimentally-verified computations to convert the 3D temperature variations predicted by a geodynamic model to high-resolution maps of seismic velocity variations in the lower mantle. By applying a tomographic filter, we are able to directly compare the results from our synthetic tomography model to tomographic model SP12RTS (Koelemeijer et al., 2016), a joint P- and S-wave model. We demonstrate that the fit between the synthetic model and SP12RTS is improved when the effects of the spin crossover in ferropericlase are included. Our study thus provides strong indications that the spin crossover in ferropericlase occurs in the Earth's mantle and that lateral and vertical variations in spin state may be investigated using seismic tomography models.

2.2. Materials and methods

2.2.1. Experiments at high pressure and temperature

2.2.1.1. Continuous compression with time-resolved X-ray diffraction

Powder of $(Mg_{0.8}Fe_{0.2})O$ was synthesized from stoichiometric mixtures of reagent grade MgO and Fe_2O_3, treated in a gas-mixing furnace at 1,250°C at an oxygen fugacity 2 log units below the fayalite-magnetite-quartz buffer (Marquardt & Miyagi, 2015). Platinum powder was mixed with the sample as pressure marker and this mixture was loaded in two diamond-anvil cells (DACs) with 150 μm culet size diamonds (RH1 and RH2), as well as a DAC with 200 μm anvil culets (GL1). Rhenium gaskets with inserts of $Fe_{0.79}Si_{0.06}B_{0.15}$ metallic glass were used to avoid parasitic Re peaks (Dong et al., 2022). Neon was loaded as pressure-transmitting medium (PTM) using the gas-loading setup at beamline P02.2 at PETRA III, DESY, Germany (Liermann et al., 2015) in cell GL1 for measurements at room temperature. In RH1 and RH2 no PTM was used, due to experimental difficulties in using a gas PTM at the high temperatures of our experiments and the fact that additional strong XRD reflections from a solid medium would complicate analysis of the data. A dynamic DAC (dDAC), driven by a piezoelectric actuator (Jenei et al., 2019), and resistive-heated dDAC (RH-dDAC) setup, developed at beamline P02.2 at PETRAIII, DESY, Germany (Méndez et al., 2020) were employed to continuously compress ferropericlase across the spin crossover pressure range. During compression, time-resolved X-ray diffraction measurements were conducted, which allowed us to collect quasi-continuous volume-pressure data. The compression experiments were performed at P02.2 using monochromatic synchrotron X-ray radiation with a fixed wavelength of 0.4836 Å. A fast GaAs 2.3 LAMBDA detector (Pennicard et al., 2018) was employed to collect diffraction images with single image exposure times of 200 ms, capturing about 20% of the Debye-Scherrer diffraction rings (fig. 2.1a).

Two types of experiments were conducted (fig. 2.2): (1) Continuous compression along a pre-programmed pressure ramp (e.g. Méndez et al., 2020), and (2) pressure cycling over a limited pressure interval (Marquardt et al., 2018). Details of each experimental run are provided in table 2.1. A single continuous compression ramp at 300 K from about 33 to 97 GPa with a maximum

compression rate of 1.2 GPa/s was measured in cell GL1. In cell RH1, a total of three ramp experiments were measured at ~900 K. Single diffraction images were collected every ~50 K during heating to target temperature and the sample was cooled down to room temperature between ramps. During heating before the third ramp, 3.5 sinusoidal pressure oscillations of 0.2 Hz were applied to the sample at temperatures between 300 K and 900 K in steps of approximately 50 K. A total of 100 datapoints was measured in each pressure cycling experiment, with the first 15 points collected before pressure cycling commenced. The amplitude of the cycling is related to the voltage applied to the piezo-actuator and the tightness of the cell and varied from 0.9 to 2.9 GPa. A single compression ramp was measured at ~1100 K in cell RH2. The cell was then cooled down to room temperature and heated again to 1450 K, while pressure cycling measurements with amplitudes of 1-19 GPa were conducted every ~50 K. Maximum compression rates during high-temperature ramp experiments ranged from 0.17 GPa/s to 0.3 GPa/s and pressure increased by 16-34 GPa in each ramp, together covering pressures between 33 GPa and 105 GPa. Temperature measurements before and after each run from two type-R thermocouples mounted close to the tips of the diamonds were used to estimate temperature variations during the experimental run, which were less than 3%.

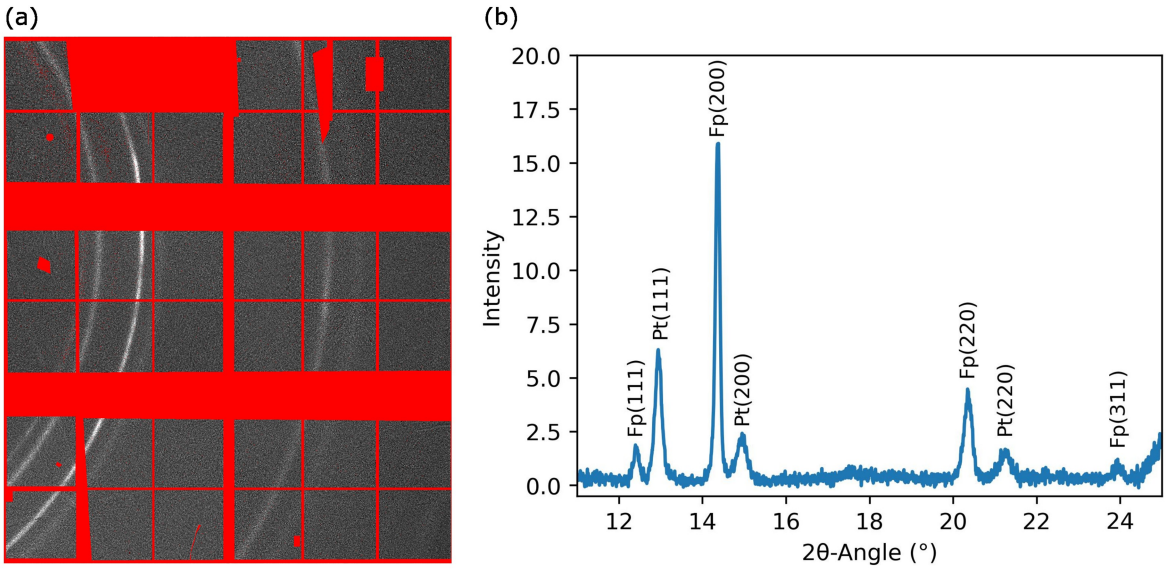

Figure 2.1 Example of raw X-ray diffraction data collected on a LAMBDA detector. a) Diffraction image collected after 200 ms exposure. A mask is applied (red) before integrating the image. b) Integrated diffraction pattern, showing labelled peaks of ferropericlase and platinum that were used to calculate volume and pressure.

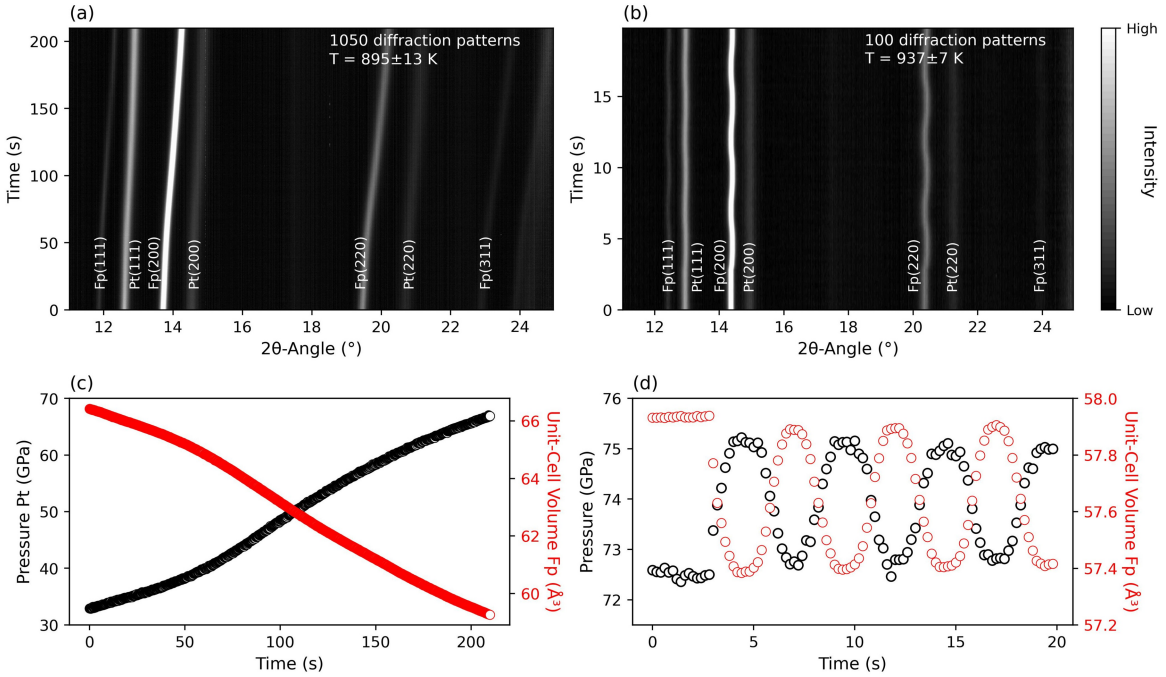

Figure 2.2 Examples of pressure ramp (a, c) and pressure cycling (b, d) experiments on $(Mg_{0.8}Fe_{0.2})O$ ferropericlase and platinum powders, measured in the RH-dDAC. a) and b) show contour plots consisting of stacked diffraction patterns, with labels indicating the *hkl* indices of the diffraction peaks of ferropericlase (Fp) and platinum (Pt). c) and d) show how the pressure derived from platinum and the unit-cell volume of ferropericlase change over the course of the experiments.

Table 2.1 Summary of experimental runs

Experiment	DAC	*T* (K)	u (*T*)*	Nr of patterns	Starting *P* (GPa)	*P* range (GPa)	Max. compression rate (GPa/s)
Ramp 0	GL1	300	-	338	33.1	63.9	1.3
Ramp 1	RH 1	895	13.0	1050	32.9	34.2	0.30
Ramp 2	RH 1	927	6.4	1050	58	16.5	0.17
Ramp 3	RH 1	894	3.8	1050	64.9	16	0.18
Ramp 4	RH 2	1131	35.5	1050	74.7	29.9	0.22
Osc 1	RH 1	300	-	100	52.9	1.2	0.46
Osc 2	RH 1	300	-	100	54.0	1.0	0.41
Osc 3	RH 1	325	1.7	100	54.6	0.9	0.36
Osc 4	RH 1	378	1.8	100	55.2	1.0	0.38
Osc 5	RH 1	433	3.8	100	55.9	1.0	0.38
Osc 6	RH 1	479	4.8	100	56.5	1.0	0.40
Osc 7	RH 1	530	6.0	100	57.2	0.9	0.36
Osc 8	RH 1	581	6.5	100	57.9	1.0	0.40
Osc 9	RH 1	624	6.3	100	58.5	1.2	0.48
Osc 10	RH 1	671	6.0	100	59.3	1.1	0.44
Osc 11	RH 1	734	5.3	100	60.2	1.2	0.47
Osc 12	RH 1	777	6.0	100	60.5	1.2	0.47
Osc 13	RH 1	819	6.5	100	61.6	1.1	0.44
Osc 14	RH 1	867	7.8	100	62.3	1.4	0.54
Osc 15	RH 1	927	6.4	100	65.0	2.2	0.88
Osc 16	RH 1	937	6.5	100	72.4	2.9	1.15
Osc 17	RH 1	971	6.5	100	72.7	2.8	1.11
Osc 18	RH 1	1021	7.5	100	72.9	2.9	1.16
Osc 19	RH 1	1070	13.8	100	73.8	2.7	1.10
Osc 20	RH 2	300	-	100	92.4	1.1	0.43
Osc 21	RH 2	327	6.8	100	92.6	1.0	0.40
Osc 22	RH 2	388	7.3	100	93.1	1.9	0.75
Osc 23	RH 2	392	7.0	100	93.2	2.6	1.02
Osc 24	RH 2	443	8.0	100	93.5	2.8	1.12
Osc 25	RH 2	502	10.3	100	94.1	2.6	1.05
Osc 26	RH 2	566	10.8	100	94.7	3.4	1.36
Osc 27	RH 2	592	11.3	100	94.9	3.3	1.33
Osc 28	RH 2	672	14.3	100	95.7	3.1	1.25
Osc 29	RH 2	727	15.3	100	96.7	3.1	1.22
Osc 30	RH 2	759	15.5	100	96.9	3.1	1.26
Osc 31	RH 2	811	17.5	100	97.7	3.1	1.24
Osc 32	RH 2	859	18.3	100	98.4	2.9	1.17
Osc 33	RH 2	910	17.8	100	99.2	3.4	1.36
Osc 34	RH 2	952	13.5	100	100.6	3.2	1.30
Osc 35	RH 2	1000	8.8	100	101.6	3.5	1.40
Osc 36	RH 2	1044	2.0	100	102.3	4.1	1.63
Osc 37	RH 2	1070	4.5	100	103.2	4.3	1.73
Osc 38	RH 2	1133	11.0	100	104.1	4.8	1.90
Osc 39	RH 2	1128	14.3	100	103.2	4.9	1.97
Osc 40	RH 2	1180	17.8	100	106.9	11.4	4.54
Osc 41	RH 2	1392	24.3	100	115.5	16.0	6.40
Osc 42	RH 2	1430	19.3	100	118.7	15.6	6.25
Osc 43	RH 2	1436	6.5	100	112.8	19.3	7.74

*u (*T*) refers to the uncertainty in temperature of each run, estimated from four temperature measurements taken before and after the run, on either side of the gasket.

2.2.1.2. Data processing and analysis

The program Dioptas (Prescher & Prakapenka, 2015) was used to integrate and background-correct diffraction images (fig. 2.1b). A Python code for batch-processing of time-resolved diffraction data (Wang, 2022) was used on the integrated data to extract the peak positions of ferropericlase and platinum. The average unit-cell volume of platinum from the $(111)_{Pt}$, $(200)_{Pt}$ and $(220)_{Pt}$ reflections, weighted by the uncertainty of the peak-fit, was used to derive pressure, employing previously published third-order Birch-Murnaghan Equation of State (EoS) parameters (Fei et al., 2007a). Similarly, the unit-cell volume of ferropericlase was derived from the weighted average of the $(111)_{Fp}$, $(200)_{Fp}$ and $(220)_{Fp}$ reflections. Line-shift analysis of the utilized reflections (Singh & Takemura, 2001) showed that the differential stresses present during the ramp experiment measured in cell RH2 at 1100 K were high compared to the other experiments (see appendix A.1 and fig. A.1). We found that the volumes derived from the $(111)_{Fp}$ and $(220)_{Fp}$ reflections are closest to the volumes measured during the pressure oscillation experiments at the same temperature and under lower stress conditions. Therefore, we chose to use the weighted average of the volumes from the $(111)_{Fp}$ and $(220)_{Fp}$ reflections only for the ramp at 1100 K. Uncertainties in pressure and unit-cell volume of ferropericlase were estimated from the difference between diffraction lines.

The smooth nature and high pressure-resolution of the compression ramps permits direct calculation of the isothermal bulk modulus (K_T) by numerical differentiation, according to its thermodynamic definition: $K_T = -V \cdot \frac{\partial P}{\partial V}\Big)_T$ (Méndez et al., 2021). K_T is calculated from the slope of a linear fit to measured volumes V as a function of pressure, i.e., $V(P)$, that fall in a chosen pressure interval around the target pressure (fig. 2.3). The error in K_T is propagated from the uncertainty in V and the standard error of the slope of the linear fit. When choosing the pressure interval, there is a trade-off between the uncertainties in the derived bulk moduli and the effective pressure resolution (fig. 2.4). We chose to use an interval of 5 GPa, which is large enough to encompass the uncertainties in pressure of the $V(P)$ data. Following Marquardt et al. (2018), the $V(P)$ data collected during pressure cycling at seismic frequencies was also used to calculate the

bulk modulus at each temperature step. A linear regression was applied to the 100 datapoints collected at each temperature to derive the slope of the $V(P)$ curve and the volume V at the average pressure, which were then used to calculate the bulk modulus. The quality of the diffraction images collected during pressure cycling experiments Osc 20 & 21 in RH2 was not sufficient to extract a reliable bulk modulus value from the $V(P)$ data because the uncertainty in the pressures of the individual datapoints was larger than the range over which pressure was cycled (fig. A.2).

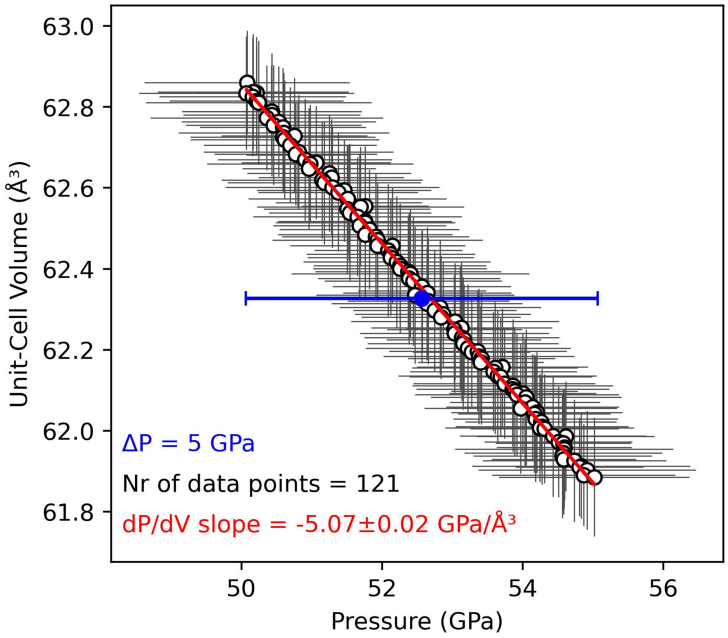

Figure 2.3 Unit-cell volume of ferropericlase as a function of pressure for data points from ramp 1 in a 5 GPa pressure interval around the blue point. The slope from a linear regression line (red) was used to calculate the isothermal bulk modulus value corresponding to the central point.

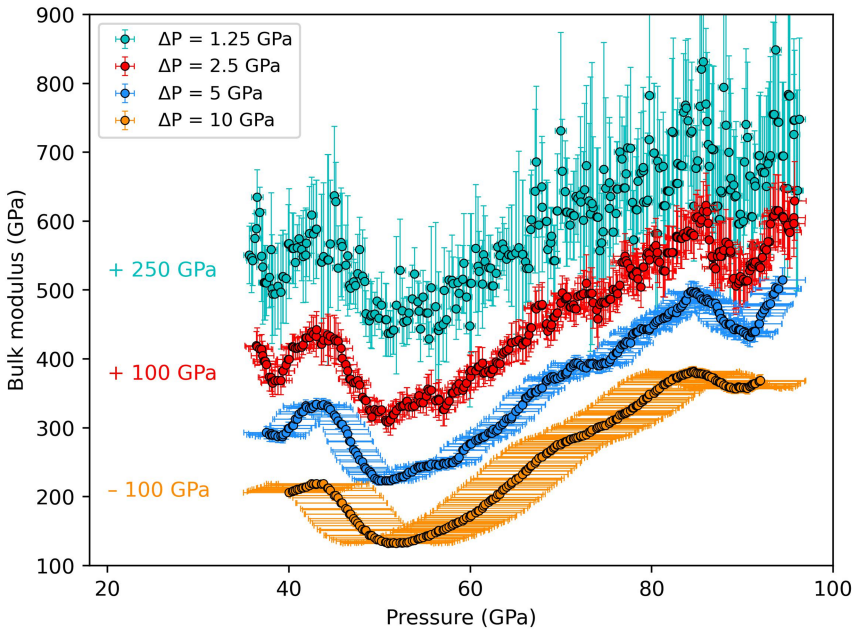

Figure 2.4 Bulk modulus curves derived from the pressure-volume data from ramp 0, using different pressure intervals for the linear regression. If a larger pressure interval is used, the uncertainty in the bulk modulus value decreases, but the pressure resolution decreases too. Curves are shifted up or down for clarity, as indicated by the numbers on the left.

2.2.2. Ab-initio calculations

Two types of theoretical calculations were performed: (1) lattice dynamics calculations to determine the difference in the static and vibrational free energy of ferropericlase in different spin states, allowing calculation of the spin crossover, and (2) molecular dynamics simulations to determine the elastic properties of ferropericlase in a fixed high or low-spin state. Both sets of results were combined to estimate the properties of ferropericlase through the spin crossover. For all calculations we used the Vienna Ab-initio Simulation Package (Kresse & Furthmüller, 1996a, b) employing the projector augmented wave method (Blöchl, 1994; Kresse & Joubert, 1999), within the framework of density functional theory. The local density approximation (LDA) (Perdew & Zunger, 1981) was used for the exchange-correlation functional. In order to describe the correlated *d* electrons of iron in ferropericlase, we utilized the LDA+U scheme of Dudarev et al. (1998), in which only the difference between onsite Coulomb interaction parameter U and onsite exchange parameter J is meaningful. In the present work, we used U - J = 3.3 eV, which was found to lead to the best agreement with experimental values for the spin crossover pressure in ferropericlase at 300 K (Méndez et al., 2022), and is similar to the 3.0 eV used in other studies of

the spin crossover (Muir & Brodholt, 2015). Since the LDA is known to underestimate pressure, we calculated a correction using the method outlined by Oganov et al. (2001), including the thermal pressure term calculated from our lattice dynamics calculations. The correction was calculated to be +3.5 GPa, based on the ambient condition volume of 76.1 Å^3 reported by Lin et al. (2005). This correction is applied to our high-temperature results (both lattice dynamics and molecular dynamics) before their use in the synthetic tomography models.

2.2.2.1. Approach to spin transition calculations

In their pioneering work, Tsuchiya et al. (2006) and Wentzcovitch et al. (2009) calculated the fraction of LS iron in ferropericlase from an expression similar to:

$$n(P,T) = \frac{1}{1+m(2s+1)\left(\frac{\Delta G_{HS-LS}(P,T)}{k_B x_{Fe} T}\right)}, \quad (2.1)$$

where m is the electronic configuration degeneracy for HS iron (m = 3 for HS and m = 1 for LS), s is the spin quantum number for HS iron (s = 2 for HS and s = 0 for LS), $\Delta G_{HS-LS}(P,T)$ is the difference between the static and vibrational components of the Gibbs free energy of the high- and low-spin states, x_{Fe} is the fraction of iron, and k_B is the Boltzmann constant. This derivation assumes ideal mixing of high- and low-spin ions. We will refer to this approach as the single spin transition method (SSTM), since it only involves calculation of $\Delta G_{HS-LS}(P,T)$ for a single transition (from full HS to full LS). This method tends to lead to a spin crossover that is narrower at ambient temperature than experimental results (Méndez et al., 2022).

Later work by Holmström and Stixrude (2015) demonstrated that favourable enthalpy of mixing of high- and low-spin ions leads to a broader spin crossover. Further studies have proposed alternative methods, which include a non-ideal mixing model, with and without the contribution of magnetic entropy (Sun et al., 2022). Building on this, we recently showed that good agreement is obtained with ambient temperature experimental results if, rather than assuming ideal mixing of high- and low-spin states, one calculates the series of successive spin transitions between stable spin states, from high- to low-spin (Méndez et al., 2022). In this method, equation 2.1 is applied to each individual spin transition, where $\Delta G_{HS-LS}(P,T)$ is now the difference between the static and

vibrational components of the Gibbs free energy of the higher and lower spin states and X_{Fe} is the fraction of iron weighted by the fraction of iron involved in the spin transition. The overall n value for a model is then a weighted average of the n values for the individual spin transitions, where the weights are the fraction of iron atoms in the model involved in the successive spin transitions. We will refer to this approach as the multiple spin transition method (MSTM), as it requires the calculation of $\Delta G_{HS-LS}(P,T)$ for multiple spin transitions.

Preliminary calculations showed that differences in the results of the SSTM and MSTM are only significant at low temperature (<1,000 K), where it is possible for a spin transition in one particular iron atom to finish before it begins in another. Experimental results at 300 K are reproduced best by the MSTM. At lower mantle temperatures (ranging from approximately 1,800 K at the top of the lower mantle to 4,000 K at the core-mantle boundary), both methods lead to similar results, since all iron atoms are undergoing a spin transition and so the order of the spin transitions is irrelevant. Here, we chose to use the MSTM to compare with experimental results between 300 K and 1450 K, since the MSTM is expected to reproduce results below 1,000 K better than the SSTM.

2.2.2.2. Spin state calculations

Prior to performing lattice dynamics calculations, we investigated the effect of model size and arrangement of iron atoms on the spin crossover. Based on the results, we selected a 216-atom ferropericlase model with a $(Mg_{0.8148}Fe_{0.1852})O$ composition (i.e., 20 iron atoms in the model) for our production calculations. This model is larger than those in our previous work (Méndez et al., 2022), allowing on-axis iron atom neighbour pairs, while avoiding infinite repeating sequences of Fe and O atoms, arising from finite-size effects associated with the use of periodic boundary conditions. The latter was shown to have a non-negligible effect on the calculated spin crossover (Méndez et al., 2022). In accordance with the observations of Waychunas et al. (1994), the positions of the iron atoms were chosen at random. Since it was not feasible to calculate the vibrational free energy for all possible spin states for a 216-atom model, we first calculated the stable mixed-spin states between the high- and low-spin states at 0 K, neglecting the vibrational

free energy contribution, and used those to compute the fraction of LS iron. Lattice dynamics calculations were then performed to calculate the vibrational free energy for only the stable mixed-spin states at 0 K.

2.2.2.3. Elastic constants of ferropericlase

Molecular dynamics simulations were used to calculate the elastic properties, as opposed to lattice dynamics calculations, for two reasons: molecular dynamics simulations account for all anharmonic effects, which may become important at lower mantle temperatures; and the large cell used in the lattice dynamics calculations made calculating elastic constants using lattice dynamics prohibitively computationally expensive. Preliminary calculations showed that the elastic properties of ferropericlase are less sensitive to magnetic state and arrangement of iron than the spin crossover, permitting the use of a smaller 64-atom model for molecular dynamics simulations. The model used has a $(Mg_{0.8125}Fe_{0.1875})O$ composition (i.e., 6 iron atoms in the model) and an arrangement of iron atoms identical to the symmetric model used in our previous work (Méndez et al., 2022).

High-temperature elastic constants were calculated for ferropericlase, fixed in a HS and LS state, from molecular dynamics simulations (NVT ensemble) using the Nosé thermostat to maintain constant temperature (Nosé, 1984). Isothermal and adiabatic elastic properties were calculated at 4 pressures and 6 temperatures. To predict elastic constants at other pressures and temperatures a weighted linear least-squares fit was made to values at the same temperature to determine values at the desired temperature and then values at the two nearest pressures points were used to interpolate or extrapolate to the desired pressure. To predict densities at other pressures and temperatures a weighted linear least-squares fit was made to values at the same temperature, to determine four values at the desired temperature, and these were then fit using a second-order Birch-Murnaghan equation of state (Birch, 1947; Murnaghan, 1944). To calculate the elastic constants of ferropericlase through the spin crossover, we used the equations derived by Wu et al. (2013) with the low spin fractions obtained from our lattice dynamics calculations.

2.2.3. Synthetic tomography models

To understand the effect of the iron spin crossover in ferropericlase on global seismic tomography, specifically its effect on the relationships between seismic velocities, we constructed synthetic seismic tomography models from which we can calculate the ratio between V_S and V_P variations ($R = \mathrm{d}\ln V_s/\mathrm{d}\ln V_P$, here-after denoted as S/P ratio) and the correlation between V_S and V_C variations (here-after denoted as S-C correlation). We follow the methodology employed by Koelemeijer et al. (2018) with some adaptations as described below.

Rather than assuming a random distribution of temperatures in the mantle, we use the predicted present-day temperature distribution in the mantle based on a high-resolution isochemical mantle circulation model (Davies et al., 2012; see Koelemeijer et al., 2018 for more details). To convert these temperature variations to seismic velocities, we employ a thermodynamic database that describes the elastic parameters for any combination of pressure and temperature in the mantle for a given bulk mantle composition. However, existing databases based on thermodynamic mineralogical models (e.g. Stixrude & Lithgow-Bertelloni, 2011; Stixrude & Lithgow-Bertelloni, 2022) include ferropericlase only in the HS state. To obtain the required thermodynamic database for ferropericlase in different spin states, we first linearly interpolate our experimentally-verified computations for density and bulk modulus obtained at a few fixed temperatures (300, 1000, 2000, 3000 and 4000 K) to a spacing of 50 K, before linearly interpolating to every 1 GPa in pressure. We then calculate Voigt-Reuss-Hill average properties for a mantle of pyrolitic composition in a simplified six-component system using the thermodynamic database of Stixrude and Lithgow-Bertelloni (2011, personal communication 2019), but replacing the phase properties of ferropericlase with our results for the MS phase with *P-T* dependent spin fractions. Note that by calculating a phase weighted average, we implicitly assume that ferropericlase is homogeneously distributed in the mantle. The phase properties for HS ferropericlase in the published model of Stixrude and Lithgow-Bertelloni (2011) match with our new computational results for HS ferropericlase with relative differences of less than 0.5% along the geotherm. We convert the temperatures in the mantle circulation model to seismic velocities using the adapted

thermodynamic database, including either our own HS or MS ferropericlase results. The resulting high-resolution seismic mantle models describe realistic mantle structures, that we can use to calculate the relationships between seismic velocities, in order to investigate the expected effect of the spin crossover in ferropericlase in the Earth's mantle. Specifically, we calculate the S-C correlation, as well as S/P ratio.

The S-C correlation is calculated using equation (4) in Forte et al. (2015) and measures the linear correlation between V_S and V_C variations. The result varies between -1 and 1, with a value of -1 corresponding to perfect inverse correlation, a value of 0 corresponding to no correlation and a value of 1 corresponding to perfect linear correlation. For the calculation of both S-C correlation and S/P ratio, we directly use the spherical harmonic coefficients that describe the tomography models after reparameterization, using the same approach as in Koelemeijer et al. (2018). We focus on the radially averaged values of these quantities, in order to remove any geographic dependence due to the plate reconstruction model used in the geodynamic simulation.

We cannot directly compare the high-resolution synthetic models to data-derived tomography models from the literature, because these represent a filtered and weaker version of actual mantle structures. To enable a meaningful comparison, we multiply our high-resolution synthetic models with the resolution matrix of model SP12RTS (Koelemeijer et al., 2016). SP12RTS is one of few existing tomography models that inverted jointly for V_S and V_P variations in the mantle without imposing an *a priori* scaling, which is crucial for studying the relationships between different seismic velocities. It also provides the associated resolution matrix (or tomographic filtering), which allows us to capture the heterogeneous data coverage and inherent damping of the tomographic inversion. Therefore, we can perform like-to-like and quantitative comparisons between our synthetic tomography models with HS or MS ferropericlase and SP12RTS itself. By calculating the relationships between seismic velocities in both the high-resolution seismic models and the filtered models, we can determine the theoretically expected effect of the spin crossover in the Earth's mantle as well as what we may observe realistically at present in an existing tomography model.

2.3. Results and discussion

2.3.1. Comparison of experimental and computational results on the anomalous compressibility of ferropericlase at high temperature

The experimental unit-cell volumes of $(Mg_{0.8}Fe_{0.2})O$ collected in the ramp experiments at 300 K, 900 K and 1100 K are shown in figure 2.5a as a function of pressure, together with the isotherms from our ab-initio calculations. Previous data collected at 300 K (Lin et al., 2005) and at 1200 K in a laser-heated DAC (Mao et al., 2011) are also shown. We note that static compression data from Lin et al. (2005) and our dDAC measurements at 300 K with compression rates up to 1.3 GPa/s are in excellent agreement, suggesting that compression rates of this order of magnitude are sufficiently slow to avoid significant non-equilibrium effects in the system. Consequently, results from our high temperature ramp experiments with maximum compression rates ≤ 0.3 GPa/s are expected to be generally comparable to those derived during resistive-heating under static compression, but with largely increased pressure-resolution.

At approximately 60 GPa, there is a clear drop in the volumes determined from the compression ramps measured at 900 K, which is shifted to higher pressures by about 10 GPa compared to the volumes at 300 K. This change in the trend of the $V(P)$ curve is attributed to the onset of the spin crossover. Our experimental $V(P)$ data from both the ramp and pressure cycling experiments, as well as static compression while heating (figs. 2.5a & 2.6a) agree well with the new theoretical predictions at most pressures and temperatures. The only previously published data on ferropericlase at high temperature (Komabayashi et al., 2010; Mao et al., 2011) were collected in laser-heated DACs. Data from Mao et al. (2011) at 1200 K diverge from our experimental and computational results at pressures above ~40 GPa, where they are shifted to higher pressures and/or volumes (fig. 2.5a). This may be due to a higher iron content of the sample (25 at.%), the use of a different pressure standard, an inhomogeneous temperature distribution or chemical segregation that can occur during laser-heating (Sinmyo & Hirose, 2010).

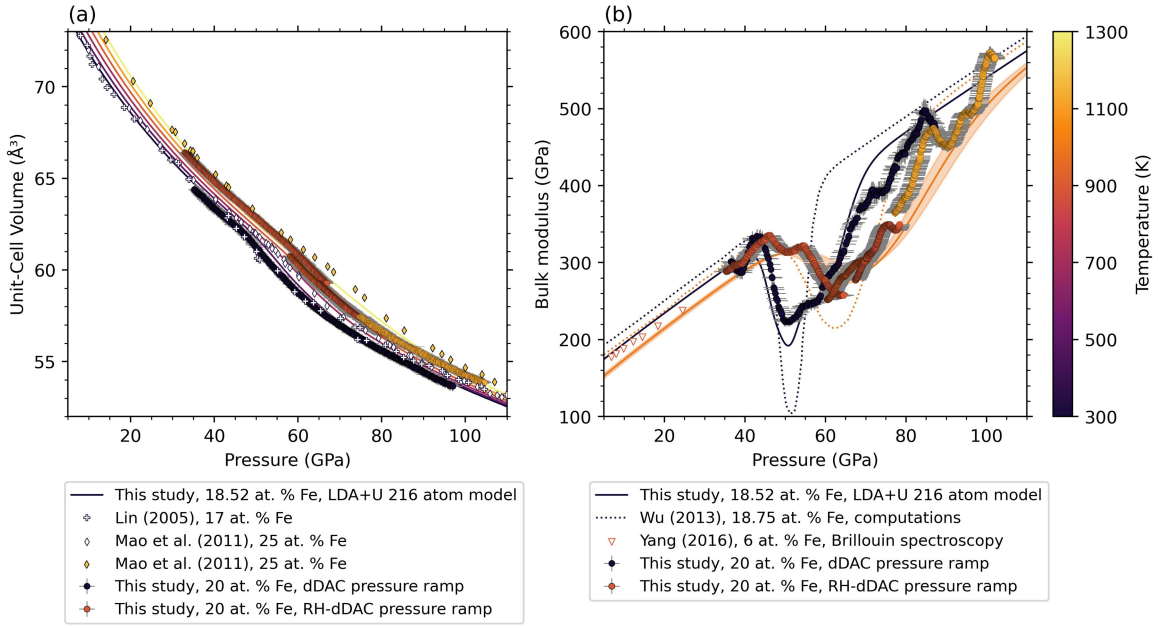

Figure 2.5 (a) Volume-pressure (*V*-*P*) data collected during quasi-continuous pressure ramp experiments at 300 K and 900-1100 K (filled circles), together with the predicted *V*-*P* curves along isotherms from our numerical calculations. Also shown are previous results from Lin et al. (2005) (static compression at room temperature, crosses) and from Mao et al. (2011) (static compression at room temperature and at 1200 K with laser heating, diamonds). (b) Experimental bulk moduli as a function of pressure at 300 K and high temperature, derived from pressure ramp experiments (filled circles). The error bars for pressure indicate the pressure interval over which the *V*-*P* curve was differentiated to derive the bulk modulus. The 1000 ± 100 K isotherm from our lattice dynamics calculations is shown as a solid orange line with a shaded region and the 300 K isotherm is indicated by a solid dark line. Also shown are Brillouin spectroscopy results at 900 K (open triangles, Yang et al. (2016)), as well as previous computational results at 300 K and 1000 K (dotted lines, Wu et al. (2013)). Note that the results from both Yang et al. (2016) and Wu et al. (2013) are for the adiabatic bulk modulus, whereas the results from this study are for the isothermal bulk modulus.

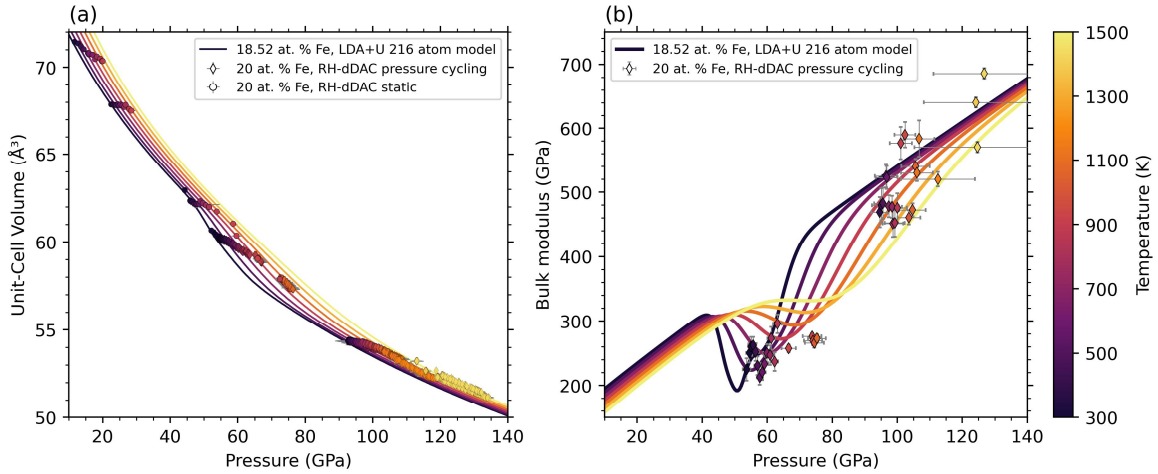

Figure 2.6 (a) Volumes derived from pressure cycling experiments (diamonds) and static compression while heating (circles), together with isotherms from lattice dynamics calculations (solid lines). (b) Bulk moduli derived from pressure cycling experiments at selected pressure-temperature conditions (diamonds), together with isotherms from the lattice dynamics calculations (solid lines). Error bars for pressure correspond to the pressure range of the cycling.

We note that there is generally significant disagreement on the onset pressure and width of the spin crossover in existing literature, using a wide range of experimental designs and analytical methods (see for example table 8 in Solomatova et al. (2016)). Some of these differences might arise from limited pressure resolution. The quasi-continuous nature of our compression curves allows us to constrain the spin crossover pressure range more precisely. We derived the isothermal bulk modulus directly from the slope of our $V(P)$ data, without having to fit an equation of state or rely on model assumptions (Méndez et al., 2021), providing the first experimental constraints on the bulk modulus softening of ferropericlase at high temperature.

In figure 2.5b, the experimentally determined bulk moduli are plotted as a function of pressure, together with our computational predictions and results from previous studies. The normalized L1 misfit (defined as the absolute difference normalized by the experimental value) between our experimental and computational results is shown in figure A.3. The misfit is $\lesssim 0.15$ at all pressures and temperatures, with average values of 0.07 and 0.06 for the ramps at 300 K and 900-1100 K, respectively. This demonstrates that there is good agreement between our experimental and computational results. The experimental data at room temperature show a softening in the bulk modulus between approximately 45 GPa and 80 GPa with an asymmetric shape. These features, which we attribute to the spin crossover, are reproduced by our *ab initio* calculations. Our experimental and theoretical results at 900-1100 K also agree well overall: both show a broad and asymmetric softening between approximately 50 GPa and 105 GPa. Pressure cycling measurements performed at selected *P-T* conditions confirm the softening of the bulk modulus at seismic frequencies (fig. 2.6b). There is good agreement between our results and Brillouin spectroscopy measurements at 900 K of the bulk modulus of $(Mg_{0.94}Fe_{0.06})O$ by Yang et al. (2016), although those measurements are limited to pressures below the spin crossover and made on a single-crystal sample of ferropericlase with lower iron content, in a neon PTM.

In our new computations a random distribution of iron atoms in the crystal lattice is accounted for and rather than assuming ideal mixing of HS and LS states, the enthalpy of mixed spin states is calculated, in addition to full HS and LS states (see Méndez et al., 2022 for details). This is in

contrast to older studies based on models assuming an ideal mixing of HS and LS iron and a uniform arrangement of iron atoms (Wentzcovitch et al., 2009; Wu et al., 2013). More recent studies have taken the favourable enthalpy of mixing of HS and LS states into account (Holmström & Stixrude, 2015; Sun et al., 2022), but these predict a wider spin crossover than found in this work. Comparison of our calculated bulk moduli with those of Wu et al. (2013) shows excellent agreement in regions where ferropericlase is in a pure high- or low-spin state, but differences emerge for the mixed-spin state. Similarly, differences in shear moduli are most pronounced in the mixed-spin region and increase at higher pressures and temperatures. This suggests that differences arise mainly from different values for the low-spin fraction of iron. Wu et al. (2013) predict a sharper bulk modulus softening over a narrower depth range and a larger amplitude than observed in our experimental results (fig. 2.5b), which is reflected in a much larger misfit compared to our computational results (fig. A.3). The average misfit between our experimental results and the computations from Wu et al. (2013) is 0.19 and 0.10 for the data at 300 K and 900-1100 K, respectively. Our new computational results thus fit the experimental data approximately twice as well as the previous theoretical models.

The agreement between our high-temperature experimental results and our computations at high temperature (fig. A.3) confirm the robustness of the later, allowing us to confidently extend the theoretical model to mantle temperatures. Our theoretical results for density (ρ) and seismic velocities (V_S, V_P and V_C) along several isotherms are shown in figure 2.7a–d for $(Mg_{0.8125}Fe_{0.1875})O$. Along a typical geotherm, the onset of the spin crossover is predicted to occur around 1,250 km depth, while full low-spin state is never reached (fig. 2.8), indicating that spin crossover-induced changes to the physical properties of ferropericlase are expected to affect most of the lower mantle (see also Méndez et al., 2022). We find a substantial reduction in V_P and V_C across the spin crossover, while V_S and ρ are barely affected and increase continuously with pressure (fig. 2.7a–d).

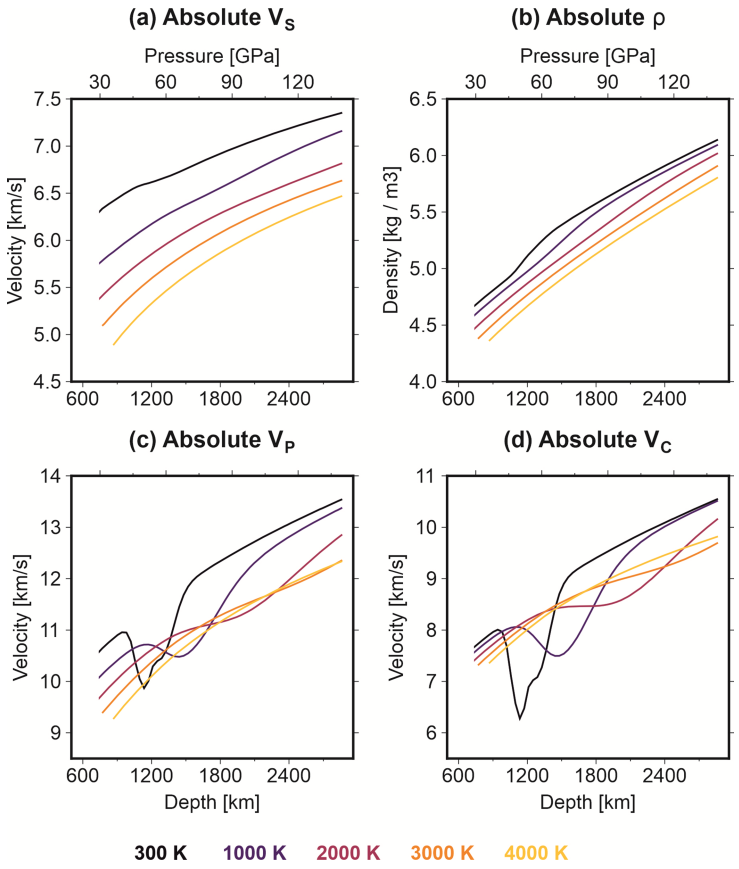

Figure 2.7 Theoretical predictions of absolute (a) S-wave velocity V_S, (b) density ρ, (c) P-wave velocity V_P, and (d) bulk sound velocity V_C of ferropericlase as a function of depth in Earth's mantle. The iron spin crossover leads to a marked reduction in V_P and V_C, while V_S and ρ increase continuously with depth with only slight changes in slope.

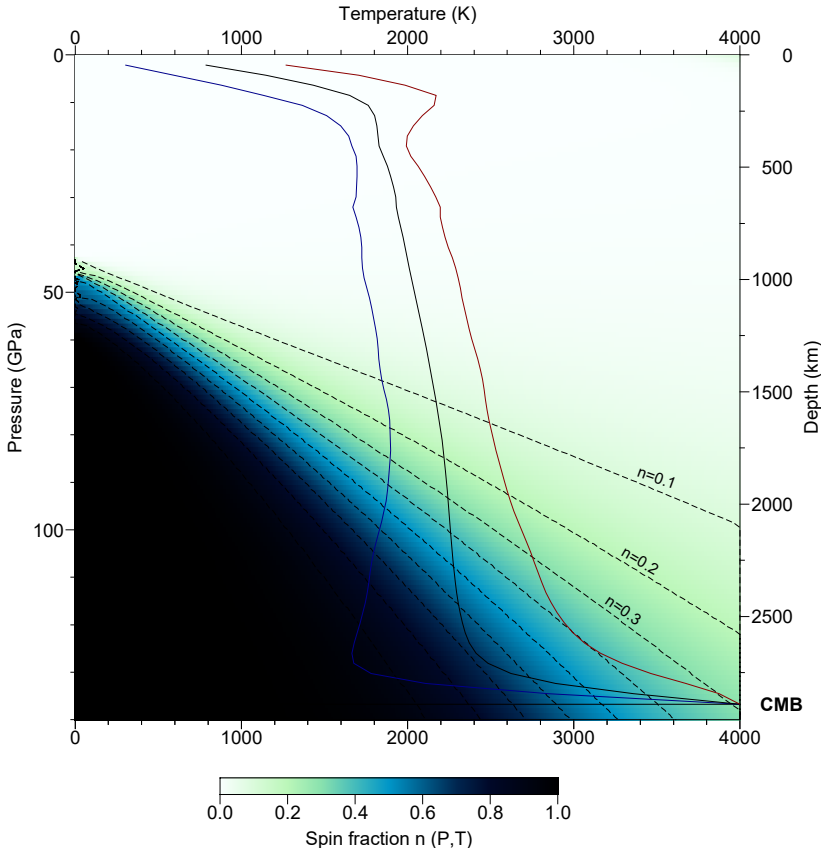

Figure 2.8 Low-spin fraction n as a function of pressure P and temperature T predicted by our theoretical calculations for the mixed-spin MS model, indicated by colour and contours. A radially averaged geotherm (black) and the range of temperature variations (95th percentile) in hot (red) and cold (blue) regions of the mantle (Davies et al., 2012) are also shown, indicating that full low-spin state is not reached in the lower mantle along a typical geotherm.

2.3.2. Signature of the spin crossover in seismic tomography

To understand how the signature of the spin crossover in ferropericlase will show up in data-based tomography models, we constructed synthetic seismic tomography models with and without the spin crossover, using the methodology described in section 2.2.3. Specifically, we combine the present-day temperature field of a high-resolution mantle circulation model (Davies et al., 2012; for details see Koelemeijer et al., 2018) with the temperature dependence of the spin crossover from our experimentally benchmarked calculations to create maps of the spin state and seismic velocity variations in the lower mantle (fig. 2.9).

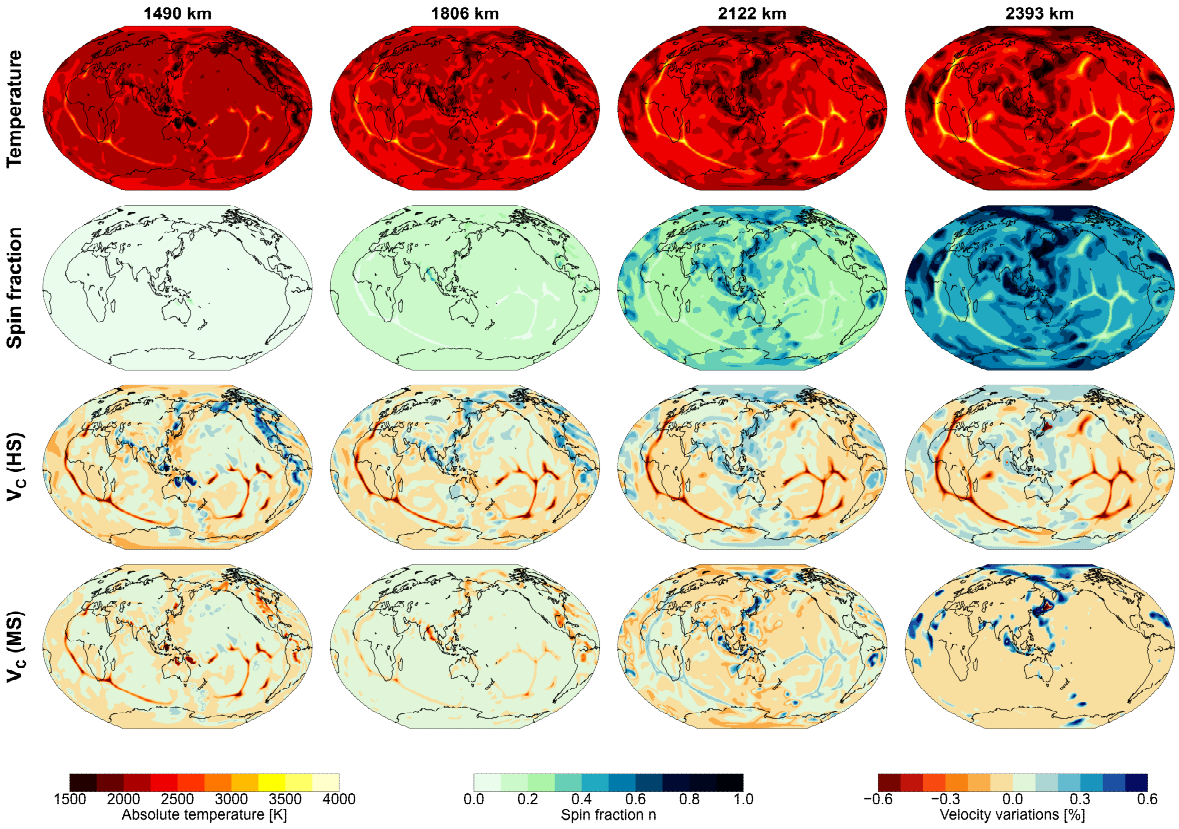

Figure 2.9 Maps of temperature, spin fraction and bulk sound velocity variations for high-spin and mixed-spin ferropericlase at different depths in the lower mantle in our synthetic models. The top row shows the temperature field generated from a high-resolution geodynamic model and the second row shows the fraction of ferropericlase in the low-spin state corresponding to these temperatures, as predicted by *ab initio* calculations. The last two rows show bulk sound velocity V_C variations in the high-resolution synthetic seismic tomography models when ferropericlase is assumed to stay in a high-spin state (HS model) and when the effects of spin fraction variations are included (MS model), respectively.

The distribution of heterogeneity in the mantle circulation model is, to first order, consistent with the seismologically imaged distribution, as it is largely dictated by 300 Myr of prescribed surface plate velocities. The resulting ring of downwellings around the Pacific and upwelling return flow in the Pacific and under Africa cause temperature variations in the lower mantle (fig. 2.9 top row). These temperature variations lead to substantial lateral variations in spin fractions at depths below 1,800 km (fig. 2.9 second row): low spin fractions are generally higher in cold regions with down-going slabs than in hot regions with upwelling plumes. In the bottom two rows of figure 2.9, bulk sound velocity variations are shown at different depths in the lower mantle for the HS (without the spin crossover) and MS (with the spin crossover) models. Our results clearly show that at depths where the elastic behaviour of ferropericlase is influenced by the spin crossover, bulk sound velocity variations are much less pronounced in the MS model compared to the HS model, indicating a lower sensitivity to temperature. In some regions, we even observe a positive correlation between temperature and bulk sound velocity, i.e., lower temperatures lead to negative velocity variations (e.g. 1490 km depth) and higher temperatures lead to positive velocity variations (e.g. 2122 km depth). This inversion of the temperature dependence can be explained by the shift of the bulk modulus softening in ferropericlase to higher pressures with increasing temperature, which leads to a positive temperature dependence of V_C (= $\sqrt{\frac{K}{\rho}}$) at specific P-T conditions (fig. 2.5b and 2.7d), as previously suggested (Marquardt et al., 2009a; Wu, 2016).

The seismic signature of the spin crossover becomes more evident when looking at the radially-averaged correlation between V_S and V_C variations in depth profiles of the synthetic tomographic models (fig. 2.10a). The anti-correlated temperature dependence of shear and bulk sound velocity in the spin crossover depth range leads to a strong negative anomaly in the S-C correlation in the MS model with a maximum around 1,800 km depth, which is absent in the HS model. A second minimum in the S-C correlation at lowermost mantle depths is the result of the bridgmanite to post-perovskite transition (Koelemeijer et al., 2018), which was included in the construction of the models.

To allow for a direct comparison between our high-resolution synthetic velocity models and data-derived seismic tomography models with a limited tomographic resolution, we apply a tomographic filter (see section 2.2.3). After filtering, the spin crossover signal in the depth profile of the mixed-spin synthetic tomography model becomes less pronounced, with a more smeared out and weakened negative S-C correlation (fig. 2.10b). Nonetheless, differences between the HS and MS models remain clearly visible. The MS model shows a lower S-C correlation between 1200 km and 2300 km depth than the HS model, indicating that a negative anomaly in S-C correlation can serve as a distinguishing feature in seismic observations for the detection of the iron spin crossover, even if a realistic limited seismic resolution is accounted for. A high V_S/V_P ratio has also been suggested in the past as a characteristic signature of the spin crossover (Marquardt et al., 2009a). While we observe a modest increase in S/P ratio at mid-lower mantle depths in the high-resolution MS model as a result of the spin crossover, the differences between the HS and MS models largely disappear after tomographic filtering (fig. 2.11). This suggests that S/P ratio is a less suitable measure for the detection of the spin crossover when accounting for the resolution achieved in current tomographic models.

When comparing our filtered synthetic tomography models to joint S- and P-wave model SP12RTS (Koelemeijer et al., 2016), we find that the negative S-C correlation at mid-lower mantle depths in SP12RTS is best reproduced by the synthetic model with ferropericlase in mixed-spin state (fig. 2.10b). Inclusion of the spin crossover significantly affects the L1 misfit with model SP12RTS between 1000 and 2500 km depth, reducing it on average by 63%, from 0.27 (HS) to 0.10 (MS) (fig. 2.10c). Since there is no other known process that has the same effect on seismic velocities at these depths, our results strongly suggest that the negative S-C correlation in the mid-lower mantle is caused by the iron spin crossover in ferropericlase.

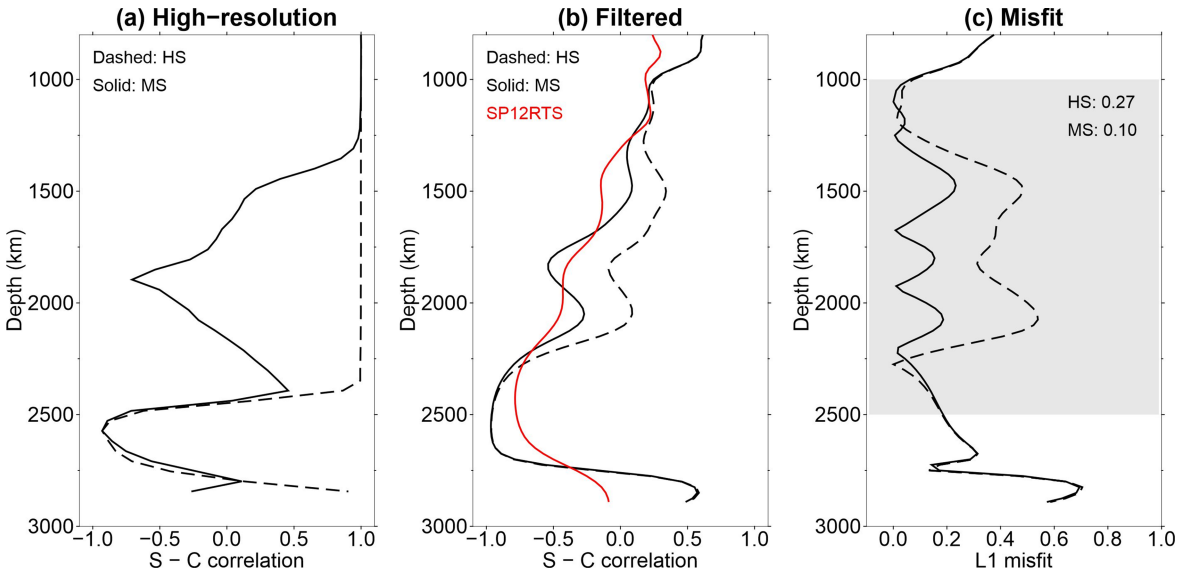

Figure 2.10 Prediction of radially averaged correlation between V_S and V_C variations (S-C correlation) along depth profiles in the synthetic tomography models without the spin crossover (high-spin ferropericlase only, HS) and including the spin crossover (ferropericlase with P-T dependent mixed spin fractions MS), as dashed and solid lines, respectively. (a) Results without the application of a tomographic filter, showing a strong negative anomaly in the mid-lower mantle produced by the spin crossover. (b) Results of the synthetic models with tomographic filtering compared to seismic tomography model SP12RTS (in red, Koelemeijer et al. (2016)). (c) L1 misfit between the predicted S - C correlations of the HS and MS models and model SP12RTS itself. The average misfit between 1000 and 2500 km depth (grey shaded region) is reduced by 63% from 0.27 (HS) to 0.1 (MS) when the effects of the iron spin crossover in ferropericlase are included.

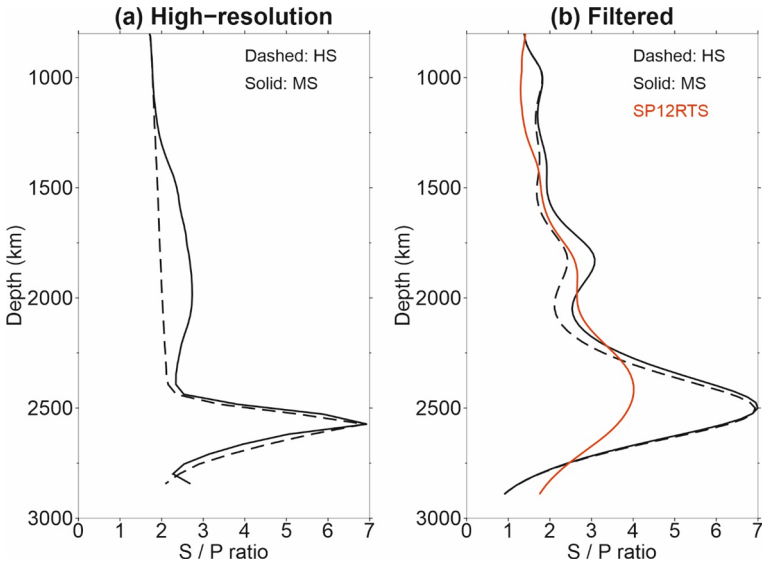

Figure 2.11 Radially averaged ratio between variations in V_S and V_P (S/P ratio) along depth profiles in the synthetic tomography models without the spin crossover (HS) and including the spin crossover (MS), as dashed and solid lines, respectively. (a) Results without the application of a tomographic filter, showing a moderate positive anomaly in the mid lower mantle produced by the spin crossover. (b) Results of the synthetic models with tomography filtering compared to seismic tomography model SP12RTS (in red, Koelemeijer et al. (2016)). The differences between the models are small after filtering and the MS model does not significantly improve the fit with SP12RTS.

Our work thus provides the first evidence for the visibility of the iron spin crossover in ferropericlase in seismic tomography models while taking realistic tomographic resolution into account. This finding implies the presence of about 20% of ferropericlase throughout the lower mantle, supporting recent works in favour of a pyrolitic lower mantle composition (Kurnosov et al., 2017; Wang et al., 2015; Zhang et al., 2016), as opposed to a perovskitic average composition (Murakami et al., 2012). If the depth resolution in seismic tomography models describing V_C variations improves in the future, a more detailed mapping of the spin crossover might become feasible and could ultimately allow for pinpointing average mantle temperature at mid-lower mantle depths, as well as lateral temperature variations from comparisons between synthetic and data-derived tomographic models. In areas of the mantle were subducting slabs cause cold downwellings, the spin crossover-induced changes in ferropericlase properties will occur at shallower depths as compared to the radial average, and the magnitude of the *Vc* softening will be larger (fig. 2.7d). This would make the seismic signature of the spin crossover easier to detect, consistent with the observations of Shephard et al. (2021). In contrast, in hot areas of the mantle (e.g. superplumes), the maximum V_C softening would be weaker and shifted to greater depths, near the core-mantle boundary (see also Méndez et al., 2022).

Our theoretical computations, that are used for the construction of the seismic tomography models are for a single composition of ferropericlase, i.e., an iron content of 18.75 at.%. Although this is close to the composition expected for the majority of the lower mantle (Irifune et al., 2010; Murakami, 2005), it has been suggested that the iron partitioning between ferropericlase and bridgmanite is affected by the spin crossover, leading to an increase of iron content of ferropericlase (Lin et al., 2013). In addition, ferropericlase may be enriched in iron in the lowermost mantle and the low seismic velocities in Ultra-Low Velocity Zones have been attributed to the presence of iron-rich ferropericlase (Wicks et al., 2010; Wicks et al., 2017). The spin crossover-induced bulk modulus softening is expected to shift to higher pressures with increasing iron content (Solomatova et al., 2016), so compositional variations in lower mantle-ferropericlase would affect the spin state, in addition to temperature variations. Such mechanisms should be

considered in future studies to further resolve the spin state of the lower mantle and its effect on mantle physical properties.

Other mantle minerals, most importantly bridgmanite, may also undergo a spin crossover at mantle pressures (e.g. Badro et al., 2004; Badro, 2014; Lin et al., 2005). However, despite ongoing research, any possible effects of a spin crossover in bridgmanite on elastic properties are not yet well-constrained (e.g. Fu et al., 2018; Okuda et al., 2020; Zhu et al., 2020) and likely weaker, and were therefore not included in the construction of our seismic velocity models. The methodology used in the present work may be adopted in future studies to resolve the effects of iron content of ferropericlase and a spin crossover in bridgmanite on global seismic tomography.

2.4. Conclusions

First experimental results on the spin crossover-induced elastic softening in ferropericlase at high temperature are reproduced by a new theoretical model that takes the position of iron atoms in the crystal lattice into account. By combining the experimentally-verified computations with the present-day temperature distribution in the mantle predicted by geodynamics, we constructed high-resolution synthetic seismic tomography models. The theoretically expected seismic signature of the spin crossover in the lower mantle is expressed as a strong negative anomaly in the S-C correlation and a moderate increase in S/P ratio. After applying a tomographic filter to account for a realistic tomographic resolution of data-driven tomography models, we find that a negative S-C correlation is the most suitable measure for detection of the spin crossover in seismic observations. Including the spin crossover in the filtered synthetic model improves the fit in the S-C correlation with global tomography model SP12RTS between 1000 and 2500 km depth by 63%. Our findings provide the first evidence for the visibility of the spin crossover in seismic tomography models when realistic tomographic resolution is accounted for and hence indicate the presence of mixed-spin ferropericlase in large parts of the lower mantle. Improvement of seismic resolution will facilitate a detailed mapping of the spin crossover using the S-C correlation. In the future, this may be translated to 3D maps of temperature and iron distribution in the mid-lower mantle, by reversing the protocol employed in this study.

Chapter 3. Seismic signal of the iron spin crossover in travel-time data

Preface

This chapter is currently in preparation for submission to *Geophysical Research Letters* as:

Trautner, V. E., Koelemeijer, P., Ritsema, J. & Marquardt, H. (*In prep*). Seismic Signal of the Iron Spin Crossover in Travel-Time Data.

In this chapter, the seismic signal of the spin crossover is investigated using synthetic travel-time data from seismic wave propagation simulations with AxiSEM3D. Synthetic results are compared to a global data set of travel-time anomalies. My contributions include preparing the input models and running the AxiSEM3D simulations, cross-correlation of the synthetic waveforms to obtain differential travel-times, analysis of the synthetic and observational data, data visualization and writing of the original draft. Synthetic velocity models were provided by Paula Koelemeijer and the global travel-time data set was provided by Jeroen Ritsema. Acknowledgements for this chapter include Adrian Mag, Benjamin Fernando and Andrew Walker for support with AxiSEM3D and Tarje Nissen-Meyer for helpful discussions.

Supplementary material is included in Appendix B.

Abstract

Seismology can provide essential constraints on the temperature and chemical composition of Earth's mantle, but this requires a detailed understanding of the effects of mineralogical processes on seismic observables. The iron spin crossover in ferropericlase, the second most abundant mineral in the lower mantle, causes significant changes to physical properties in the lower half of the mantle. Here, we characterize the seismic expression of the spin crossover in travel-time data using synthetic waveforms. We show that spin crossover-induced delays in P-wave arrivals lead to an increase in the ratio between travel-time anomalies of S- and P-waves ($\Delta S/\Delta P$). Our results suggest that the spin crossover can partially explain the increasing trend in $\Delta S/\Delta P$ with depth that is observed in a published set of global travel-time measurements. Finally, we demonstrate the temperature sensitivity of the seismic signal of the spin crossover and consider its potential to constrain lateral variations in mantle temperature.

3.1. Introduction

Constraining the thermochemical structure of Earth's mantle is essential to understand the present-day dynamics of our planet's interior and how it evolved over time. Seismic observations can provide crucial information on the thermochemical variability of the deep interior. However, their interpretation requires a detailed, quantitative understanding of the physical properties and mineralogical processes of mantle materials and how they affect seismic wave propagation. The lower mantle is primarily composed of bridgmanite, with (Mg,Fe)O ferropericlase constituting approximately 18% by volume as the second most abundant mineral (Irifune et al., 2010). At mid-lower mantle depths, ferropericlase undergoes an iron spin crossover, leading to changes in a wide range of properties that are relevant to large-scale geodynamic and geochemical processes (Lin et al., 2013). The spin crossover refers to a pressure-induced electronic reconfiguration of the *d* orbitals of ferrous iron in ferropericlase from a high-spin (HS) to a low-spin (LS) state, resulting in a reduction of the ionic radius of the iron atoms (Badro et al., 2003; Badro, 2014). The transition from full HS to full LS state occurs gradually over a broad pressure range, with the mixed-spin (MS) region extending over hundreds of kilometres depth at lower mantle temperatures (e.g. Sun et al., 2022; Trautner et al., 2023).

The spin crossover causes an increase in density and a softening of the bulk modulus in the MS region (e.g. Crowhurst et al., 2008; Lin et al., 2005; Marquardt et al., 2018; Méndez et al., 2022; Trautner et al., 2023; Wentzcovitch et al., 2009). This leads to a marked reduction in compressional (V_P) and bulk sound (V_C) velocities of ferropericlase, while shear modulus and shear velocities (V_S) are not substantially affected (e.g. Marquardt et al., 2009a; Wu et al., 2013; Yang et al., 2015). The difference in behaviour of V_S versus V_P and V_C in MS ferropericlase has been suggested to produce a characteristic seismic signature by which the spin crossover may be detected in seismic data (Marquardt et al., 2009a; Wu & Wentzcovitch, 2014; Yang et al., 2015). Indeed, several studies have recently reported evidence for the occurrence of the spin crossover in the lower mantle in seismic tomography models (Cobden et al., 2024; Shephard et al., 2021; Trautner et al., 2023) and one-dimensional (1D) models (Kennett, 2021) based on considerations of

these effects. In particular, comparisons with synthetic tomography models show that a negative correlation between V_S and V_C variations and a high ratio of V_S to V_P variations ($R = \mathrm{d}\ln V_s/\mathrm{d}\ln V_P$) in seismic tomography model SP12RTS in the mid-lower mantle is linked to the spin crossover (Trautner et al., 2023). A high R is often interpreted as evidence for thermochemical heterogeneity in the lower mantle (Deschamps & Trampert, 2003; Masters et al., 2000; Mosca et al., 2012), underlining the importance of taking the effects of the spin crossover on seismic observations into account.

The spin crossover is highly sensitive to temperature, with the onset shifting to greater depths and the MS region broadening with increasing temperature (e.g. Mao et al., 2011; Sturhahn et al., 2005; Sun et al., 2022; Trautner et al., 2023). In addition, the magnitude of the reduction in V_P and V_C is larger for lower temperatures, so the spin crossover should produce a more pronounced seismic signal in cooler regions of the mantle (Shephard et al., 2021; Trautner et al., 2023; Wu & Wentzcovitch, 2014). This raises the possibility to place constraints on vertical and lateral variations in mantle temperatures by using seismic observations to map the spin crossover in the lower mantle. However, identifying the signal of the spin crossover in seismic data requires a detailed understanding of the nature and magnitude of its effects on seismic observables. While previous studies have focussed on comparing predicted seismic velocity models incorporating the effects of the spin crossover with seismic tomography models (i.e., after inversion) (Cobden et al., 2024; Shephard et al., 2021; Trautner et al., 2023), the detectability of the spin crossover in raw travel-time data has not yet been studied.

Here, we investigate the effects of the spin crossover on the global seismic wavefield using synthetic seismograms. By recording differential travel-times for models with and without the spin crossover, we quantify the sensitivity of different seismic phases to its effects. We identify the signal of the spin crossover in the ratio between travel-time anomalies of S- and P-waves by comparing our synthetic data to a widely used global data set. Finally, we consider the effect of temperature on the seismic signal of the spin crossover and discuss its potential to constrain temperatures in the lower mantle.

3.2. Methodology

3.2.1. Synthetic forward modelling

In order to investigate the seismic signal of the spin crossover on travel-times, we run global seismic wave propagation simulations using AxiSEM3D (Leng et al., 2019). As input, we use spherically symmetric (1D) Earth models, derived from the synthetic seismic tomography models presented in Trautner et al. (2023) (Chapter 2). We consider four different isochemical models, either including or excluding the spin crossover and the bridgmanite to post-perovskite (Bg-ppv) transition: "*HS no ppv*", "*MS no ppv*", "*HS with ppv*", and "*MS with ppv*", where HS refers to models where ferropericlase does not undergo a spin crossover (i.e., remains in HS state) and MS refers to models including the properties of MS and LS ferropericlase.

These models are produced by combining the seismic properties of pyrolite using the thermodynamic database of Stixrude and Lithgow-Bertelloni (2011) and new, experimentally verified, computations of the properties of ferropericlase across the spin crossover (see section 2.2.3 for details). For each model, we extract three 1D velocity profiles along the average geotherm and for the 95th percentile temperatures (i.e., "*Average*", "*Hot*", and "*Cold*") of the present-day temperature distribution from a high-resolution mantle circulation model (Davies et al., 2012). We then combine the synthetic profiles for the lower mantle with the Preliminary Reference Earth Model (PREM, no ocean) (Dziewonski & Anderson, 1981) for the crust, upper mantle and core. To obtain a smooth depth profile we interpolate linearly between the values for PREM at 667 km depth and the values of the synthetic profiles over a 100 km depth interval. The twelve 1D velocity models obtained in this way (fig. 3.1) serve as input for the synthetic forward modelling.

We use AxiSEM3D (Leng et al., 2019), which degenerates to an axisymmetric spectral element method for spherically symmetric models, to simulate the global wavefield for each of the twelve synthetic models, as well as PREM. We use an earthquake source at 35 km depth with the moment tensor of the 2011 Mw 5.8 Virginia earthquake (CMT 201108231751A) for the simulations, which had a period of 10 s for computational efficiency. This is the minimum globally resolved period, i.e., higher period waves are also simulated. Shorter periods are not required, because spin

crossover-induced changes in seismic properties occur gradually over hundreds of kilometres depth and seismic waves are thus expected to be sensitive to these changes irrespective of the width of

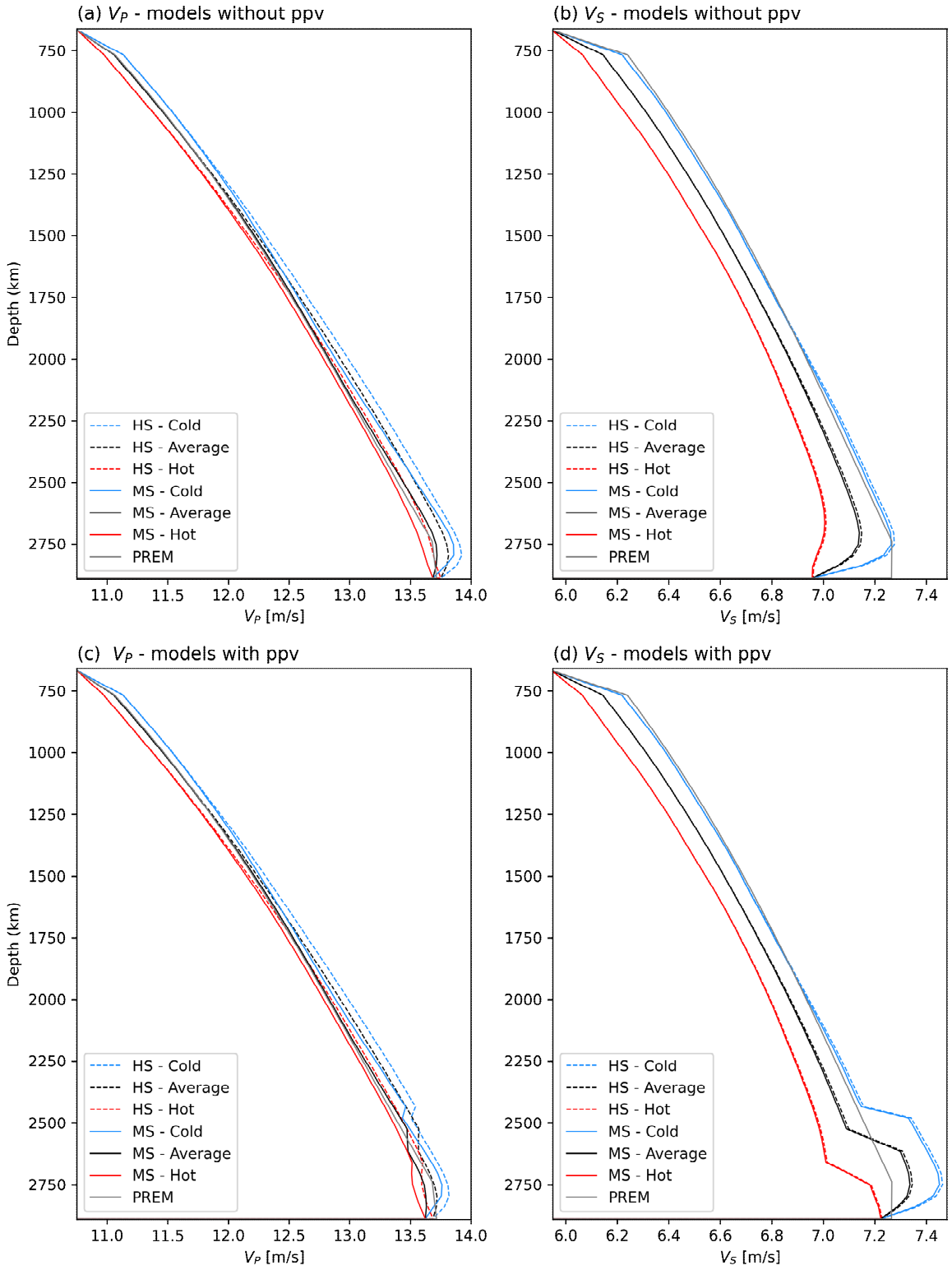

Figure 3.1 Compressional (V_P) and shear (V_S) wave velocity profiles along cold, average and hot geotherms for the four synthetic models used as input for wave propagation simulations, i.e., with or without the spin crossover (*MS* versus *HS*), and with or without the Bg-ppv transition (*with ppv* versus *no ppv*). PREM velocity profiles are shown for reference.

their Fréchet kernels (Hung et al., 2000). Synthetic seismograms were recorded from 25 s before to 3600 s after the origin time at epicentral distances between 0-180°.

3.2.2. Differential travel-time measurements

While any seismic phases passing through the mid-lower mantle may show differences as a result of the spin crossover, we expect phases with turning points in the spin crossover depth range (i.e., below approximately 1,250 km depth (Méndez et al., 2022; Trautner et al., 2023) to be most sensitive to its effects. In addition, the spin crossover signal may be obscured in phases that strongly interact with the core-mantle boundary (CMB). Therefore, we focus our attention on direct P- and S-waves and their surface reflections that turn in the lower mantle (fig. 3.2). We use ObsPy (Beyreuther et al., 2010) to obtain differential travel-time measurements (δT), by cross-correlating the synthetic waveforms in windows around the ray-theoretical arrival times of the phase of interest, as illustrated in figure 3.3. Differential travel-times of any P+P_{diff}, PP, PPP, S+S_{diff}, SS and SSS waves arrivals between 5° and 180° epicentral distance are determined at 5° intervals, with a minimum correlation coefficient $r > 0.8$. The vertical component trace was used for P-wave arrivals and the transverse component for S-wave arrivals. To investigate the magnitude of the spin crossover effects in seismic observations, we determine the differential travel-time between models with and without the spin crossover (i.e., $\delta T_{HS\text{-}MS}$) for each temperature profile (fig. 3.4).

The ratio of V_S to V_P variations R is sensitive to the spin crossover (Marquardt et al., 2009a; Trautner et al., 2023; Wu & Wentzcovitch, 2014; Yang et al., 2015). There are many ways to obtain this, but it is commonly estimated directly from seismic data using the slope of the best-fitting line relating the travel-time residuals of S- and P-wave phases (Chaves et al., 2021; Masters et al., 2000; Ritsema & van Heijst, 2002). Therefore, we can use this measure, which we shall refer to as the ΔS/ΔP slope, to compare our synthetic results to observational data. We take a subset of the travel-time residuals used by Koelemeijer et al. (2016) in the construction of seismic tomography model SP12RTS, which were obtained by cross-correlation with normal mode synthetics for PREM after low-pass filtering to a period of > 16 s. We select data for P and S

waves, as well as *PP* and *SS* waves, recorded for common earthquake-receiver pairs, with ray-theoretical turning depths below the transition zone. We divide the data into overlapping bins of 10°-wide epicentral distance intervals, offset by 50%. For each bin, we determine the slope of the best-fitting line relating S-wave and P-wave travel-times using the first principal component in a principal component analysis (PCA) (see figs. B.1 and B.2). A bootstrapping routine is employed to estimate the uncertainty in the obtained values for δT_S / δT_P and δT_{SS} / δT_{PP}.

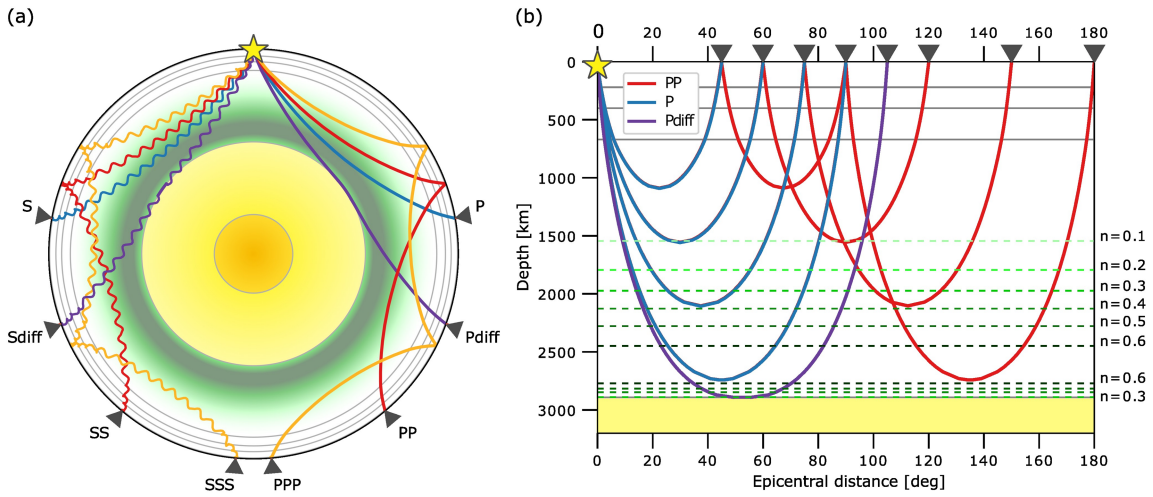

Figure 3.2 Ray paths of selected seismic phases predicted for PREM. (a) Example ray paths of the phases considered in this study, with turning points between the base of the transition zone and the core-mantle boundary, plotted in spherical geometry. (b) Ray paths of P-wave phases in cartesian geometry, illustrating ray-theoretical turning depths for arrivals at selected epicentral distances. Dashed lines indicate contours of low spin fraction *n* along an average geotherm, based on Trautner et al. (2023). The yellow star indicates the earthquake source and grey triangles indicate receivers.

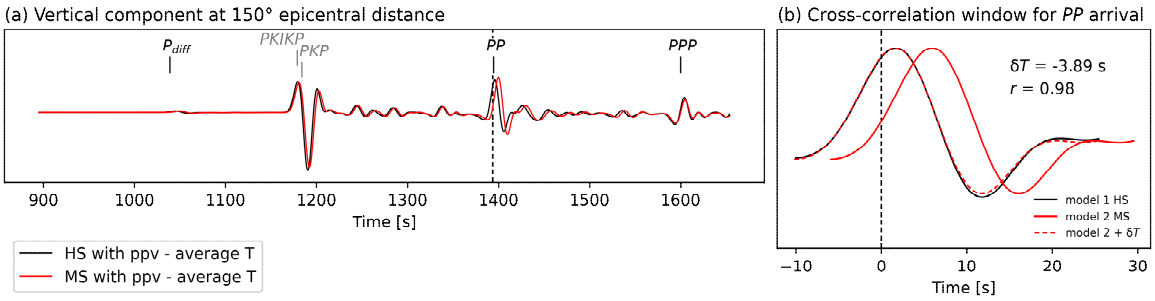

Figure 3.3 Example of a differential travel-time measurement. (a) Vertical component trace of the synthetic waveforms recorded at 150° epicentral distance for models with (MS) or without (HS) the spin crossover (red and black lines, respectively). (b) Cross-correlation between waveforms from HS and MS models in windows around the *PP* arrival times predicted by ray theory (shown as a dashed black line for the HS model in both panels). The dashed red line shows the MS waveform after a time shift of -3.89 s is applied, resulting in the best fit with a correlation coefficient $r = 0.98$.

We likewise determine travel-time anomalies for our synthetic models with respect to PREM (i.e., $\delta T_{PREM\text{-}syn}$) using cross-correlation of the waveforms obtained from the AxiSEM3D simulations. For each of the four models (HS/MS, with/without ppv), we combine the travel-time residuals of the three different temperature profiles, group them into epicentral distance bins, and determine the ΔS/ΔP slopes by PCA. With this approach, illustrated in figure 3.5a for a single distance bin, we effectively assume that lateral temperature variations in the mantle are the dominant factor in the correlation between global S- and P-wave travel-time residuals.

3.3. Results and discussion

3.3.1. Spin crossover effects on seismic travel-time anomalies

The differential arrival times of HS models with respect to MS models are shown in figure 3.4. We find increasingly negative $\delta T_{HS\text{-}MS}$ at epicentral distances corresponding to ray-theoretical turning depths in the spin crossover range. The delay is much greater for P-waves than S-waves, as we would expect from the contrasting effects of the spin crossover on V_P versus V_S (e.g. Marquardt et al., 2009a; Wu et al., 2013; Yang et al., 2015). When looking at the results for the different temperature profiles, the temperature-dependence of the spin crossover is evident: the spin crossover-induced travel-time delays shift to higher epicentral distances (corresponding to greater turning depths) for hotter geotherms. We find that for the average geotherm, direct P-waves are up to ~3.5 s slower as a result of the spin crossover, while PP-waves are delayed by up to ~6 s. These values are of the same order of magnitude as P-wave travel-time anomalies associated with Large Low Velocity Provinces (LLVPs) (e.g. Chaves et al., 2021; Koelemeijer et al., 2016). This underscores the importance of considering spin crossover effects on seismic observations when inverting for the thermochemical structure of the lower mantle (Cobden et al., 2024). Including changes in properties associated with the spin crossover in thermodynamic databases used for such inversions is a key next step, which has only started to be implemented very recently (Deng et al., 2023; Stixrude & Lithgow-Bertelloni, 2024).

To compare the magnitude of the effects on travel times from the spin crossover to other mineralogic transitions in the lower mantle, the differential arrival times of models with ppv with

respect to models without ppv are shown in figure 3.5. We see that ppv starts to affect travel times at greater epicentral distances compared to the spin crossover. This is expected, since the Bg-ppv transition occurs in the lowermost mantle, while the onset of the spin crossover is in the mid-lower mantle. We find that the contribution of ppv to delays in S-wave travel times is significantly larger than that of the spin crossover. In contrast, the magnitude of the travel-time delays for P-waves introduced by the Bg-ppv transition is comparable to the spin crossover-induced delays, but of opposite sign (i.e. P-waves travel faster as a result of ppv, but are slowed down by the spin crossover).

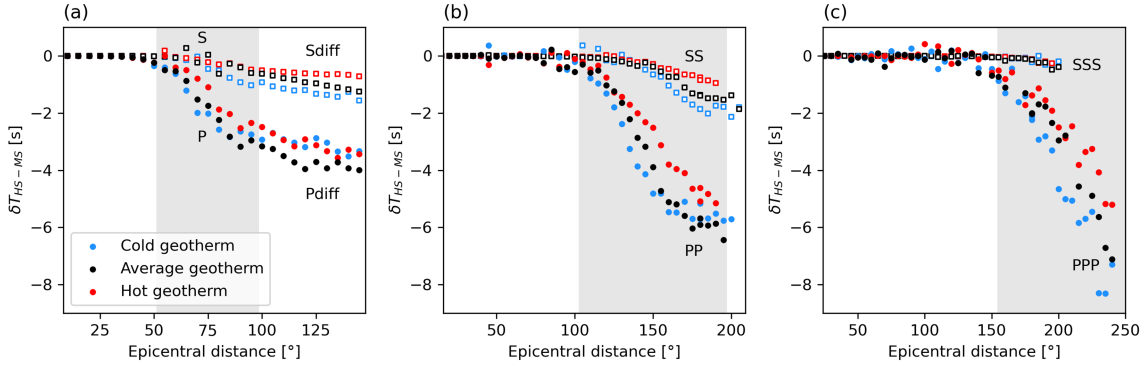

Figure 3.4 Effect of the spin crossover on differential travel-times between models with (MS) and without (HS) the spin crossover (and with post-perovskite). Results for P+P_{diff} and S+S_{diff} waves in (a), for *PP* and *SS* waves in (b), and for *PPP* and *SSS* waves in (c). P- and S-wave phases are shown as solid circles and open squares, respectively. Colours indicate cold, average and hot geotherm models (blue, black and red symbols, respectively). The shaded areas correspond to PREM ray-theoretical turning depths between 1,250 and 2,890 km (the approximate depth range of the spin crossover).

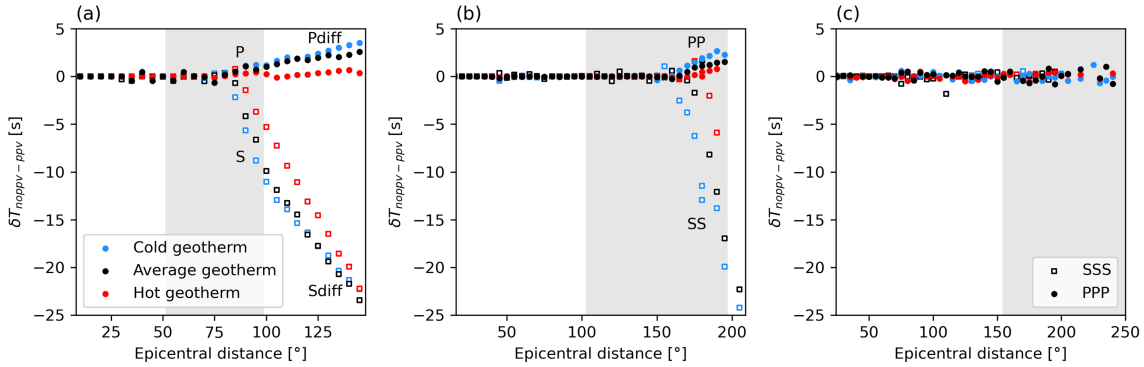

Figure 3.5 Effect of the bridgmanite to post-perovskite transition on differential travel-times between HS models with (ppv) and without (noppv) post-perovskite. Results for P+P_{diff} and S+S_{diff} waves in (a), for *PP* and *SS* waves in (b), and for *PPP* and *SSS* waves in (c). P- and S-wave phases are shown as solid circles and open squares, respectively. Colours indicate cold, average and hot geotherm models (blue, black and red symbols, respectively). The shaded areas correspond to PREM ray-theoretical turning depths between 1,250 and 2,890 km.

3.3.2. ΔS/ΔP slopes from synthetics in comparison to a global data set

To further investigate the seismic signal of the spin crossover, we determine δT_S / δT_P and δT_{SS} / δT_{PP} as a function of epicentral distance for both synthetic travel-time data and the global observational data set (figs. 3.6b and 3.6c). The ΔS/ΔP slopes based on observations show an increase with epicentral distance, consistent with findings from previous studies, that suggest an increase of R with depth in the mantle (Chaves et al., 2021; Masters et al., 2000; Ritsema & van Heijst, 2002). The large uncertainties for δT_{SS} / δT_{PP} around 150° are caused by a low number of travel-time measurements in this distance range (see fig. B.2), due to interference with other arriving phases. Nonetheless, an increase in the ΔS/ΔP slopes of about 50% over an epicentral distance range where waves turn in the bottom half of the mantle (i.e., ~60-90° for δT_S / δT_P and 110-175° for δT_{SS} / $\delta T_{PP)}$ appears to be a robust feature in the observational data.

We find that none of the synthetic models reproduces the observational ΔS/ΔP slopes exactly, but we can nevertheless use our results to investigate and quantify the effects of the spin crossover and post-perovskite. The spin crossover causes an increase in ΔS/ΔP slopes at epicentral distances where waves turn in the mid-lower mantle, with slopes for MS models about 0.5 higher than for HS models (fig. 3.6). Inclusion of the Bg-ppv transition in the models produces an even larger increase (up to 1.2 with respect to models without ppv), but only at epicentral distances sensitive to regions near or at the CMB (i.e., >75° for δT_S / δT_P and >155° for δT_{SS} / δT_{PP}). To test how well the synthetic models agree with the observational data, we have calculated the average L2 misfit, defined as the squared difference, over the epicentral distance range affected by the spin crossover (Table 3.1). For δT_S / δT_P, the misfit is improved from 2.6 to 1.1 (i.e., by 58%) if the effects of both the spin crossover and the Bg-ppv transition are included. For δT_{SS} / δT_{PP} the misfit is similar for all models (i.e., 0.3) and we can thus not say that one model is favoured over the others.

Nonetheless, we find that the increasing trend in the ΔS/ΔP slopes that we see in the observational data is strongest in the model that includes both the spin crossover and the Bg-ppv transition (fig. 3.6). This suggests that both mineralogical processes contribute materially to the seismic properties of the lower mantle and are at least partially responsible for an increase in R with depth. The lack

of an exact match between the synthetic and observational results may be explained by the simplifications and assumptions inherent to the synthetic models, i.e., they are isochemical and spherically symmetric. Thus, the models cannot capture any complexities in the observational data resulting from chemical heterogeneities or lateral variations in seismic properties. In addition, the observational source-receiver paths are not uniformly distributed over the globe, which may affect the derived ΔS/ΔP slopes (although there is no significant depth-dependent bias in the distribution).

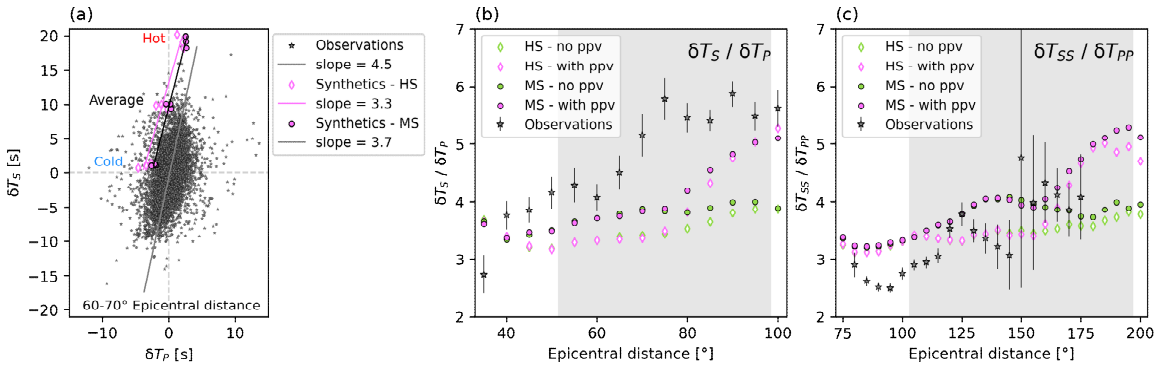

Figure 3.6 Effect of the spin crossover on the ΔS/ΔP slope. (a) Measurements of δT_S versus δT_P with respect to PREM for common source-receiver pairs at epicentral distances between 60-70°, with best-fitting lines. Observational data are shown as grey stars and synthetic data for HS and MS models with post-perovskite are shown as open diamonds and solid circles, respectively. Labels indicate the datapoints from the hot, average and cold temperature profiles. ΔS/ΔP slopes derived from the best-fitting lines as a function of epicentral distance are shown in (b) for δT_S / δT_P and in (c) for δT_{SS} / δT_{PP}. Values for the synthetic models with/without the spin crossover are indicated by open diamonds and solid circles, respectively. Pink and green indicate models with/ without post-perovskite, respectively. Slopes derived from the observational data are shown as grey stars, with error bars showing two standard deviations. The shaded areas correspond to ray-theoretical turning depths between 1,250 and 2,890 km for PREM.

Table 3.1 Average L2 misfit between models and observational data in the region affected by the spin crossover

	HS no ppv	MS no ppv	HS with ppv	MS with ppv
δT_S / δT_P[a]	2.6	1.8	1.8	1.1
δT_{SS} / δT_{PP}[b]	0.3	0.3	0.3	0.3

[a]Between 50-95° epicentral distance
[b]Between 105-175° epicentral distance

3.4. Towards constraining mantle temperature using the spin crossover signal

The spin crossover-induced travel-time delays for the three temperature profiles (fig. 3.4) reflect both the temperature sensitivity of the spin crossover, as well its differing effects on V_S and V_P. These characteristics of the spin crossover may allow its seismic signature to be used to map the spin state of the lower mantle and, consequently, constrain mantle temperatures. However, since a HS-only reference does not exist in the mantle, this would require identifying the signal of the spin crossover in seismic observations with respect to a global average, such as PREM (Dziewonski & Anderson, 1981). To investigate the temperature sensitivity of the spin crossover signal, we can thus look at the differences in travel-times between the hot and cold models relative to the average geotherm model, which is analogous to PREM in our synthetics (fig. 3.7c and 3.7d).

We find that δT_{SS} increases/decreases continuously with depth in a symmetric fashion in the mid-lower mantle for the hot and cold models, respectively, with irregularities that are attributed to the Bg-ppv transition occurring only in the lowermost mantle. Contrastingly, in models with the spin crossover the magnitude of δT_{PP} does not increase continuously with depth, but stays constant over a certain depth range. The same is observed for δT_P & δT_S and δT_{PPP} & δT_{SSS} (figs. B.3 and B.4).

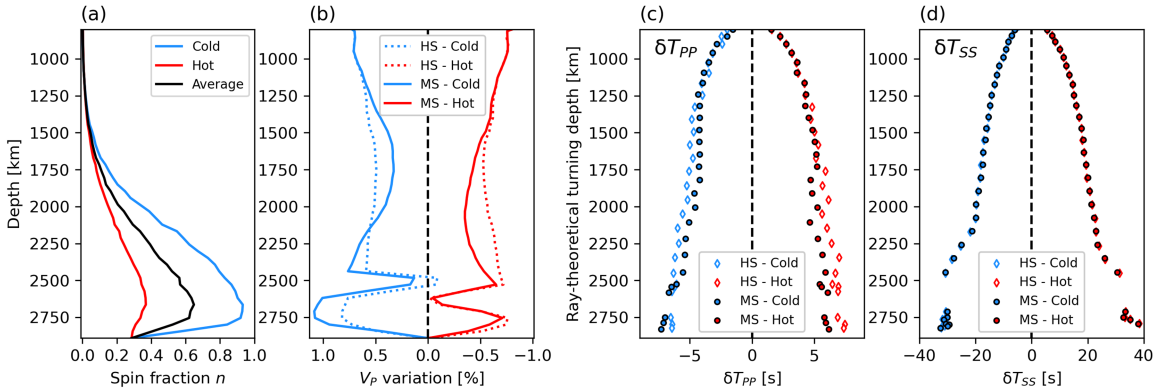

Figure 3.7 Effect of temperature on the signal of the spin crossover in seismic travel-times. (a) Low spin fraction n as a function of depth for the cold, hot and average temperature profiles (from Trautner et al., 2023). (b) Variations in V_P for cold (blue) and hot (red) velocity profiles with respect to the average geotherm, for MS (solid line) and HS (dotted line) models with post-perovskite. (c,d) *PP* and *SS* travel-time anomalies for the cold (blue) and hot (red) models with respect to the average geotherm model, as a function of ray-theoretical turning depth. Results are shown for MS models (filled circles) and HS models (open diamonds) with post-perovskite.

This “flattening” of the curves is temperature dependent: for the cold model it occurs from about ~1,250 km depth, while we observe it below ~1,750 km depth in the hot model.

These observations can be explained by the reduced temperature sensitivity of V_P in the depth range of the spin crossover, as a result of its temperature-dependence (Trautner et al., 2023). The onset of the spin crossover shifts to greater depths and the fraction of LS iron increases less steeply with increasing temperature (fig. 3.7a). The spin crossover-induced reduction in V_P is most pronounced for spin fractions <0.4 (Méndez et al., 2022), resulting in a temperature-dependent minimum in V_P variations with respect to the average geotherm (fig. 3.7b). The resulting asymmetry in δT_{PP} compared to δT_{SS} for the hot and cold models indicates that the spin crossover causes an increase in ΔS/ΔP that will occur at greater epicentral distances (i.e., corresponding to greater depths) for hotter regions of the mantle. This characteristic may in principle provide a tool to constrain spin state and temperature variations in the mid-lower mantle. However, it may not be easily distinguished in current observational travel-time data, especially if it were obscured by effects from chemical heterogeneities at these depths.

3.5. Conclusions

Using seismic waveform modelling, we characterize and quantify the signal of the spin crossover in ferropericlase in seismic travel-time data. We show that the spin crossover causes P-wave travel-time delays that are of the same order of magnitude as those observed due to LLVPs, emphasizing that it is crucial to account for the effects of the spin crossover in seismic inversions for meaningful interpretations of mantle temperatures and composition. The spin crossover causes a characteristic increase in the ratio between travel-time anomalies of S- and P-waves with epicentral distance, that is in qualitative agreement with the ΔS/ΔP slopes in a data set of global travel-time measurements. The seismic expression of the spin crossover varies with temperature, shifting to higher epicentral distances (i.e., greater depths) for hotter mantle geotherms. While the seismic characteristics of the spin crossover identified here could in principle be used to constrain temperature variations in the lower mantle, the signal remains subtle. Future studies will reveal whether it is strong enough to be detected in seismic observations of Earth’s mantle.

Chapter 4. Iron content-dependence of ferropericlase elastic properties across the spin crossover from novel experiments and machine learning

Preface

The contents of this chapter have been published in:

Trautner, V. E., Rijal, A., Plueckthun, C., Satta, N., Koemets, E., Buchen, J., Wang, B., Glazyrin, K., Cobden, L. & Marquardt, H. (2024). Iron Content-Dependence of Ferropericlase Elastic Properties Across the Spin Crossover From Novel Experiments and Machine Learning. *Geophysical Research Letters*, *51*(22), https://doi.org/10.1029/2024gl111276

This chapter presents new experimental results on two ferropericlase compositions, as well as predictions of the relationship between ferropericlase physical properties, pressure and iron content inferred from experimental data using machine learning methods. My contributions include microprobe analysis of the samples, preparing and conducting high-pressure experiments, data processing and analysis, collating literature data, training Mixture Density Networks (MDNs) and processing the results, data visualization and writing of the original draft. Synthesis of the ferropericlase samples and Mössbauer spectroscopy was carried out by Christian Plueckthun. The MDN code was provided by Ashim Rijal.

Supplementary material for this chapter is included in Appendix C. Data tables are available via the online version of the publication. Funding bodies and acknowledgements may also be found with the article.

Abstract

The iron spin crossover in $(Mg_{1-x}Fe_x)O$ ferropericlase causes changes to its physical properties that are expected to affect seismic velocities in Earth's lower mantle. We present new time-resolved pressure-volume measurements of iron-rich ferropericlase (x_{Fe} = 0.40, 0.59) and combine the results with literature data with x_{Fe} = 0.04–0.6 to investigate the dependence of ferropericlase elastic properties on iron content. We infer the relationship between unit-cell volume, pressure and iron content directly from the data by training Mixture Density Networks and derive bulk modulus, density and bulk sound velocity from the outputs. This allows us to constrain the effect of the spin crossover on these properties and estimate their uncertainties for different iron contents. Our findings indicate that the spin crossover may significantly alter the physical properties of ferropericlase in iron-enriched regions in the lowermost mantle, with implications for the interpretation of seismic heterogeneities observed near the core-mantle boundary.

4.1. Introduction

Earth's lower mantle comprises over half of the planet's volume and is thought to predominantly consist of the two minerals bridgmanite and ferropericlase. For a pyrolitic bulk composition, $(Mg_{1-x}Fe_x)O$ ferropericlase constitutes approximately 18% by volume (Irifune et al., 2010) and is therefore expected to play a major role in the physical properties and geodynamic processes governing Earth's deep interior. Iron in ferropericlase undergoes a pressure-induced electronic spin transition from a high-spin (HS) to a low-spin (LS) state (Badro et al., 2003). The transition occurs gradually, with HS and LS iron atoms coexisting over a broad pressure/depth range that is referred to as the spin crossover region. Along a typical lower mantle geotherm, this region is expected to extend from approximately 1,250 km depth to the Core-Mantle Boundary (CMB) (Trautner et al., 2023). The spin crossover leads to a softening of the bulk modulus of ferropericlase (e.g. Marquardt et al., 2009a; Méndez et al., 2022), with wide-ranging geophysical implications (e.g. Cammarano et al., 2010; Lin et al., 2013; Marquardt & Miyagi, 2015).

Ferropericlase with approximately 20 at.% Fe (i.e., $x_{Fe} = 0.2$) is considered representative for most of the lower mantle (Irifune et al., 2010; Murakami, 2005; Sinmyo & Hirose, 2013) and has therefore been extensively studied (e.g. Lin et al., 2007a; Mao et al., 2011; Méndez et al., 2022; Trautner et al., 2023; Wu et al., 2013). However, iron partitioning between ferropericlase and bridgmanite is expected to change with pressure, temperature and spin state, possibly increasing ferropericlase iron content up to 35 at.% at the base of the lower mantle (Muir & Brodholt, 2016). Evidence for a wide range of ferropericlase compositions has been found in super-deep diamond inclusions (Kiseeva et al., 2022) and the notion of a chemically heterogeneous lower mantle is becoming increasingly accepted. The anomalous seismic properties of Large Low Velocity Provinces (LLVPs) and Ultra-Low Velocity Zones (ULVZs) are widely believed to have a thermo-chemical origin (Garnero et al., 2016). LLVPs are best explained by warm material enriched in iron and silicate (Deschamps et al., 2015), while ULVZs have been suggested to consist of chemically distinct, strongly iron-enriched material (e.g. Liu et al., 2016; Otsuka & Karato, 2012). Iron-enriched ferropericlase may play a major role in these observed heterogeneities, since iron

partitions strongly into ferropericlase for high total iron contents (Muir & Brodholt, 2016) and the physical properties of iron-rich ferropericlase may account for the seismic characteristics of ULVZs (Finkelstein et al., 2018; Wicks et al., 2017; Yu & Garnero, 2018).

In light of the wide range of expected compositions of ferropericlase in Earth's lower mantle, a detailed understanding of the physical properties of ferropericlase as a function of iron content is essential. Changes as a result of the spin crossover are of particular interest. The spin crossover is known to shift to higher pressures with increasing iron content (e.g. Cheng et al., 2018; Glazyrin et al., 2017; Muir & Brodholt, 2015; Solomatova et al., 2016; Speziale et al., 2005), but the iron content-dependence of the elastic softening of ferropericlase is not well-constrained. While experimental high-pressure studies have been conducted for a range of ferropericlase compositions, data coverage is sparser for pressures relevant to the lowermost mantle (fig. 4.1a). Moreover, existing results are often inconsistent even at low pressures, likely due to inevitable experimental uncertainties and differences in experimental approaches and pressure scales used (Solomatova et al., 2016). In addition, the conventional approach to determine elastic properties of minerals by fitting data to an Equation of State (EoS) introduces potential biases in uncertainty quantification (Rijal et al., 2021) and is particularly problematic for ferropericlase due to its anomalous compression behaviour across the spin crossover.

Here, we present new results on the compression behaviour of $(Mg_{1-x}Fe_x)O$ with $x_{Fe} = 0.40$ and $x_{Fe} = 0.59$ across the spin crossover, employing time-resolved X-ray diffraction (XRD) in combination with continuous compression experiments in Diamond Anvil Cells (DACs). We combine our results with published pressure-volume data on ferropericlase with $x_{Fe} = 0.04$–0.6 and use Mixture Density Networks (Rijal et al., 2021) to infer the relationship between pressure, unit-cell volume and iron content (P-V-X_{Fe}) of ferropericlase from the compiled data set. By applying machine learning techniques, we can comprehensively integrate existing experimental data and quantify uncertainties. Furthermore, this approach allows us to derive the isothermal bulk modulus as a function of pressure and iron content, without imposing any *a priori* assumptions on the thermodynamic model or functional form of the EoS.

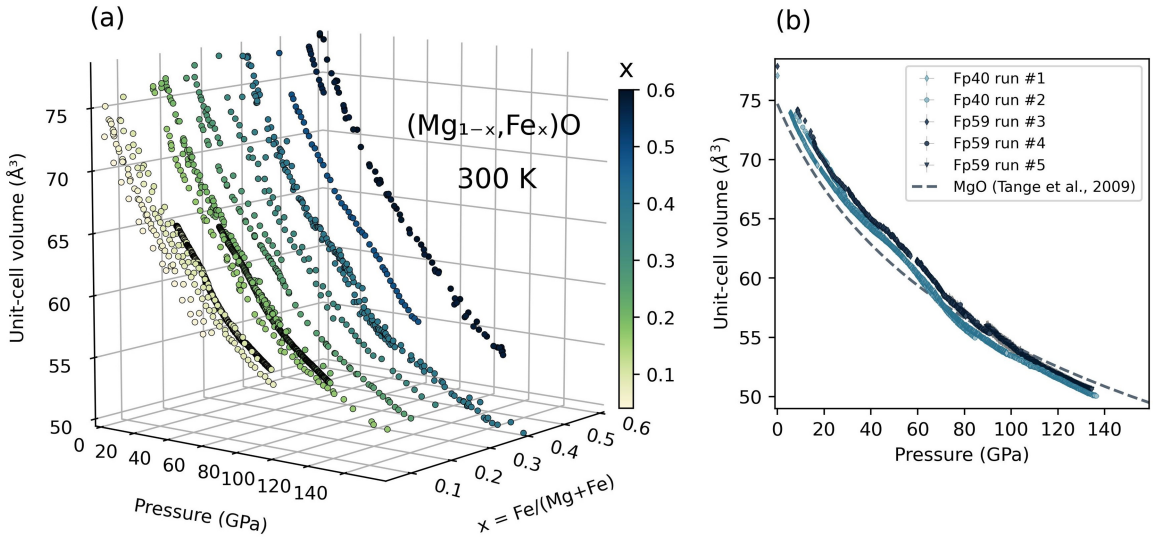

Figure 4.1 Experimental P-V-X_{Fe} data on $(Mg_{1-x}Fe_x)O$. (a) Overview of previously published P-V data from XRD measurements on ferropericlase with x_{Fe} = 0.04-0.6 (see section 4.3.2 for references). Reported uncertainties are not shown for clarity. (b) Unit-cell volumes of $(Mg_{0.60}Fe_{0.40})O$ (Fp40, light symbols) and $(Mg_{0.41}Fe_{0.59})O$ (Fp59, dark symbols) as a function of pressure from our continuous compression experiments at room temperature. The effect of the spin crossover is clearly visible as an enhanced volume reduction. For reference, a third-order Birch-Murnaghan EoS for MgO from Tange et al. (2009) is included (dashed grey line).

4.2. Materials and methods

4.2.1. Experimental details

Powdered samples of $(Mg_{0.604(4)}Fe_{0.396(4)})O$ and $(Mg_{0.409(4)}Fe_{0.591(4)})O$ (hereafter referred to as Fp40 and Fp59) were synthesized from stoichiometric mixtures of MgO and Fe_2O_3. The samples have a face-centered cubic structure at ambient conditions with zero-pressure volumes of 77.08 ± 0.03 Å^3 for Fp40 and 77.88 ± 0.06 Å^3 for Fp59 and $Fe^{3+}/\Sigma Fe$ of 0.071 ± 0.021 in Fp40 and 0.088 ± 0.015 in Fp59 (see appendix C.1 for details on sample synthesis and characterization). To conduct compression experiments at high pressure, symmetric diamond-anvil cells (DACs) were prepared with either 200 µm culet diamonds or 150 µm culet diamonds with beveled anvils. Rhenium gaskets were pre-indented to a thickness of about 30 µm and circular holes of approximately 70 µm and 95 µm in diameter were drilled in the gaskets for anvil culet diameters of 150 µm and 200 µm, respectively. The sample powders were pressed into loose pellets and for each cell a chip with a diameter of about 30-50 µm was loaded onto a diamond culet. A piece of platinum foil was placed on the opposite diamond anvil to serve as pressure marker (Fei et al., 2007a), allowing for

simultaneous XRD measurements of the sample and pressure standard. After the gasket was put in place, neon or helium gas (table 4.1) was loaded into the sample chamber as pressure-transmitting medium (PTM) using the gas-loading setup at beamline P02.2 at PETRAIII, DESY, Germany (Liermann et al., 2015).

Continuous compression experiments in combination with time-resolved XRD measurements (Liermann et al., 2015) were conducted at beamline P02.2 over the course of four beamtimes. Intense monochromatic synchrotron X-ray radiation with a fixed wavelength (table 4.1) was used and XRD images were collected on the fast area detector XRD1621 (Perkin-Elmer) (Liermann et al., 2015). Tilting and rotation of the detector and sample-detector distance were calibrated using a CeO_2 standard (NIST 674b). Pressure in the DACs was increased remotely using a gas-membrane system. By increasing the membrane-pressure at a controlled rate we could continuously compress the sample, while simultaneously collecting time-resolved XRD measurements with single image exposure times of 1-3 s (table 4.1). In each experimental run, the sample was first pre-compressed to the starting pressure using the membrane. Before starting the compression experiment, a fine grid was measured around the center of the sample chamber to find a position with optimal peak intensity ratio between sample and pressure standard.

Table 4.1 Summary of experimental runs

Run nr.	Culet size (µm)	Sample	PTM[a]	λ (Å)	Beam size[b] (µm)	SDD[c] (mm)	Exposure time (s)	Pressure range (GPa)	Max. compression rate (GPa/s)	Nr. of patterns
#1	200	Fp40	He	0.2905	2 x 2	401.5	2	5.6 - 17.1	0.07	250
								18.5 - 98.1	0.05	1729
#2	150	Fp40	He	0.2905	2 x 2	401.5	2	8.0 - 21.3	0.08	100
								22.3 - 84.5	0.09	761
								89.3 - 136.5	0.06	700
#3	200	Fp59	He	0.2906	2 x 2	412.1	2	8.4 - 29.3	0.14	62
								30.2 – 56.9	0.09	238
								59.6 - 80.5	0.07	298
#4	200	Fp59	He	0.2900	2 x 2	401.5	3	73.5 - 90.8	0.04	171
#5[d]	150	Fp59	Ne	0.4845	3 x 8	399.5	1	89.3 - 134.4	0.06	1250

[a]PTM = Pressure-Transmitting Medium
[b]Beam size at FWHM
[c]SDD = Sample Detector Distance
[d]Rhenium gasket with an insert of $Fe_{0.79}Si_{0.06}B_{0.15}$ metallic glass (Dong et al., 2022)

XRD patterns were monitored during compression to ensure data quality, since deformation of the sample chamber with increasing pressure can move the sample out of the beam or cause parasitic rhenium peaks to appear. If this happened, compression was stopped and a new grid was measured to return to a better position. We collected quasi-continuous compression data on both sample compositions covering pressures from 8 GPa to 135 GPa in five experimental runs. Pressure increased by about 10-60 GPa in individual compression runs and the maximum compression rates reached in the experiments were less than 0.15 GPa/s (table 4.1).

The measured diffraction images were integrated and background-corrected using the program Dioptas (Prescher & Prakapenka, 2015). The peak positions and peak widths of the ferropericlase sample and platinum were extracted from the diffraction patterns using a Python code for batch-processing of time-resolved XRD data (Wang, 2022). Although peak overlap prevented us from using the same reflections of sample and pressure standard across the full pressure range of the experimental runs, we ensured that multiple peaks could be fitted in all collected diffraction patterns and used to determine pressure and sample unit-cell volume. We used 4-7 reflections (i.e., at least four out of $(111)_{Pt}$, $(200)_{Pt}$, $(220)_{Pt}$, $(311)_{Pt}$, $(222)_{Pt}$, $(400)_{Pt}$, $(420)_{Pt}$, $(422)_{Pt}$ and $(333)_{Pt}$) to calculate the average unit-cell volume of platinum, weighted by the uncertainty of the peak-fit. A third-order Birch-Murnaghan EoS was employed to derive experimental pressures using the parameters from Fei et al. (2007a). The unit-cell volume of ferropericlase was derived from 3-6 reflections (i.e., at least three out of $(200)_{Fp}$, $(220)_{Fp}$, $(311)_{Fp}$, $(400)_{Fp}$, $(420)_{Fp,}$ and $(422)_{Fp}$), assuming a cubic crystal structure (fig. C.1, appendix C.2) and uncertainties were estimated from the standard deviation of the weighted average volume.

4.2.2. Mixture Density Networks

Since uncertainties are inherent to experimental measurements, inferring the P-V-X_{Fe} relationship from experimental data is a probabilistic inverse problem and the solution is the posterior probability density function (pdf) for volume. We seek to solve this inverse problem using a neural network-based approach called Mixture Density Network (MDN) (Bishop, 1995), where a conventional feed-forward neural network is combined with a Gaussian mixture model to find the

posterior pdf at a given pressure and iron content (Rijal et al., 2021), as shown schematically in figure C.2. MDNs are flexible and can approximate arbitrary pdfs, making them well-suited to investigate the compression behaviour of ferropericlase across the spin crossover.

Collated experimental P-V-X_{Fe} data for ferropericlase from this study and literature (table 4.2, fig. C.4, appendix C.3) is used to train the MDNs. Training (≈ 70%), monitoring (≈ 20%) and test (≈ 10%) sets are randomly generated from the total data set. The loss function used to compute the difference between output and target is described in detail in Rijal et al. (2021). Once training of an MDN begins, this function is summed over all data in the training set to provide the average training error and minimized iteratively. The same error function is used to calculate monitoring and test set errors. The monitoring set is used to monitor overfitting of the training data by the MDN. The test set is not seen by the network during training and is used to evaluate the prediction performance of the trained MDN and assign a weight to it. We train a large number of MDNs (10^3) and combine their predicted pdfs by a weighted sum (Rijal et al., 2021). See appendix C.3 for details on the setup and training of the MDNs.

To compile the data set of P-V-X_{Fe} data on $(Mg_{1-x}Fe_x)O$ used to train the MDNs any rhombohedral unit-cell volumes reported in previous studies were normalized to the number of atoms in a cubic unit-cell (i.e., 8 atoms). Experimental uncertainties are propagated through the MDNs by drawing nine random vectors from the Gaussian distribution defined from the uncertainty range of the data and adding them to the input data, thus decupling the size of the data set. If no uncertainties were reported in previous studies we assumed standard deviations of 0.01 for x_{Fe} and 0.1% of the reported values for unit-cell volumes, while the following values were used for pressure: 0.001 GPa for $P \leq 0.1$ GPa, 0.1 GPa for $P \leq 5$ GPa, 0.5 GPa for $P \leq 25$ GPa, 1 GPa for $P \leq 50$ GPa and 2 GPa for $P > 50$ GPa.

The isothermal bulk modulus K_T can be directly derived from the pressure-volume curve using the identity: $K_T = -V \cdot \left(\frac{\partial P}{\partial V}\right)_T$. To constrain K_T of ferropericlase from the P-V-X_{Fe} relationships predicted by the MDNs, we calculate the conditional mean volume for any given pressure and iron content from each trained MDN, corresponding to the output of a feed-forward neural network.

Table 4.2. Experimental details of studies reporting XRD data on $(Mg_{1-x}Fe_x)O$ used to train the MDNs

Reference	Fe content (at.%)	Pressure device	Pressure scale[a]	Pressure-transmitting medium	Sample type[b]	High-T annealing	Nr of data
Chen et al. (2012)	33	DAC	RF	Ne	Pd	-	36
Fei et al. (1992)	40	DAC	Au, RF	Ne	Pd	-	2
Fei et al. (2007b)	20, 39, 58	DAC	NaCl	NaCl	Pd	To 1600 K	150
Glazyrin et al. (2017)	4, 6, 9, 19, 33	DAC	RF	Ne	SC	-	77
Hamada et al. (2021)	40	DAC	RF, DR	KCl / Kbr / none	Pd	-	11
Jacobsen et al. (2002)	6, 27, 56	DAC	Quartz	4:1 methanol:ethanol	SC	-	22
Jacobsen et al. (2005)	27	DAC	RF	He	SC	-	16
Kantor et al. (2006)	20	DAC	RF	none	Pd	< 1000 K	27
Komabayashi et al. (2010)	19	DAC	Au	NaCl	Pd	To 1300 K	31
Lin et al. (2005)	17, 60	DAC	Pt	Ne	Pd	-	73
Mao et al. (2011)	25	DAC	Au	KCl / NaCl	Pd	To 1200 K	58
Marquardt et al. (2009a)	10	DAC	RF	Ne	Pd	-	29
Matsui et al. (2012)	17, 25	Multi-Anvil	Au	Cr-doped MgO	Pd	To 1100 K	26
Méndez et al. (2022)	10, 20	dDAC	Pt	Ne	Pd	-	1109 / 121[c]
Richet et al. (1989)	59	DAC	RF	Ar	Pd	-	17
Rosenhauer et al. (1976)	40	DAC	NaCl	?	Pd	-	10
Solomatova et al. (2016)	48	DAC	RF	Ne	Pd	-	45
Speziale et al. (2007)	20	DAC	RF	Ar / 16:3:1 methanol:ethanol:water	Pd	To 450 K	30
Westrenen et al. (2005)	36	Multi-Anvil	Au, MgO	Cr-doped MgO	Pd	>1473 K	3
Yang et al. (2015)	6	DAC	Au	Ne	SC	-	44
Yang et al. (2016)	8	DAC	Au	Ne	SC	-	29
Zhang and Kostak (2002)	40	Multi-Anvil	NaCl	Amorphous boron + epoxy resin	Pd	To 1273 K	10
Zhuravlev et al. (2010)	39	DAC	RF	Ne	Pd	-	71
This study	40, 59	DAC	Pt	Ne / He	Pd	-	5559 / 353[c]

[a]RF = Ruby Fluorescence, DR = Diamond Raman shift
[b]SC = Single Crystal, Pd = Powder
[c]Before / after data binning, see appendix C.3

Then we obtain the derivative of the *V(P)* curve by perturbing pressure, allowing us to compute K_T (Rijal et al., 2021). Since we have trained 10^3 networks, we can estimate uncertainty from the spread in the derived K_T values and calculate the weighted average using the weights obtained from the test set error.

4.3. Results and discussion

4.3.1. Compression behaviour of $(Mg_{0.60}Fe_{0.40})O$ and $(Mg_{0.41}Fe_{0.59})O$

The collected quasi-continuous compression curves of $(Mg_{0.60}Fe_{0.40})O$ and $(Mg_{0.41}Fe_{0.59})O$ are shown in figure 4.1b. We observe an enhanced volume contraction during the compression of both Fp40 and Fp59, which is attributed to the spin crossover of Fe^{2+}. The presence of ~8% Fe^{3+} in both Fp40 and Fp59 is expected to reduce the measured volumes slightly with respect to stoichiometric $(Mg_{1-x}Fe_x)O$ (Jacobsen et al., 2002). Such Fe^{3+}-contents are common for Fe-rich ferropericlase samples and may well exist at lower mantle conditions (Sinmyo et al., 2008b). We note that the two compression runs on Fp40 are in excellent agreement above approximately 30 GPa, but they deviate at lower pressures, which is highlighted by the high data density obtained in our time-resolved XRD measurements. Given that experimental conditions were the same for both runs, this warrants further investigation. We calculate normalized stress *F* as a function of Eulerian strain *f* ('*F-f* plots', fig. 4.2a,b), where $f = 0.5\,(\frac{V_0^{\frac{2}{3}}}{V} - 1)$ and $F = \frac{P}{3f(1+2f)^{5/2}}$ (Angel, 2000; Stacey et al., 1981), from the obtained XRD data on Fp40 and Fp59. We find that both compression runs on Fp40 show anomalies in the material compressional behaviour up to 30 GPa (fig. 4.2c), which can be attributed to deviatoric stresses in the sample and/or pressure marker that occur if the stress in the pressure medium is unequally distributed between different stress tensor components in the sample/pressure marker (Glazyrin et al., 2016). The high compressibility of a helium PTM, which was used in both Fp40 experiments, leads to significant shrinkage of the gasket hole and irregular deformation of the sample chamber is known to lead to complex stress states (Takemura, 2021). In addition, this may have resulted in the sample or pressure marker bridging the walls of the sample chamber, leading to larger deviatoric stresses than expected for a helium PTM. As a result, the

pressure recorded by the pressure marker does not correspond exactly to the pressure exerted on the sample, producing the irregular compression curves of the two Fp40 runs at low pressures. However, these inconsistencies disappear above 30 GPa, which indicates a reduction of deviatoric stresses. The *F-f* relation is also a useful tool to detect and investigate the spin crossover, which manifests as a gradual decrease in normalized stress with increasing Eulerian strain (e.g. Glazyrin et al., 2016; Solomatova et al., 2016). When normalized stress is plotted as a function of pressure, the onset and completion pressures of the spin crossover become apparent (fig. 4.2c,d). For Fp40 the spin crossover occurs over a pressure range of about 50–85 GPa, whereas for Fp59 it shifts to higher pressure and broadens to about 60–110 GPa.

While ferropericlase has a cubic B1 crystal structure at ambient pressure, it has been reported to undergo a rhombohedral distortion at high pressures that is more prominent in iron-rich compositions and is sensitive to non-hydrostatic conditions (Finkelstein et al., 2017; Kantor et al., 2006; Zhuravlev et al., 2010). The cubic–rhombohedral ($Fm\bar{3}m$–$R\bar{3}m$) transition leads to splitting of the $(111)_{\text{Fp-cubic}}$ and $(220)_{\text{Fp-cubic}}$ peaks, whereas the $(200)_{\text{Fp-cubic}}$ and $(400)_{\text{Fp-cubic}}$ peaks are not affected. While we did not observe any peak splitting in the measured XRD images, analysis of the Full-Width-at-Half-Maximum (FWHM) of the fitted peaks showed peak broadening of the $(220)_{\text{Fp-cubic}}$ for both Fp40 and Fp59 compositions at about 30 GPa (fig. 4.2e,f). We interpret this as the onset of a rhombohedral distortion, but the transition does not lead to any obvious changes in the compression behaviour of ferropericlase (fig. 4.1b), in agreement with previous reports on samples with similar or higher iron contents (Fei et al., 2007b; Finkelstein et al., 2017; Zhuravlev et al., 2010). In the FeO endmember of the (Fe,Mg)O solid solution the rhombohedral distortion occurs at approximately 20 GPa (Jacobsen et al., 2005). The addition of MgO extends the stability field of the cubic phase to higher pressures, but the transition pressure decreases with non-hydrostaticity (e.g. Finkelstein et al., 2017; Kantor et al., 2006). The transition pressure observed in the runs on Fp40 coincides with the pressure at which anomalies in the compressional behaviour disappear (fig. 4.2c), suggesting that the rhombohedral distortion helps to reduce deviatoric stresses in the sample.

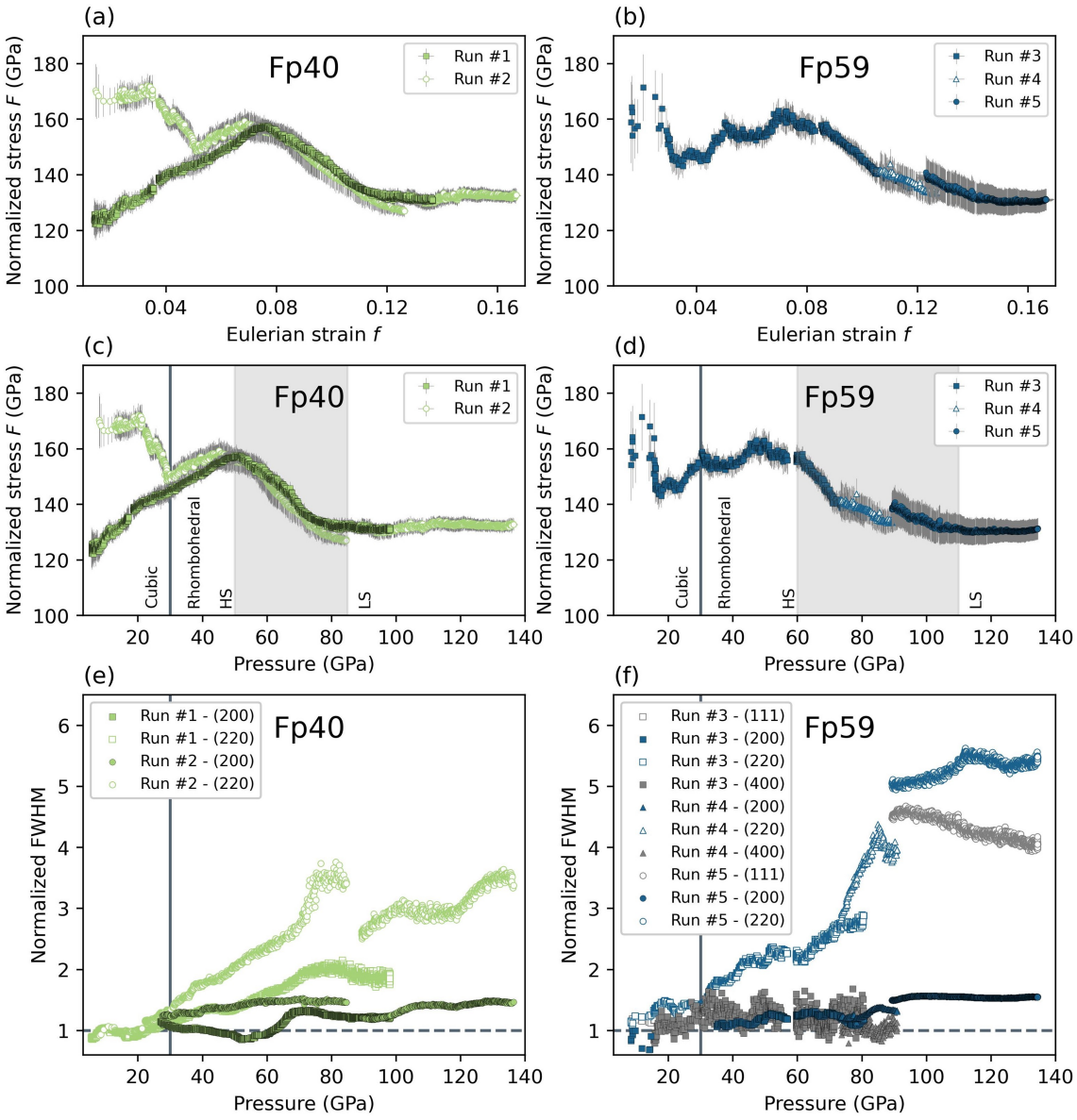

Figure 4.2 (a, b) Normalized stress *F* as a function of Eulerian strain *f* of experimental runs on Fp40 and Fp59, respectively. (c, d) Normalized stress as a function of pressure for Fp40 and Fp59, respectively. A gradual reduction in normalized stress from approximately 50 GPa to 85 GPa for Fp40 and 60 GPa to 110 GPa for Fp59 is attributed to the iron spin crossover, indicated by the grey shaded area. Anomalous trends in the normalized stress below 30 GPa are an indication for deviatoric stresses that appear to be reduced by the cubic-rhombohedral transition (grey solid line). (e, f) Normalized FWHM of fitted diffraction peaks as a function of pressure for Fp40 and Fp59, respectively. The FWHM of fitted peaks is normalized to the FWHM at ambient pressure and shows a larger broadening for the (111) and (220) reflections compared to the (200) and (400) reflections above 30 GPa, which is interpreted as the onset of the rhombohedral distortion indicated by a grey solid line.

4.3.2. *P-V-X_{Fe}* Relationship of $(Mg_{1-x}Fe_x)O$

To investigate *P-V-X_{Fe}* relationships of ferropericlase we combine our experimental results with previously published high-pressure XRD data on $(Mg_{1-x}Fe_x)O$ with x_{Fe} = 0.04–0.60 (Chen et al., 2012; Fei et al., 1992; Fei et al., 2007b; Glazyrin et al., 2017; Hamada et al., 2021; Jacobsen et al., 2002; Jacobsen et al., 2005; Kantor et al., 2006; Komabayashi et al., 2010; Lin et al., 2005; Mao et al., 2011; Marquardt et al., 2009a; Matsui et al., 2012; Méndez et al., 2022; Richet et al., 1989; Rosenhauer et al., 1976; Solomatova et al., 2016; Speziale et al., 2007; Westrenen et al., 2005; Yang et al., 2015; Yang et al., 2016; Zhang & Kostak, 2002; Zhuravlev et al., 2010) (figs. 4.1 & C.4, appendix C.3). Experimental approaches vary widely between studies (table 4.2) and although the compiled data show a clear trend overall, quantitative differences and inconsistencies are apparent, limiting the robustness in obtained *P-V-X_{Fe}* relationships. To map out how iron content affects the elastic behaviour of ferropericlase across the spin crossover we have employed machine learning techniques, that allow comprehensive integration of all existing experimental results and unbiased uncertainty quantification of the inferred relationship.

The MDN-predicted unit-cell volume pdfs for different iron contents are presented in figure 4.3. The fit between the training data and the pdfs is shown in figure C.5. The effect of the spin crossover is clearly visible for all compositions as an enhanced volume contraction, with the onset shifting to higher pressures with iron content. At pressures below the spin crossover the compression curves of all $(Mg_{1-x}Fe_x)O$ compositions closely follow the trend of the EoS of MgO (Tange et al., 2009), but they are shifted to higher volumes with increasing iron content. This indicates that the unit-cell volume of HS ferropericlase increases with increasing iron content and can be attributed to HS Fe^{2+} having a larger ionic radius than Mg^{2+} (Shannon, 1976). However, as Fe^{2+} transitions from HS to LS state its ionic radius is reduced, leading to a reduction in the unit-cell volume of ferropericlase. With increasing pressure, the fraction of LS iron rises and the predicted ferropericlase volumes gradually drop below the compression curve of MgO (fig. 4.3), suggesting that LS Fe^{2+} has a smaller ionic radius than Mg^{2+} at high pressure, as noted before by

Glazyrin et al. (2017). The completion of the spin crossover is indicated by the predicted compression curves following the trend of MgO again, albeit shifted to slightly lower volumes.

The width of the posterior volume pdfs predicted by the MDNs is an indication for uncertainty and is expected to be greater in regions where experimental data coverage is sparse, measurement errors are high or where discrepancies between published data are large. For all compositions, the pdfs are wider in the spin crossover pressure range (fig. 4.3). Glazyrin et al. (2016) suggested that the spin crossover is sensitive to nonhydrostatic stresses, which may lead to a larger data spread in this region and explain the greater uncertainties. The pdfs for x_{Fe} = 0.4 and x_{Fe} = 0.6 are comparatively wide and bimodal between approximately 5–35 GPa, which is caused by large discrepancies between data sets from different studies (fig. C.4).

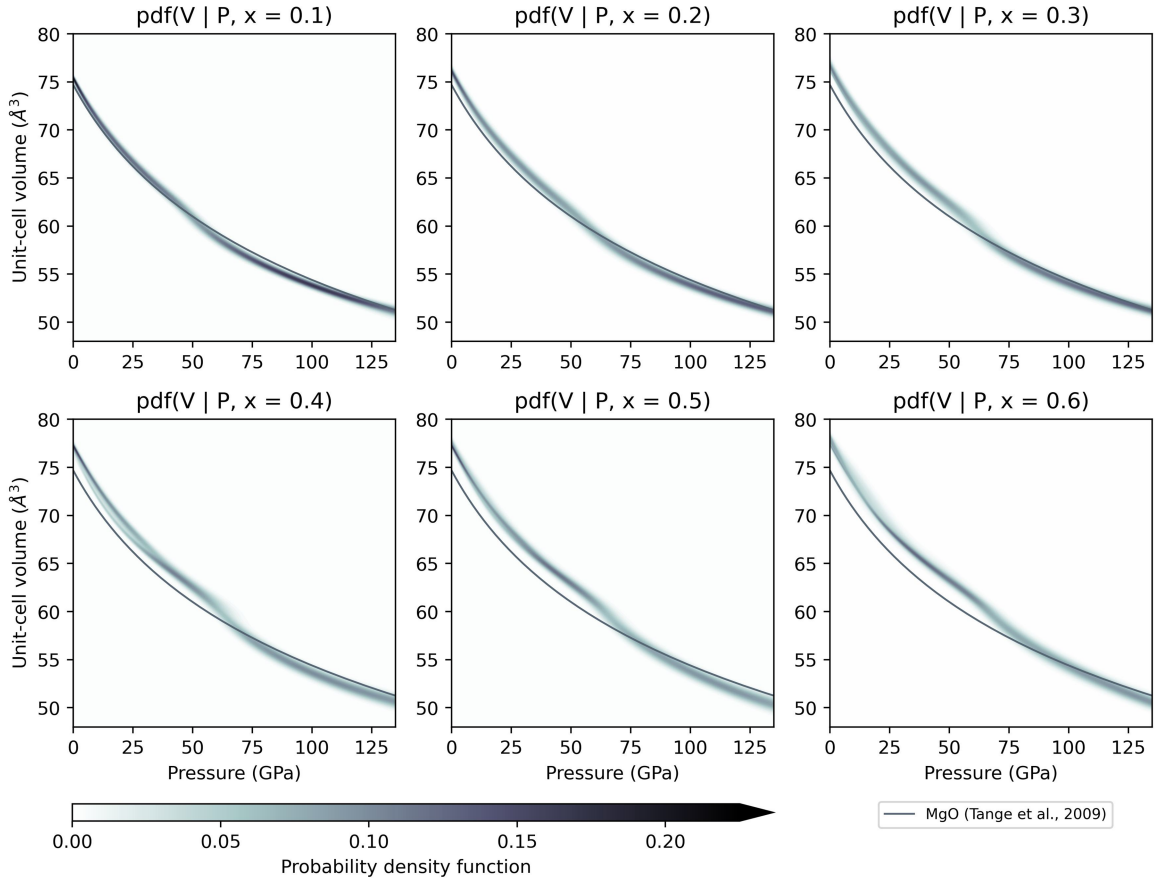

Figure 4.3 Pdfs for the unit-cell volume of $(Mg_{1-x}Fe_x)O$ as a function of pressure predicted by MDNs for different iron contents. The MDNs were trained using experimental high-pressure data with x_{Fe} = 0.04-0.6. The colour scale corresponds to the value of the pdfs and the EoS of MgO (Tange et al., 2009) is shown as a grey line for reference.

The larger ionic radius of HS Fe^{2+} compared to Mg^{2+} (Shannon, 1976) may make the volume of iron-rich ferropericlase more sensitive to non-hydrostatic stresses at pressures below the spin crossover, with the rhombohedral distortion helping to accommodate these stresses.

4.3.3. Spin crossover-induced bulk modulus softening

Most previous attempts to constrain the bulk modulus across the spin crossover from experimental *V(P)* data are based on fitting the data to fixed functional forms for HS and LS ferropericlase, with inherent biases resulting from the choice of functional, use of priors or prior windows and/or specifying the spin crossover pressure range (e.g. Chen et al., 2012; Lin et al., 2005; Mao et al., 2011; Marquardt et al., 2009a; Solomatova et al., 2016). With our approach, P-V-X_{Fe} relationships are implicitly learned from data during the training of the MDNs and bulk moduli are computed directly from the *P(V)* derivative of the mapping without any *a priori* constraints.

The bulk modulus values obtained from all 10^3 MDNs are plotted as a function of pressure in figure 4.4 as 2D histograms for different iron contents. We find that the values predicted by the networks are largely consistent, producing well-defined $K_T(P)$ curves. However, the spread in values, and thus uncertainty, dramatically increases at high pressures, particularly for compositions where experimental data coverage is sparse. The means and standard deviations of the bulk modulus distributions are shown in figure 4.5b. The deviations between data sets from different studies on $x_{Fe} \approx 0.6$ at pressures <30 GPa (fig. C.4) are captured by the larger uncertainties.

While the bulk moduli inferred by the MDNs are very close to those predicted for MgO (Tange et al., 2009) at low pressures, a spin crossover-induced softening of the bulk modulus is clearly visible with increasing pressure for all compositions. The only experimental constraints on the bulk modulus of ferropericlase not derived from XRD measurements are obtained through spectroscopic methods. With the exception of data from Antonangeli et al. (2011), spectroscopic measurements also show a softening of the bulk modulus across the spin crossover for $x_{Fe} = 0.06$ (Crowhurst et al., 2008) and $x_{Fe} = 0.08$ (Yang et al., 2015). These results are in reasonable agreement with our MDN results for a similar composition ($x_{Fe} = 0.1$, figs. 4.4 and 4.5b).

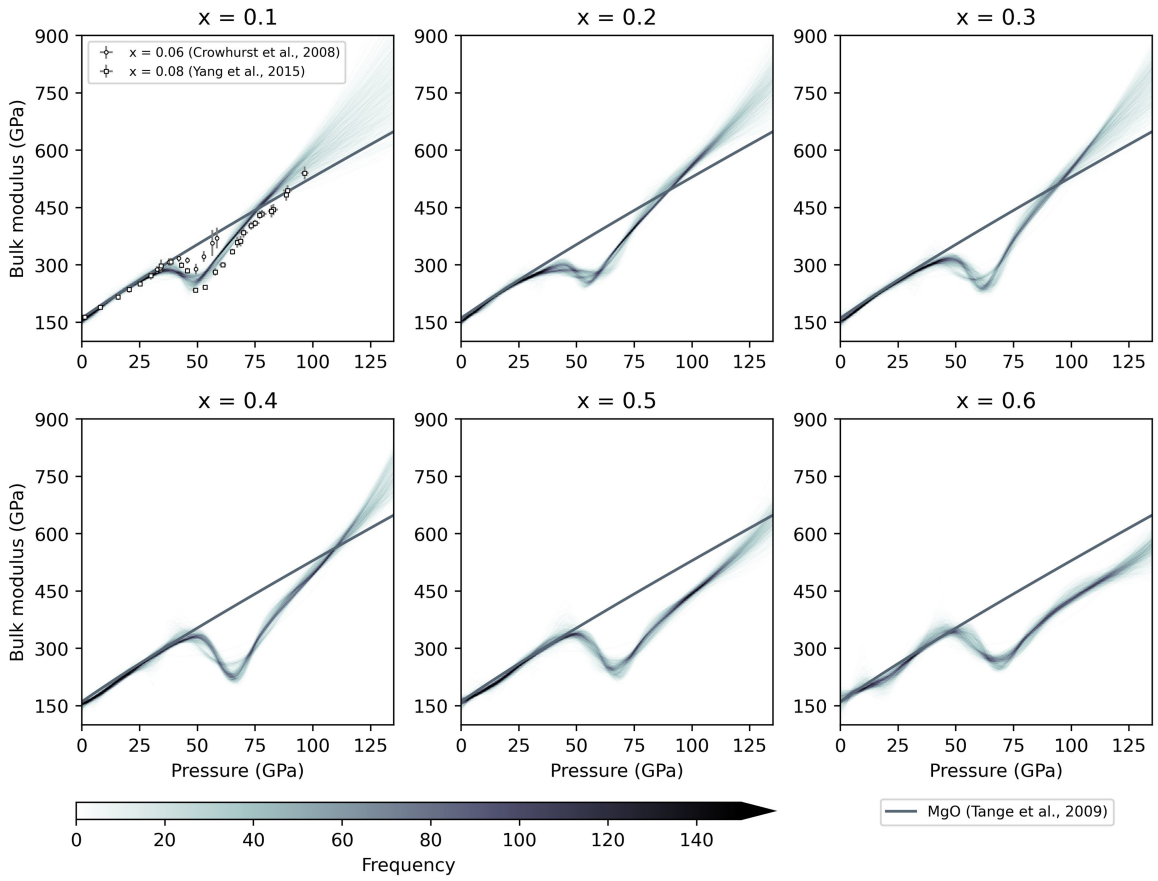

Figure 4.4 Frequency distribution of the isothermal bulk modulus values for $(Mg_{1-x}Fe_x)O$ as a function of pressure predicted by 10^3 trained MDNs for different iron contents. The frequency counts for the predicted values are at intervals of 0.1 GPa for pressure and 2 GPa for bulk modulus and the colour scale corresponds to the number of MDNs predicting that value. The bulk modulus of MgO (Tange et al., 2009) is shown for reference (grey line). Adiabatic bulk modulus values obtained from optical spectroscopy measurements (Crowhurst et al., 2008; Yang et al., 2015) are compared to the MDN-predicted values for $x_{Fe} = 0.1$.

The onset of the spin crossover shifts to higher pressures with increasing iron content by about 15 GPa between $x_{Fe} = 0.05$ and $x_{Fe} = 0.6$. We also observe a broadening of the bulk modulus softening with iron content, indicating an increase in the spin crossover pressure range, qualitatively consistent with previous studies (Solomatova et al., 2016 and references therein). The pressure where the bulk modulus shows the largest softening increases with iron content from 46.0 GPa for $x_{Fe} = 0.05$ to 68.3 GPa for $x_{Fe} = 0.6$. While the correlation between iron content and magnitude of maximal softening is positive for low iron contents, it becomes negative at high iron contents (inset fig. 4.5b). The shape and magnitude of the bulk modulus softening is directly related to the magnitude of the volume reduction between HS and LS states and the pressure range over which it occurs. We find that the degree of maximal softening is largest for $x_{Fe} = 0.4$, which may be the

result of a trade-off between an increase in volume reduction for higher iron contents due to the larger number of iron atoms undergoing a spin transition and a broadening of the spin crossover region, leading to a more gradual decrease in volume with pressure. The broadness of the spin crossover at room temperature is attributed to a favourable enthalpy of mixing ΔH_{mix} of HS and LS iron (Holmström & Stixrude, 2015). The arrangement of iron atoms affects the magnitude of ΔH_{mix}, with LS atoms stabilizing neighbouring on-axis HS atoms to higher pressures (see Méndez et al., 2022). For higher iron contents, the number of neighbouring on-axis iron atoms should increase, which may be the cause of the broadening of the spin crossover region with iron content.

4.4. Geophysical implications

The P-K_T-X_{Fe} relationship of ferropericlase inferred by the MDNs indicates that the effect of the spin crossover on the bulk modulus is largest for $x_{Fe} \approx 0.4$ (inset fig. 4.5b). To assess potential implications for the interpretation of seismological observations of the lower mantle, it must be taken into account that the spin crossover broadens and shifts to higher pressures with temperature (e.g. Trautner et al., 2023; Wu et al., 2013; Yang et al., 2021). Assuming the effects of temperature are comparable for $x_{Fe} = 0.2$ and $x_{Fe} = 0.4$ and using the temperature dependency predicted by Méndez et al. (2022) and Trautner et al. (2023), the maximum bulk modulus softening in $x_{Fe} = 0.4$ would occur at approximately 130 GPa for a mantle temperature of 2,900 K, corresponding to a depth of about 2,750 km. These conditions are similar to those near the CMB along a typical geotherm (Davies et al., 2012), suggesting that the physical properties of a phase assemblage containing moderately iron-enriched ferropericlase at the base of the lower mantle would be markedly affected by the spin crossover. This is an important finding since iron is expected to partition strongly into ferropericlase for iron-rich bulk compositions near the CMB (Muir & Brodholt, 2016) and the presence of iron-enriched ferropericlase in the lowermost mantle has been hypothesized to explain the seismic anomalies observed in ULVZs (e.g. Liu et al., 2016; Otsuka & Karato, 2012; Wicks et al., 2017; Yu & Garnero, 2018).

The compressional (V_P) and bulk (V_C) seismic wave velocities of ferropericlase are strongly affected by the spin crossover (e.g. Crowhurst et al., 2008; Marquardt et al., 2009a; Wu et al.,

2013; Yang et al., 2015), since they directly depend on the bulk modulus: $V_P^2 = \frac{K+\frac{4}{3}G}{\rho}$ and $V_C^2 = \frac{K}{\rho}$, where G is the shear modulus and ρ is density. Calculating compressional wave velocities requires constraints on the shear modulus, but density and bulk velocities can be directly computed from the MDN-predicted mean unit-cell volumes and bulk moduli (fig. 4.5). Uncertainties are propagated from the standard deviations of the volume pdfs (fig. 4.3) and distributions of K_T values (fig. 4.4).

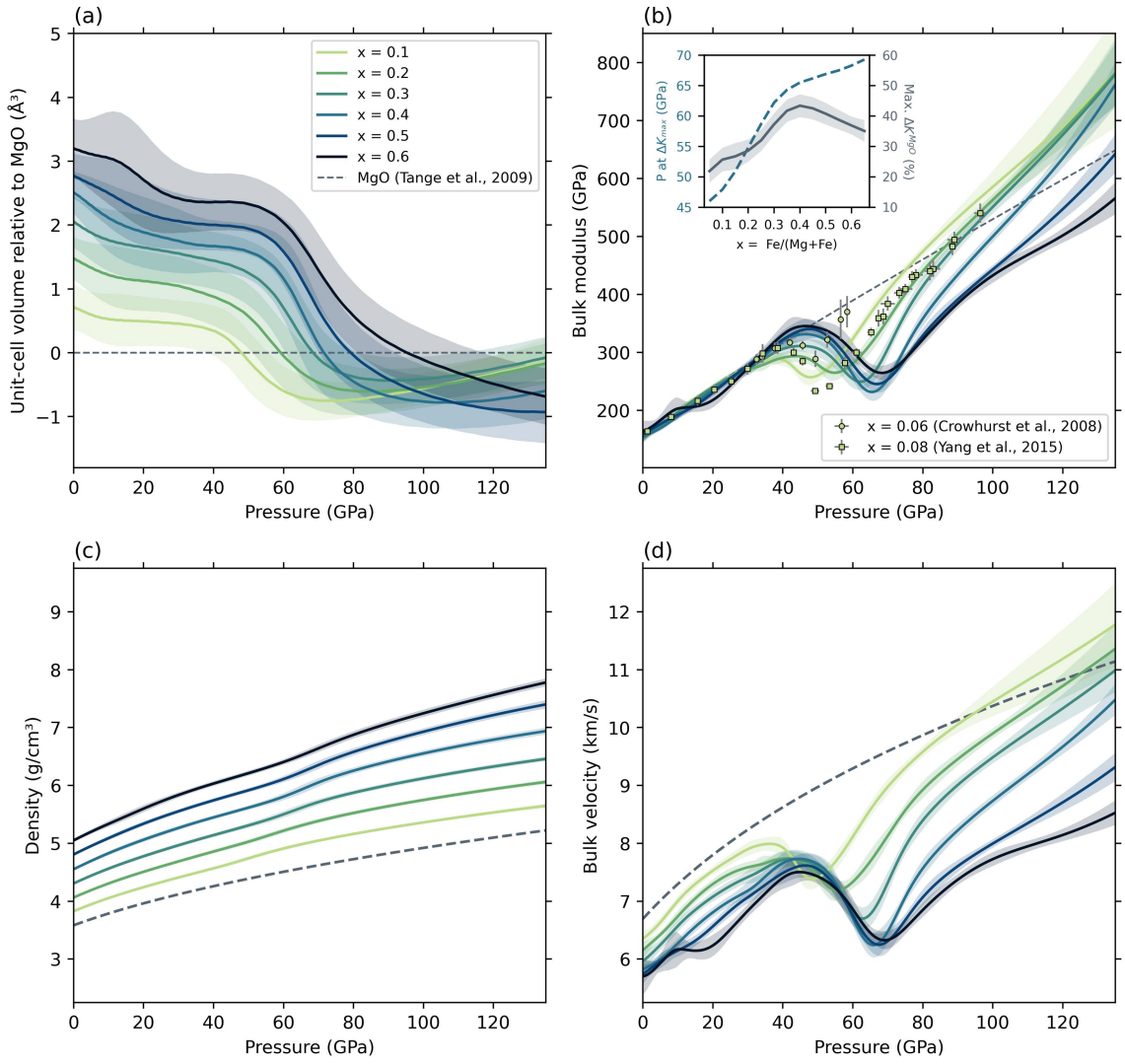

Figure 4.5 MDN predictions of mean (a) unit-cell volume (as difference relative to MgO), (b) isothermal bulk modulus, (c) density and (d) bulk sound velocity of $(Mg_{1-x}Fe_x)O$ as a function of pressure. Colours indicate iron contents and shaded areas correspond to one standard deviation from the mean. Properties for MgO derived from a third-order Birch-Murnaghan EoS (Tange et al., 2009) are shown for reference as dashed grey lines. In (b), adiabatic bulk modulus values obtained from optical spectroscopy measurements (Crowhurst et al., 2008; Yang et al., 2015) are shown for comparison. Inset: percentage of maximal bulk modulus softening with respect to MgO and the corresponding pressure as a function of iron content.

We find that density increases with iron content and that the density contrast between iron-poor and iron-rich ferropericlase is larger at high pressures, i.e., in LS state (fig. 4.5c). Bulk velocities decrease with iron content in HS and LS state and show a similar softening as the bulk modulus in the spin crossover pressure range (fig. 4.5d).

Shear wave velocities (V_S) depend only on shear modulus and density ($V_S^2 = \frac{G}{\rho}$). Previous investigations have shown that the shear modulus of ferropericlase is not sensitive to the spin crossover, systematically increasing with pressure and decreasing with temperature and iron content (Marquardt et al., 2009a; Muir & Brodholt, 2015; Wicks et al., 2017; Yang et al., 2015; Yang et al., 2016). The contrasting effects of the spin crossover on shear velocities versus compressional and bulk velocities result in a characteristically high ratio of V_S over V_P and a strong negative correlation between V_S and V_C (Marquardt et al., 2009a; Trautner et al., 2023). These are features commonly observed in seismic tomography models of the lowermost mantle for which the post-perovskite phase has been suggested as an explanation (Koelemeijer et al., 2018). Our findings of the spin crossover shifting to higher pressures with iron content and amplification of the softening for moderately iron-enriched compositions indicate that the spin crossover may contribute significantly to anomalous seismic features observed at the base of the lower mantle and should be considered in seismic inversions.

The effects of iron enrichment and elevated temperatures on the spin crossover-induced bulk modulus softening are similar in that they both cause a shift to higher pressures and a broadening of the softening. This will complicate the use of the seismic expression of the spin crossover identified in Chapters 2 and 3 to unambiguously constrain temperature variations in a compositionally heterogeneous lower mantle, since there would likely be a trade-off between iron content and temperature during inversion of seismic observations. On the other hand, the effects of temperature and iron content on the bulk modulus softening differ in that increased temperatures lead to a reduction of the amplitude of the softening, while moderately high iron contents increase the amplitude. This difference may aid in disentangling regions with iron enrichment versus high temperatures in the lower mantle. However, to accurately model the effects of iron enrichment on

the seismic properties of ferropericlase at lower mantle conditions, it is essential that the spin crossover is studied at simultaneous high iron contents and high temperatures using experiments and/or theoretical computations in future studies.

4.5. Conclusions

By using machine learning techniques to infer the P-V-X_{Fe} relationship of ferropericlase from a combination of new experimental results and literature data, we show how the effects of the spin crossover on bulk modulus, density and bulk velocity change with iron content. This approach avoids prescribing an explicit functional form and provides us with uncertainties that reflect the consistency between data from different sources, without any potential biases introduced by subjective selection of data or the choice of a particular EoS (Rijal et al., 2021). Our results can improve uncertainty quantification in the interpretation of seismic observations and provide constraints for thermodynamic databases and geodynamic models. The shift of the spin crossover to higher pressures with iron content and the amplified bulk modulus softening for moderate iron contents around $x_{Fe} = 0.4$ suggest that seismic properties of the lowermost mantle may be strongly affected by the spin crossover. Once sufficient data is available, the MDN-based approach applied here can be extended to temperature (T) and used to predict the properties of ferropericlase in P-T-X_{Fe} space. Integrating MDNs with theoretical calculations (e.g. Muir & Brodholt, 2015) and/or physical laws as regularization agents, for example by combining them with Physics-Informed Neural Networks (Raissi et al., 2019) may provide additional constraints.

Chapter 5. Compression behaviour of a polycrystalline assemblage of bridgmanite and ferropericlase at lower mantle temperatures

Preface

This chapter presents experimental results on the compression of a polycrystalline aggregate of ferropericlase and bridgmanite at room temperature and high temperature. The contents of this chapter have not yet been published, but it has been written as an article intended for a scientific journal, in keeping with the integrated format of this thesis.

My contributions include preparing and conducting the experiments, processing and analysis of the data, data visualization and writing of the manuscript. The sample was provided by Hongzhan Fei, facilitated by Biao Wang. Egor Koemets, Niccolo Satta, Biao Wang, Johannes Buchen and Nico Giordano assisted with preparing and conducting the experiments. Gareth Hughes, Estelle Ledoux and Katharina Marquardt provided support for EDS-SEM analysis of the run products. Hauke Marquardt supervised the project and provided funding.

Supplementary material is included in Appendix D.

Abstract

Earth's lower mantle consists predominantly of bridgmanite and ferropericlase, forming poly-crystalline aggregates. The bulk elastic and rheologic behaviour of multi-phase materials depend on how stress and strain are partitioned between individual phases with differing elastic properties. Although the elastic behaviour of single-phase bridgmanite and ferropericlase have been studied extensively, the effects of stress-strain partitioning between these minerals in a polycrystalline aggregate are not well-understood. To determine seismic wave speeds of lower mantle rocks, the bulk elastic behaviour is often approximated by calculating iso-strain and iso-stress bounds from the elastic properties of the constituent minerals. However, a lack of understanding of how to appropriately average these bounds hampers a unique interpretation of seismic observations.

Here, we investigate the compression behaviour of a sintered polycrystal of bridgmanite and ferropericlase with an approximate volume proportion of 7:3 at lower mantle pressures. We present experimental results at 300 K, with and without temperature annealing, and at 1,800 K. Bridgmanite forms a load-bearing framework at ambient temperature, decreasing the strain rate of ferropericlase relative to single-phase results and causing the iron spin crossover to occur at higher pressures. Heating at 1,800 K results in both bridgmanite and ferropericlase deforming in accordance with the compression behaviour observed in single phase experiments, indicating homogenization of stresses. Our findings suggest that stress-strain partitioning in multi-phase materials varies strongly with temperature, underlining the importance of studying the deformation of multi-phase mantle materials at relevant pressure and temperature conditions to get accurate constraints for geophysical studies.

5.1. Introduction

Knowledge of the physical properties of the materials constituting Earth's deep interior is essential for both geodynamic modelling and seismic inversions, which can provide important information on the thermochemical structure of the mantle (e.g. Ballmer et al., 2017; Cobden et al., 2024; Davies et al., 2012; Deng et al., 2023; Gülcher et al., 2021; Mosca et al., 2012). High-pressure/high-temperature experiments and theoretical computations are used to determine the properties of minerals at the extreme conditions of the deep Earth. Such studies typically focus on single-phase, homogeneous materials. However, the mantle is made of multi-phase materials, consisting of a variety of minerals with different elastic properties (e.g. Irifune & Tsuchiya, 2015; Stixrude & Lithgow-Bertelloni, 2024). Understanding the relation between the properties of individual minerals and average elastic and rheological properties of a multi-phase aggregate (Karato, 2008) is key for the interpretation of seismic observations and modelling of geodynamic processes.

The Voigt and Reuss bounds represent two endmember models for the average elastic behaviour of a multi-phase aggregate (Karato, 2008; Reuss, 1929; Voigt, 1928). The Voigt bound assumes that strain is homogeneously distributed throughout the material, so that the volume of each crystal in the aggregate changes by the same fraction. In the case of elastic deformation, stress and strain are linearly related through the elastic constants of a mineral. For a multi-phase aggregate, with contrasting elastic properties of the constituent minerals, homogeneous strain will therefore result in a heterogeneous stress distribution. The Reuss bound, on the other hand, assumes that the imposed external stress field is homogeneous throughout a material. In this case, the stress state of each crystal in the aggregate will be the same, but the amount of strain will vary between phases. The sound wave velocities of multi-phase materials are governed not only by volume fraction and the geometry of the constituent phases, but also by the stress-strain distribution (Watt et al., 1976). Wave velocities of lower mantle materials can be estimated by calculating the Voigt (iso-strain) and Reuss (iso-stress) bounds, but the resulting velocity variations are around 0.5-1% (Buchen, 2021). The arithmetic mean of the bounds (Voigt-Reuss-Hill average) (Hill, 1952) is most

frequently used to approximate the elastic behaviour of a polymineralic rock, but this average is not based on any physical laws. In addition, stress-strain partitioning may well vary with temperature and the frequency of seismic waves (Buchen, 2021). The lower mantle consists predominantly of bridgmanite (~75%) and ferropericlase (~18%) (Irifune et al., 2010). The compression behaviour of the single crystals and powders of these minerals have been studied extensively (e.g. Ballaran et al., 2012; Catalli et al., 2010; Criniti et al., 2021; Lin et al., 2005; Marquardt et al., 2009a; Trautner et al., 2023; Wolf et al., 2015), but the effects of stress and strain partitioning in bridgmanite-ferropericlase aggregates are not well-understood (Buchen, 2021). Understanding how to average the elastic bounds of an aggregate of bridgmanite and ferropericlase is therefore key to a successful inversion of seismic observations of the lower mantle.

Whether a material deforms plastically or elastically depends on the strength of the material. Handy (1994) outlined two endmember scenarios to place bounds on the plastic deformation of a two-phase aggregate with a strength contrast between the phases: the load-bearing framework and the interconnected weak layer. The bulk strength of the aggregate depends not only on the rheological properties of the individual phases, but also on the interconnectivity of the weaker or stronger phase (which in turn depend on microstructure and phase proportions). In the case of a load-bearing framework, stress is concentrated in the harder phase, which imposes its strain rate on the softer phase (i.e. similar to an iso-strain scenario). The interconnected weak layer, where strain is concentrated in the weaker phase, is closer to the iso-stress scenario. While measuring the strength of bridgmanite and ferropericlase at lower mantle conditions is difficult, bridgmanite is generally thought to be stronger than ferropericlase (Girard et al., 2016; Immoor et al., 2022; Miyagi & Wenk, 2016). Bridgmanite is the most voluminous phase in the lower mantle and if it forms a load-bearing framework its strength would govern the rheology of the lower mantle. However, it has been suggested that for large strain, ferropericlase forms an interconnected weak layer (Girard et al., 2016). If this were the case, ferropericlase might control the strength of materials in high strain regions of the mantle, such as in and around down-going slabs (Marquardt & Miyagi, 2015) and rising plumes, which would likely lead to shear localization. This has major

implications for mantle convection and the preservation of geochemical reservoirs: mass transport would be focussed into ferropericlase-dominated shear zones, while the rest of the mantle would have a higher viscosity, controlled by the strength of bridgmanite, and deform very little (Ballmer et al., 2017; Girard et al., 2016).

It is evident that stress-strain partitioning in polymineralic lower mantle rocks is a key factor in seismic wave propagation and mantle dynamics. An improved understanding is required to scale from experimental measurements of elastic and rheological properties of the individual minerals to bulk properties of mantle rocks. Here, we present compression data of a sintered polycrystal of bridgmanite and ferropericlase, approximating lower mantle materials, at ambient and lower mantle temperatures. We investigate the compression behaviour of the two-phase aggregate with and without stress-annealing. We discuss the implications for stress and strain partitioning and show how this affects the iron spin crossover in ferropericlase.

5.2. Materials and methods

5.2.1. Preparation of materials

To investigate the deformation behaviour of multi-phase lower mantle rocks we conducted compression experiments on sintered aggregates of bridgmanite and ferropericlase with sub-micron grain sizes. Detailed synthesis procedures are described in Fei et al. (2021) and can be summarized as follows: San Carlos olivine single crystals with an approximate composition of $(Mg_{0.91}Fe_{0.09})_2SiO_4$ were ground to a powder. This starting material should produce bridgmanite and ferropericlase in a molar ratio of 1:1 (i.e. $(Mg,Fe)_2SiO_4 \rightarrow (Mg,Fe)SiO_3 + (Mg,Fe)O$), corresponding to an expected volume ratio of approximately 7:3. Layers of olivine powder, separated by iron foils, were loaded in a platinum capsule. Small amounts of Fe-FeO (iron-wüstite buffer) were loaded next to the iron foils to buffer oxygen fugacity. The assembly was compressed to 27 GPa using a multi-anvil press and then heated to 1700 K, where it was kept for 5 minutes. Subsequently, the assembly was quenched to room temperature and slowly decompressed. The synthesized two-phase aggregates of bridgmanite and ferropericlase were recovered from the capsule, polished to a thickness of approximately 10 μm and broken into pieces of <40 μm.

Two diamond-anvil cells (DACs) with 200 µm culet size diamonds were prepared by pre-indenting rhenium gaskets to a thickness of ~30 µm and drilling a circular hole of ~90 µm in diameter. A piece of two-phase sample and a small piece of platinum foil, serving as pressure marker, were loaded in the centre of the diamond culet of one of the cells (RT1), before loading helium as a pressure-transmitting medium (PTM) using the gas-loading setup at beamline P02.2 at PETRA III, DESY, Germany (Liermann et al., 2015). After the gas-loading, the pressure in the cell was ~8 GPa and the sample chamber had shrunk to a diameter of ~50 µm; nevertheless, the sample remained isolated from the gasket (fig. 5.1a). Helium solidifies at 11.8 GPa at 298 K (e.g. Datchi et al., 2000) and above this pressure further shrinkage is expected to be small (Mao et al., 1988). This was visually verified during the compression experiment and quasi-hydrostatic conditions were thus maintained throughout the experiment. The second cell (LH1) was loaded with a piece of platinum foil as pressure marker on one of the diamond culets and a piece of sample, sandwiched between two layers of KCl of ~10 µm thickness (fig 5.1b). KCl served as both PTM and to insulate the sample from the diamonds during laser-heating.

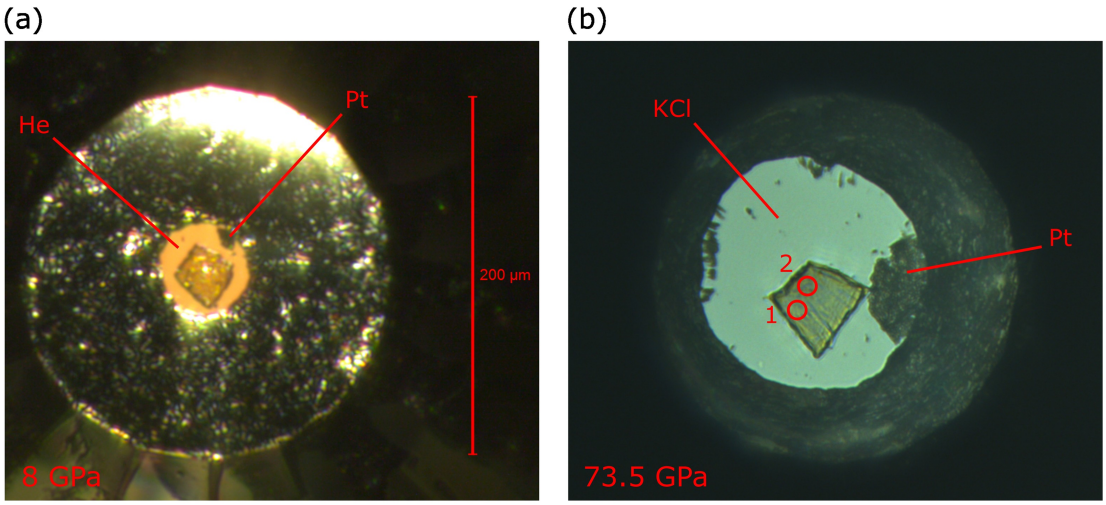

Figure 5.1 Micrographs of the loadings of the two cells used for the compression experiments. (a) Cell RT1 after gas-loading with helium (He), loaded with a piece of sintered bridgmanite-ferropericlase aggregate and a piece of platinum (Pt) foil as pressure standard. (b). Cell LH1 after compression to 73.5 GPa, loaded with a piece of sample, platinum foil and KCl. The two red circles indicate the spots that were laser-heated at 1,800 K (1) and 2,200 K (2).

5.2.2. Compression experiments

The cells were compressed remotely using a gas-membrane system at beamline P02.2. XRD images were collected parallel to the compression axis of the DACs on the fast area detector XRD1621 (Perkin-Elmer) (Liermann et al., 2015), with a sample-detector distance of 412.1 mm. Tilting and rotation of the detector and sample-detector distance were calibrated using a CeO_2 standard (NIST 674b). Intense monochromatic synchrotron xX-ray radiation with a fixed wavelength of 0.2906 Å was used and a beam size of ~2x2 μm^2 at FWHM. The sample in cell LH1 was heated to high temperatures using a double-sided on-axis laser-heating system with a Yb-fiber laser available at beamline P02.2 (Liermann et al., 2015). The heating spot had a diameter of ~10 μm and heating from both sides ensured the sample was heated uniformly along the axis of the X-ray beam. Temperatures were monitored using pyrometry of the light emitted from the hot sample (Liermann et al., 2015).

The diffraction patterns of the two-phase sample are complicated, since bridgmanite has an orthorhombic crystal structure (space group *Pbnm*) with a large number of diffraction peaks, that partially overlap with the peaks from face-centred cubic ferropericlase (space group $Fm\bar{3}m$) (fig. 5.2). To keep fitting of the diffraction patterns as straightforward as possible, platinum that served as pressure marker was placed next to the samples, rather than below it (fig. 5.1). Consequentially, however, it is not possible to measure pressure marker and sample simultaneously. Therefore, the cells were compressed in a stepwise fashion. The following measurement protocol (P1) was repeated during compression of cell RT1:

1. Increase pressure by ~2 GPa using the gas membrane;
2. Let pressure stabilize for a few minutes;
3. Take diffraction image at the position of the pressure marker;
4. Take diffraction image at the position of the sample;
5. Take diffraction image at the position of the pressure marker.

This resulted in a total of 47 diffraction images of the sample in RT1, taken at pressures between 8 GPa and 86 GPa. During the 10 s exposure, the cell was rotated by ± 5° around the vertical axis (perpendicular to the X-ray beam), to suppress inhomogeneity in the diffraction rings as a result of some texture in the sample. The images of the pressure marker had a 3 s exposure (without rotation).

Cell LH1 was pre-compressed to 28 GPa to prevent amorphization of bridgmanite during laser-heating. The sample was then heated to ~1,800 K at each pressure step at spot 1 (fig. 5.1b). The measurement protocol (P2) for LH1 was as follows:

1. Increase pressure by ~2 GPa using the gas membrane;
2. Let pressure stabilize for a few minutes;
3. Take diffraction image at the position of the pressure marker;
4. Take diffraction image of the sample at spot 1 at room temperature;
5. Turn on lasers to heat the sample to 1,800 K and stabilize temperature;
6. Take diffraction image of the sample at high temperature;
7. Turn off lasers and take diffraction image of the quenched sample;
8. Take diffraction image at the position of the pressure marker.

The diffraction images of the sample between bouts of heating provide compression data of the annealed sample at room temperature. A total of 37 such images were taken at pressures between 28 GPa and 74 GPa. A total of 18 diffraction images were taken of the sample at high temperature. The exposure time for images of the sample was 5 s for the first three pressure steps and was then increased to 10 s, to improve intensity of the diffraction peaks. The exposure time for images of the pressure marker was 3 s. Temperatures during laser-heating were estimated radiometrically by fitting a Planck curve to the signal assuming the gray body approximation (using the program T-Rax developed by Clemens Prescher) and averaging the upstream and downstream measurements. Temperatures varied between 1715.5 K and 1859 K and uncertainties are estimated to be around

100 K. After the cell was compressed to 74 GPa, the sample was heated at ~2,200 K at a different spot (i.e. spot 2, fig. 5.1b) for ~15 minutes, to investigate how prolonged heating at high temperature affects the sample. Finally, diffraction images in a grid of 17x17 in 3 μm steps around the sample were measured at room temperature.

After decompression, the sample was recovered from the cell and any remaining KCl was removed by dissolving it in de-ionised water. The sample was mounted on a holder and analysed using a FIB/SEM system (Focussed Ion Beam/Scanning Electron Microscope), equipped with an EDS (Energy Dispersive X-ray Spectroscopy) detector at the David Cockayne Centre for Electron Microscopy, Department of Materials, University of Oxford, UK. The FIB was used to cut and polish cross-sections parallel to the compression axis across both laser-heating spots. These were imaged by SEM and EDS was used to measure elemental maps (fig. 5.3), which were processed using Aztec software.

To acquire zero-pressure volumes (V_0) of the two phases in the sintered sample, the sample was placed on top of a diamond culet and a diffraction pattern was measured in air at ambient pressure and temperature. The exposure time for this measurement was 1 s and the X-rays had a wavelength of 0.4845 Å, with a beam size of 3x8 μm^2 at FWHM.

5.2.3. Data processing and pressure estimation

The program Dioptas (Prescher & Prakapenka, 2015) was used to integrate the collected diffraction images. Lattice parameters of bridgmanite, ferropericlase and platinum (fitted with a face-centred cubic structure, space group $Fm\bar{3}m$) were extracted from the diffraction patterns by LeBail refinement with GSAS-II (Toby & Von Dreele, 2013). Representative fitted diffraction patterns of the sample for different experimental conditions are shown in figure 5.2. Parasitic peaks of rhenium (fitted with a hexagonal close-packed crystal structure, space group *P63/mmc*) could not be avoided in the experimental run in helium, because of the shrinkage of the sample chamber. Peaks of KCl (fitted with a body-centred cubic structure, space group $Pm\bar{3}m$) are present in the annealed and high-temperature data sets.

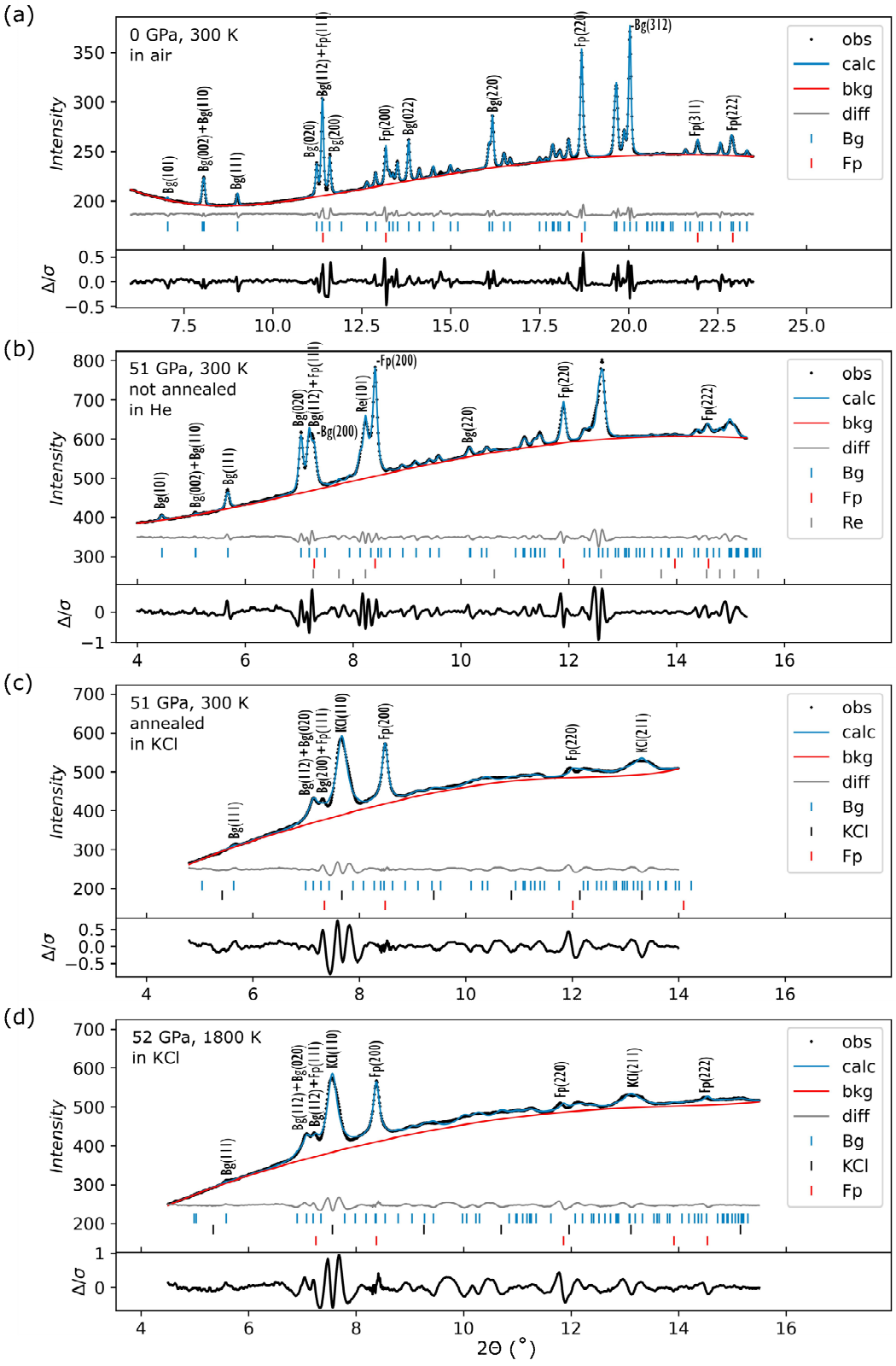

Figure 5.2 Representative X-ray diffraction patterns of the bridgmanite-ferropericlase polycrystal at different experimental conditions. Calculated (cal) spectra from LeBail fitting are also shown, with subtracted background (bkg) and difference curve (diff), as well as the differences divided by their uncertainty (Δ/σ). (a) Sample in air at ambient pressure and temperature. (b) Unannealed sample in helium, at 51 GPa and 300 K. (c) Annealed sample in KCl, at 51 GPa and 300 K. (d) Sample in KCl at 52 GPa and heated to 1,800 K.

The unit-cell volume of platinum was used to determine the pressure for all data sets, employing previously published third-order Birch-Murnaghan Equation of State (EoS) parameters (Fei et al., 2007a). A detailed description of how pressures for the sample measurements were calculated and uncertainties estimated is included in Appendix D.1. The time delay between measurements of the sample and the pressure standard introduces some uncertainty to the estimated pressure of the sample. However, by letting the pressure stabilize between pressure steps and measuring the pressure standard directly before/after the sample this uncertainty is minimized. This is supported by the small difference in the pressures measured before and after the sample (i.e. 0.3 GPa in RT1 and 0.5 GPa in LH1 on average). For the measurements in cell LH1, we also used the unit-cell volumes of KCl as a secondary pressure estimate, employing the Riedberg-Vinet EoS from Dewaele et al. (2012). The pressures determined from KCl measured with the sample and with platinum differ by up to 13 GPa, which is likely due to the comparatively large non-hydrostaticity of KCl as a PTM (Takemura, 2021; Uts et al., 2013). We chose to use the pressures determined from platinum because they are intermediate between those from KCl (fig. D.1) and allow for direct comparison to the measurements in RT1, but the pressures from KCl were used to estimate uncertainties.

Estimating the pressure of the sample during the measurements at high-temperature is more involved, because the pressure marker was measured at room temperature, while the sample was measured at ~1,800 K. During isochoric heating (i.e. the volume remains constant), the thermal pressure corresponds to the thermodynamic thermal pressure (P_{th}): $\left(\frac{\partial P}{\partial T}\right)_V = \alpha_V K_T$, where α_V is the thermal expansion and K_T is the isothermal bulk modulus. Contrarily, during isobaric heating, the sample container expands according to the thermal expansion and the thermal pressure is zero. Estimating the thermal pressure in laser-heated DACs is not straightforward, but P_{th} appears to be a reasonable first-order estimate for the thermal pressure in the volumetrically constrained pressure chamber of a DAC without the use of a PTM (Yen et al., 2020). However, the use of KCl as PTM in our experiments likely resulted in some volume expansion of the sample during heating and P_{th} is expected to overestimate the real thermal pressure. P_{th} depends on α_V and K_T, which are not the

same for the sample materials and platinum. Nonetheless, at relevant conditions the product $\alpha_V K_T$ that determines P_{th} is quite similar, i.e. at 2000 K and 40 GPa, $\alpha_V K_T$ equals approximately 7.4E-3 $GPaK^{-1}$ for bridgmanite, 7.9E-3 $GPaK^{-1}$ for ferropericlase and 7.5E-3 $GPaK^{-1}$ for platinum (Sun et al., 2008; Tange et al., 2012; Wentzcovitch et al., 2009). Andrault et al. (1998) reported a positive correlation between the ratio of experimental thermal pressure over isochoric thermal pressure and the value of $\alpha_V K_T$ for different samples in a pressure medium. Based on this relationship, we estimated the pressure at high temperature during our experiments by adding 80% of the thermal pressure of platinum at 1,800 K, based on the thermal EoS of Fei et al. (2007a), to the measured pressure at 300 K. While the uncertainty in the pressure estimate of the high temperature data is relatively large as a result of not directly measuring the pressure at high temperature, the volume of bridgmanite and ferropericlase was measured simultaneously at the same *P*, *T*-conditions. Therefore, we can directly compare their relative compression behaviours, since any inaccuracy in the pressure estimate will shift their respective compression curves by the exact same amount.

5.3. Results

5.3.1. Sample characterization and effects of laser-heating

SEM-EDS analysis of a cross-section of the laser-heated sample allows us to characterize its texture, grain size and composition. Ferropericlase and bridgmanite grains can be distinguished by brightness in the back-scattered electron images of the cross-section of the sample, with bridgmanite appearing darker (fig. 5.3, top row). The distribution of both phases is fairly homogeneous in unheated areas, with grain sizes varying slightly between approximately 0.1-0.5 μm. The two phases are also clearly visible in Mg and Si element maps, with a strong Si signal indicating bridgmanite and a strong Mg signal corresponding to ferropericlase grains (fig. 5.3). The expected volume ratio of bridgmanite to ferropericlase based on the olivine starting material used to synthesize the two-phase sample is approximately 7:3. This is in good agreement with visual estimates from the back-scattered electron images (fig. 5.3), as well as the estimates from fitting of the diffraction pattern collected at 0 GPa, which produced a volume ratio of 73:27.

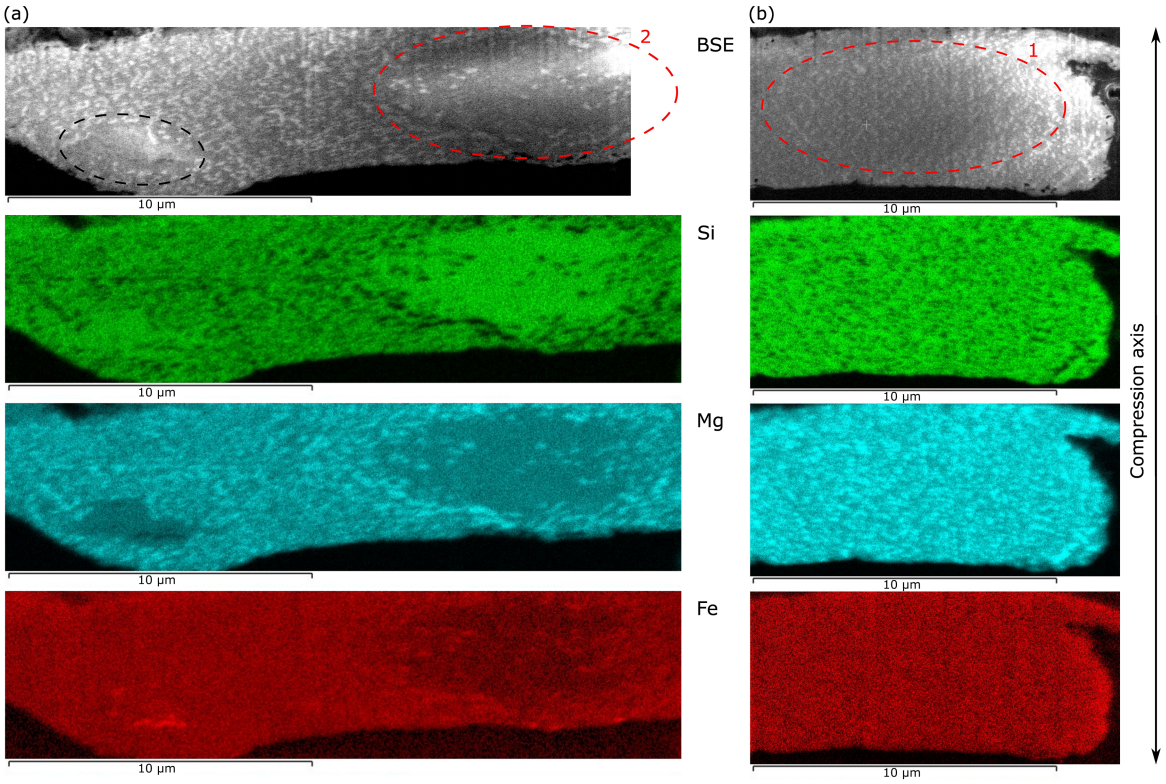

Figure 5.3 Backscattered-electron images (top-row) and X-ray maps for Si, Mg and Fe (second, third and fourth row, respectively) of cross-sections of the laser-heated areas in the polycrystalline sample of bridgmanite and ferropericlase. Bridgmanite appears darker in the electron images, while ferropericlase appears brighter. The compression axis during the experiment is indicated by the black arrow on the right. (a) Cross-section of spot 2, which was heated at 2,200 K (outlined by the red oval). The black oval indicates an area enriched in aluminium. (b) Cross-section of spot 1, which was heated at 1,800 K (outlined by the red oval).

While the distribution of iron appears mostly homogeneous in unheated areas of the sample, we observe one region that is enriched in iron, with ~1.5 at.% Al. This suggests the presence of some impurities in the starting material, implying that the bulk composition of the sample may deviate locally from $(Mg_{0.91}Fe_{0.09})_2SiO_4$.

In the laser-heating spot where the sample was heated at 2,200 K for an extended period (spot 2), we observe striking changes in the mineralogy, texture and element distribution of the sample (fig.5.3a). The sample has recrystallized, with large (~1.5 µm) bridgmanite grains that show changes in microstructure (fig. D.2) forming in the centre and ferropericlase concentrated in a rim surrounding the hotspot. The recrystallized bridgmanite is depleted in iron, while the ferropericlase in the rim is enriched in iron (fig. 5.3a, bottom row). Migration of iron away from the hot centre is in good agreement with the observations of Sinmyo and Hirose (2010). None of the effects of

laser-heating observed in spot 2 are visible in spot 1, where the sample was heated at 1,800 K at each pressure step: grain size and volume fractions of ferropericlase and bridgmanite remain unchanged and no variations in iron concentration are seen (fig. 5.3b). While the XRD images of location 2 after heating show clear signs of recrystallisation, this is not observed in the images of location 1 (fig. D.3). From this we conclude that the laser-heating in spot 1, due to the lower temperature, did not lead to significant changes in iron partitioning between ferropericlase and bridgmanite and the collected pressure-volume data should therefore represent the compression curves for constant compositions of both minerals.

5.3.2. Iron partitioning between bridgmanite and ferropericlase

The grain size of the sample is too small to measure the composition of individual crystals. However, some constraints on iron distribution can be obtained from the zero-pressure volumes of the two phases, measured by XRD (fig. 5.2a). For $(Mg_{1-x}Fe_x)O$ ferropericlase, we found V_0 = 75.269(3) Å^3, suggesting $x_{Fe} \approx 0.085$ (Jacobsen et al., 2002; Trautner et al., 2024). While iron in ferropericlase is expected to be predominantly ferrous for low iron contents (McCammon et al., 1998), iron in bridgmanite can exist as both Fe^{2+} and Fe^{3+} and is able to occupy both the dodecahedral and octahedral sites (Catalli et al., 2010). Fei et al. (2020) reported that the presence of (Mg,Fe)O increases $Fe^{3+}/\Sigma Fe$ in bridgmanite through oxygen vacancy substitution, suggesting that bridgmanite in our sample may be Fe^{3+}-rich. Fe^{3+} expands the unit-cell volume of bridgmanite more than Fe^{2+} relative to the Mg-endmember (Catalli et al., 2010). For bridgmanite in our sample we found V_0 = 164.446(5) Å^3. For a low $Fe^{3+}/\Sigma Fe$ this would suggest an iron content of > 0.35, while for a high $Fe^{3+}/\Sigma Fe$ this indicates an iron content of ~0.1 (Tschauner et al., 2014), which is more in line with the bulk composition of the sample.

The EDS spectra provide additional constraints on the iron content and distribution of the sample. We find an average iron number (i.e. Fe/[Fe+Mg]) of $\#Fe$ = 0.063 in location 1, which is lower than expected from the theoretical bulk composition ($\#Fe$ = 0.09). However, measurements of composition with EDS are imprecise and the standardless analysis method employed here has a relative deviation from the expected value of ± 25% (Goldstein et al., 2018). In addition, local iron

content may vary from the bulk composition of the starting material as a result of impurities. While it is not possible to achieve sufficiently high counts to determine the composition of individual grains due to their submicron size, we have computed spectra of comparatively Si-rich and Si-poor regions, which correspond to bridgmanite-rich and ferropericlase-rich material, respectively (fig. D.4). We can then use the Si content as a proxy for the relative proportions of the two phases in the measured region. When plotting the measured *#Fe* as a function of Si at.% normalized with respect to the total cation content (i.e. Si/[Fe+Mg+Si]), this should fall on a mixing line between the x_{Fe} of ferropericlase (at 0 Si) and x_{Fe} of bridgmanite (at 0.5 Si) (fig. 5.4). While scatter is large due to the small surface area used to compute the spectra, we find that #Fe in the bridgmanite-rich areas is higher than in the ferropericlase-rich areas. This suggests a partition coefficient $K_D < 1$, where $K_D = [Fe/Mg]_{Fp}/[Fe/Mg]_{Bg}$. This is consistent with the iron contents of the phases estimated from the zero-pressure volumes ($K_D \approx 0.8$). Iron partitioning experiments for a similar bulk composition at 1873 °C and 26 GPa (i.e. comparable to the synthesis conditions of the sample studied here) found $K_D \approx 4$ (Martinez et al., 1997). This deviates significantly from our estimates, but we cannot easily explain the difference.

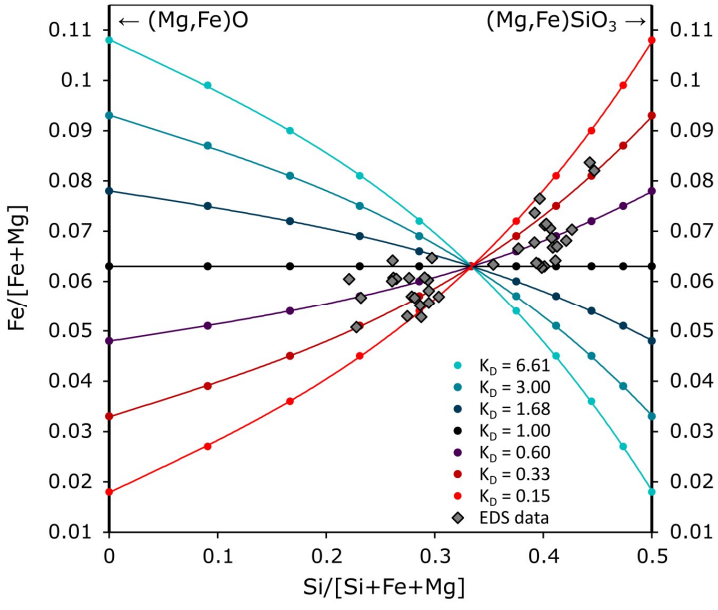

Figure 5.4 Fe/[Fe+Mg] as a function of Si/[Si+Fe+Mg] (in atomic %) of relatively bridgmanite- and ferropericlase-rich areas in the two-phase sample, measured by EDS (grey diamonds). Si/[Si+Fe+Mg] is a proxy for bridgmanite abundance: 100% (Mg,Fe)O would fall on 0 and 100% (Mg,Fe)SiO_3 at 0.5. Theoretical mixing lines for different Fe-Mg partition coefficients (K_D) between ferropericlase and bridgmanite if the bulk Fe/[Fe+Mg] = 0.063 (as measured by EDS for the two-phase sample) are shown with different colours.

5.3.3. Compression curves of ferropericlase and bridgmanite in a two-phase aggregate

Figure 5.5a shows the pressure-volume measurements at 300 K for ferropericlase in the sintered two-phase aggregate, with and without laser-annealing. Also shown are previously published compression data for polycrystalline $(Mg_{0.9}Fe_{0.1})O$ (Marquardt et al., 2009a) and $(Mg_{0.813}Fe_{0.17})O$ (Lin et al., 2005), as well as the $P(V)$-curve of $(Mg_{0.81}Fe_{0.19})O$ predicted by *ab initio* computations (Trautner et al., 2023). We observe a striking difference in the compression behaviour of single-phase ferropericlase and ferropericlase in the two-phase sample that was not annealed: the compression curve of the latter is much shallower and at 80 GPa the volume is ~3.5% larger than expected from single-phase measurements. In contrast, the volumes of ferropericlase in the annealed two-phase sample are in excellent agreement with the steeper compression curves of the single-phase literature data.

The $P(V)$-data for bridgmanite in the annealed and unannealed two-phase aggregate is shown in figure 5.5b, together with literature results for single-crystal $(Mg_{0.96}Fe_{0.04})SiO_3$ (Ballaran et al., 2012) and single-phase polycrystalline $(Mg_{1-x}Fe_x)(Si_{1-x}Fe_x)O_3$ with $x_{Fe} = 0.1$ (Catalli et al., 2010). The lattice parameters as a function of pressure are shown in figure D.5. The volumes for bridgmanite in the unannealed sample are in good agreement with literature data, showing no signs of the anomalous compression behaviour observed in ferropericlase. A slight offset in the volume curves is likely due to differences in $Fe^{3+}/\Sigma Fe$ and total iron content. The trend of the compression curve for bridgmanite in the annealed sample is also consistent with the literature data, but it is shifted to higher volumes, compared to the unannealed sample. We can partially explain this by relaxation of stresses in the sample during annealing, since the volume of bridgmanite increased after the first episode of heating (fig. 5.5b). In addition, uncertainties in the volume of bridgmanite for the measurements in cell LH1 are large, because peak overlap with KCl and ferropericlase in the diffraction patterns resulted in only a single, low-intensity peak of bridgmanite that could be fit in isolation (fig. 5.2c,d). The three unique lattice parameters of orthorhombic bridgmanite could therefore not be constrained very well in the laser-heated sample.

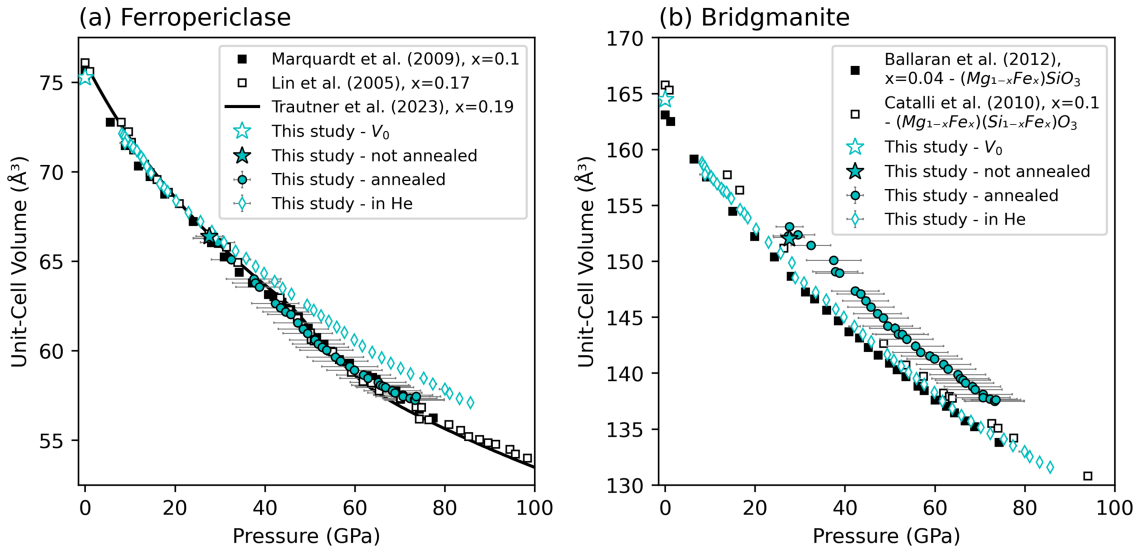

Figure 5.5 Compression curves for ferropericlase (a) and bridgmanite (b) at 300 K. Volume-pressure data collected during compression of the two-phase sample in KCl or in helium as pressure medium and with or without laser-annealing are shown with filled circles and open diamonds, respectively. The open star indicates the volumes at ambient conditions and the filled star indicates volumes measured in KCl before annealing. Also shown are literature data for single-phase powder of ferropericlase (Marquardt et al., 2009a) and single crystal bridgmanite (Ballaran et al., 2012) (filled squares), single-phase polycrystals of ferropericlase (Lin et al., 2005) and bridgmanite (Catalli et al., 2010) (open squares), and theoretical computations for ferropericlase (Trautner et al., 2023) (black line); all with similar compositions as those estimated for the two-phase sample.

The compression curves for ferropericlase and bridgmanite in the two-phase aggregate at 1,800 K are shown in figure 5.6. Our results for ferropericlase agree well with published experimental data for single-phase polycrystalline $(Mg_{0.81}Fe_{0.19})O$ at similarly high temperatures (Komabayashi et al., 2010), as well as theoretical computations (Trautner et al., 2023). The volumes of bridgmanite in the two-phase sample at 1,800 K are higher than previous high-temperature results for single-phase polycrystalline $(Mg_{0.87}Fe_{0.13})SiO_3$ (Wolf et al., 2015), but the volume difference between results at 300 K and ~1,800 K is approximately the same for both data sets. The similar magnitudes of volume expansion from 300 K to 1,800 K observed in our experiments and in previous studies indicates that our approach to estimate the pressure for the high-temperature data is reasonable (see section 5.2.3).

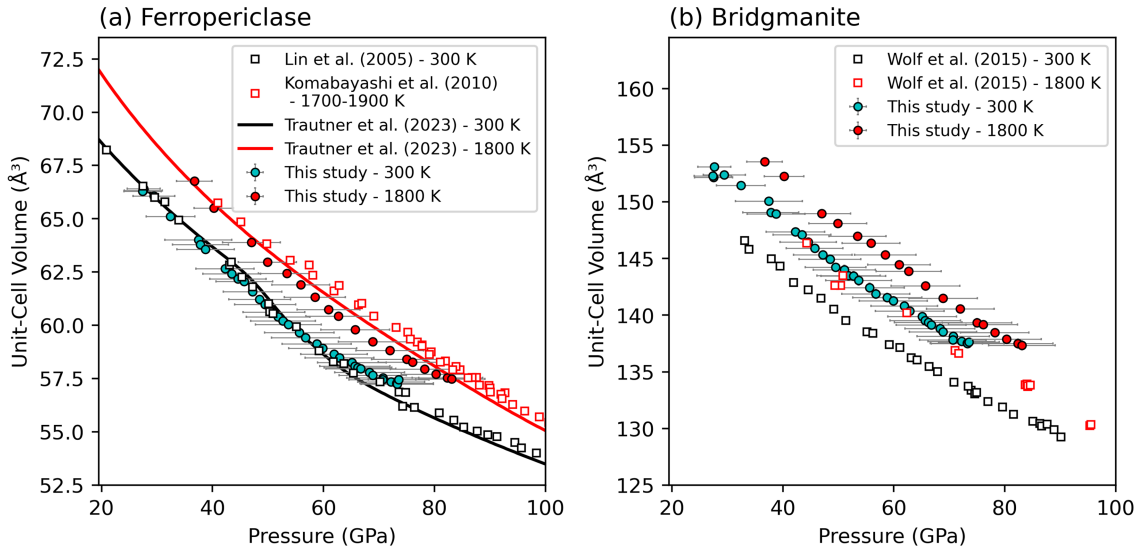

Figure 5.6 Compression curves for ferropericlase (a) and bridgmanite (b) at 300 K and 1,800 K. Volume-pressure data collected during compression of the two-phase sample in KCl at 300 K and 1,800 K are shown with green and red filled circles, respectively. Also shown in (a) are literature data for single-phase, polycrystalline ferropericlase at 300 K (Lin et al., 2005) and 1,700-1,900 K (Komabayashi et al., 2010) (black and red open squares, respectively), as well as results at 300 K and 1,800 K (black and red lines, respectively) from theoretical computations (Trautner et al., 2023). In (b), compression data for single-phase, polycrystalline bridgmanite at 300 K and 1,800 ± 65 K from Wolf et al. (2015) are shown as black and red open squares, respectively.

5.4. Discussion

5.4.1. Stress-strain partitioning between ferropericlase and bridgmanite

Differences in stress and strain partitioning between ferropericlase and bridgmanite in our experiments may allow us to explain the contrasting compression behaviour of ferropericlase in the unannealed and annealed two-phase samples (fig. 5.5). But first we must consider the types of strain and stress occurring in our experiments. DACs are uniaxial compression devices, in which the diamonds impose pressure (or confining stress) and deviatoric stress on a sample. The use of a pressure medium can reduce the deviatoric stress in the sample chamber to quasi-hydrostatic conditions, resulting in near hydrostatic strain. Whether stress is accommodated elastically or plastically depends on whether the deviatoric stress on a material exceeds its strength (i.e., yield stress). Helium maintains its quasi-hydrostatic properties to very high pressures and external deviatoric stress in cell RT1 is therefore expected to be very low. However, even during uniform compression, differences in compressibility of the constituent phases of a multi-phase material will

result in stresses developing at the grain boundaries. Therefore, the unannealed sample in RT1 may still experience significant internal deviatoric stresses, despite being surrounded by quasi-hydrostatic helium. External deviatoric stress is much larger in a less hydrostatic pressure medium like KCl, as was used in cell LH1. However, laser-annealing homogenizes stresses in the sample: heating of the sample results in a reduction of the yield stress, leading to plastic deformation and reduction of internal deviatoric stresses. Such plastic deformation is not visible in XRD measurements of an axial DAC compression experiment, because XRD only records the stress-induced deformation of the crystal lattice (i.e. elastic deformation).

The bulk elastic behaviour of the two-phase sample is expected to lie between the Voigt and Reuss bounds, i.e. homogeneous strain or homogeneous stress, respectively (Karato, 2008; Reuss, 1929; Voigt, 1928). Since bridgmanite is significantly stronger than ferropericlase (Girard et al., 2016), the bulk strength of the sample is likely determined by how interconnected the respective mineral grains are. The volume proportions of bridgmanite and ferropericlase in the two-phase sample is approximately 7:3 and back-scattered electron images of the sample (fig. 5.3) show that ferropericlase grains are not interconnected (at least not in the two-dimensional cross-section). This suggests that bridgmanite might behave like a load-bearing framework (Handy, 1994), supporting most of the external stress field and controlling the strain rate. This scenario can explain the anomalous compression behaviour of ferropericlase in the unannealed sample (fig. 5.5). Because bridgmanite is less compressible than ferropericlase (e.g. Ballaran et al., 2012; Marquardt et al., 2009a), the pressure transmitted to ferropericlase by elastic deformation of bridgmanite is lower than the confining pressure, resulting in a less steep compression curve. Ferropericlase in the experiment with laser-annealing, on the other hand, exhibits the same compression behaviour as in single-phase materials, indicating that the pressure on ferropericlase is equal to the confining pressure. This suggests that stresses in the sample are homogenized at high temperature, likely through plastic deformation.

We can further investigate the stress-strain partitioning in the sample by looking at normalized volume strain ($\varepsilon = [V\text{-}V_{ref}]/V_{ref}$) as a function of pressure (fig. 5.7). Since the two-phase sample was

synthesized at 27 GPa and decompression to room pressure is likely to have changed the stress state, we use the volumes at 27 GPa as V_{ref}. We compare our results for the two-phase aggregate with single-phase data from literature (Ballaran et al., 2012; Catalli et al., 2010; Lin et al., 2005; Marquardt et al., 2009a). We find that the strain in single-phase ferropericlase is larger than for single-phase bridgmanite, as expected from the higher compressibility of ferropericlase. For the annealed sample, the strain of both phases is in excellent agreement with the single-phase data, confirming that the elastic behaviour of the sample in this experiment is best described by the iso-stress model. For the unannealed sample, the strain of bridgmanite is also consistent with the single-phase data. However, the strain of ferropericlase is lower than that of single-phase ferropericlase, but higher than the strain of bridgmanite. This suggests that stress-strain partitioning in the sample is intermediate between the Voigt and Reuss bounds. The pressure difference between ferropericlase in the annealed and unannealed sample for the same strain may be indicative for the maximum stress that can be supported by bridgmanite before plastic deformation occurs and any additional stress is transmitted to ferropericlase.

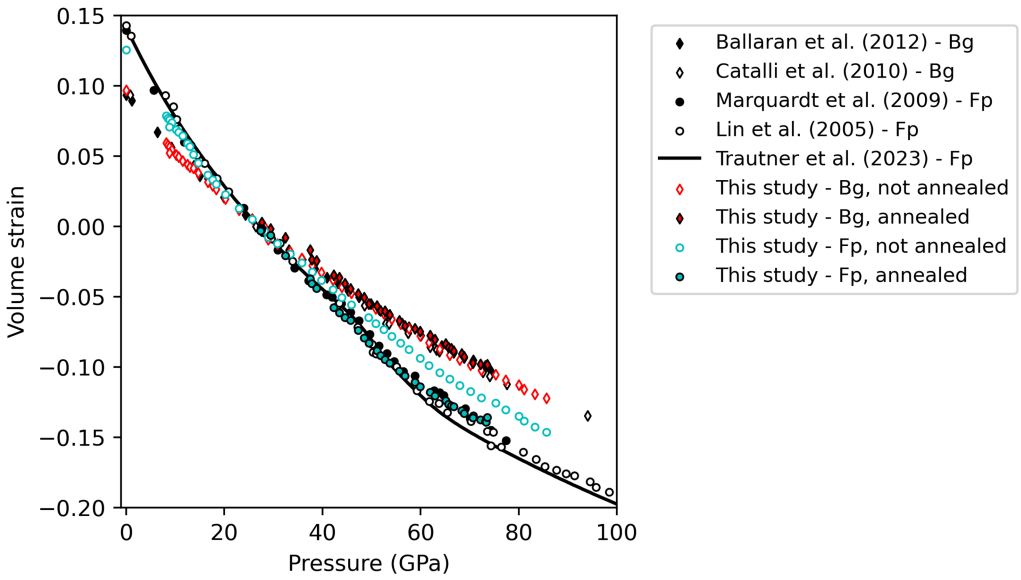

Figure 5.7 Volume strain as a function of pressure for ferropericlase (circles) and bridgmanite (diamonds) at 300 K, relative to the volume at 27 GPa. Strain during compression of the two-phase sample with or without laser-annealing is shown with filled and open coloured symbols, respectively. Also shown are literature data for single-phase powder of ferropericlase (Marquardt et al., 2009a) and single-crystal bridgmanite (Ballaran et al., 2012) (filled black symbols), single-phase polycrystals of ferropericlase (Lin et al., 2005) and bridgmanite (Catalli et al., 2010) (open black symbols), and theoretical computations for ferropericlase (Trautner et al., 2023) (black line).

Between 27 GPa and 75 GPa, the difference between the pressure-strain curves of the two ferropericlase samples increases from ~0 GPa to ~10 GPa (fig. 5.7). This is approximately half of the maximum differential stresses observed in bridgmanite at room temperature, which are indicative for flow strength (Miyagi, 2021).

From our findings we conclude that quasi-hydrostatic deformation of a bridgmanite-ferropericlase aggregate at room temperature is intermediate between iso-stress and iso-strain scenarios, with the degree of stress-strain partitioning governed by the strength of bridgmanite if it forms a load-bearing framework. At high temperature, the system moves towards an iso-stress regime and the new stress state is preserved after quenching to room temperature. This suggests that the Reuss bound may be more appropriate to describe the bulk elastic properties of lower mantle rocks, as minimum temperatures in the lower mantle are expected to be > 1,800 K (Davies et al., 2012). It is important to note that the elastic response of rocks may depend on the compression rate and stress-strain partitioning could therefore be different at the frequency of seismic waves (Buchen, 2021).

5.4.2. Effects of stress-strain partitioning on the iron spin crossover in ferropericlase

Ferrous iron in ferropericlase undergoes a pressure-induced spin crossover, involving an electronic reconfiguration from high-spin to low-spin state (Badro et al., 2003). This is associated with a decrease in ionic radius of iron, leading to an enhanced volume reduction across the spin crossover pressure range (e.g. Lin et al., 2013). Since the spin crossover is pressure-induced, and therefore sensitive to the hydrostatic or confining stress, it may be affected by the stress-strain partitioning in the two-phase aggregate of bridgmanite and ferropericlase. While the volume reduction caused by the spin crossover is discernible in the *P(V)*-curve of ferropericlase (fig. 5.5a), it occurs gradually, making it difficult to pinpoint the exact onset pressure. The spin crossover is more easily identified in the relationship between normalized stress *F* and Eulerian strain *f*, where $f = 0.5\ (\frac{V_0^{\frac{2}{3}}}{V} - 1)$ and $F = \frac{P}{3f(1+2f)^{5/2}}$ (Angel, 2000; Stacey et al., 1981). We calculate the normalized stress of ferropericlase in our experiments, using the measured V_0 for ferropericlase in the unannealed

sample. The V_0 reported by Marquardt et al. (2009a) is used for ferropericlase in the annealed sample, because it is in better agreement with the extrapolated pressure-strain curve (fig. 5.7). When normalized stress is plotted as a function of pressure (fig. 5.8), the pressure range of the spin crossover is marked by a drop in normalized stress (e.g. Glazyrin et al., 2016; Solomatova et al., 2016). We find that the spin crossover in ferropericlase in the annealed sample occurs between ~40-58 GPa, while it occurs between ~50-72 GPa in the unannealed sample. The shift of the onset to higher pressure in the unannealed sample is consistent with ferropericlase experiencing a lower confining stress than expected from the pressure in the sample chamber, because it is shielded by less compressible bridgmanite. The intercept on the F axis of the F-P plot corresponds to the value of the bulk modulus at ambient conditions (K_0). Single-phase ferropericlase has a K_0 around 158 GPa (Marquardt et al., 2009a), while single-phase bridgmanite has a has a K_0 around 250 GPa (Ballaran et al., 2012). Despite the large scatter in the F-P plot at low pressures that is typical for such plots (Angel, 2000), it is evident that K_0 of ferropericlase for the unannealed sample (~180 GPa, fig. 5.8) is intermediate between the values of single-phase ferropericlase and bridgmanite.

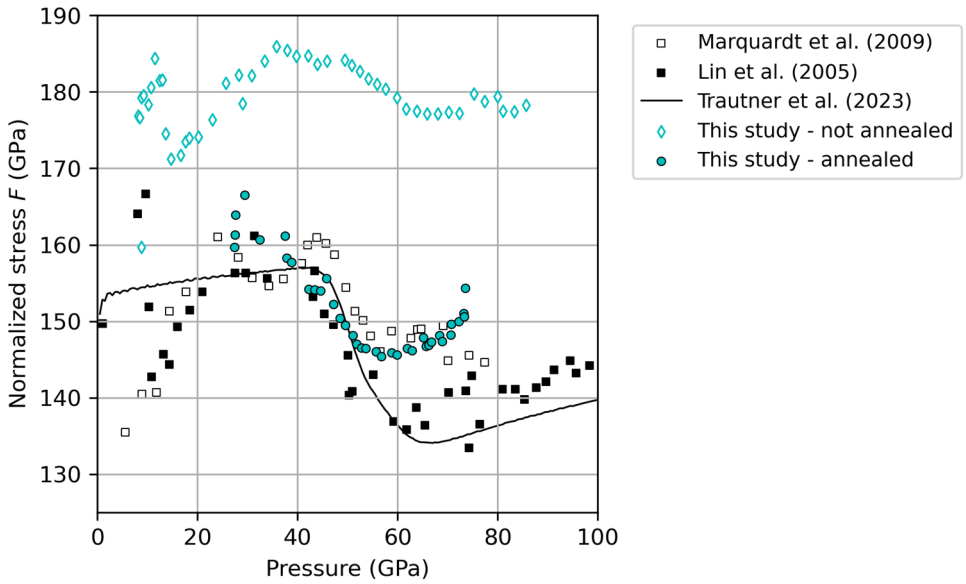

Figure 5.8 Normalized stress F as a function of pressure for ferropericlase. Data from ferropericlase in the two-phase sample with and without laser-annealing are shown with coloured circles and open diamonds, respectively. Also shown are literature data for single-phase ferropericlase from Marquardt et al. (2009a) (filled squares) and Lin et al. (2005) (open squares), as well as theoretical computations (Trautner et al., 2023) (black line). A drop in the normalized stress occurs across the pressure range of the iron spin crossover.

This is further evidence suggesting that the elastic behaviour of ferropericlase in the two-phase aggregate is controlled by the compressibility of bridgmanite at ambient temperature.

5.5. Conclusions

We have investigated the compression behaviour of a two-phase aggregate of bridgmanite and ferropericlase, approximating the mineralogy of the lower mantle, at ambient and high temperatures. We compared our results to single-phase experimental results and investigated the effects of laser-annealing on stress-strain partitioning between the two phases. We found that bridgmanite forms a load-bearing framework during quasi-hydrostatic compression at room temperature, with the bulk elastic deformation of the sample intermediate between iso-strain and iso-stress bounds: the compressibility and strength of bridgmanite determine how much of the external confining pressure is transmitted to ferropericlase. As a result, the iron spin crossover in ferropericlase occurs at higher pressures than in single-phase experiments. At high temperatures, stress is homogenized and the elastic behaviour of bridgmanite and ferropericlase in the two-phase aggregate is consistent with observations from single-phase experiments. Our findings show that temperature has a strong effect on stress-strain partitioning in multi-phase materials. Therefore, it is imperative to study the deformation of polymineralic mantle assemblages at relevant conditions, in order to get accurate estimates of the bulk elastic and rheological properties of the mantle for geodynamic modelling and seismic wave inversions.

Chapter 6. Synthesis

In the previous four chapters, I have sought to enhance our understanding of the effects of the iron spin crossover in ferropericlase on lower mantle seismology by taking an interdisciplinary approach. High-pressure experiments, theoretical computations, synthetic seismic tomography models, seismic wave propagation simulations and machine-learning techniques were used to constrain the elastic behaviour of ferropericlase in *P-T-X* space and characterize the signal of the spin crossover in seismic observations. In this chapter, I draw over-arching conclusions from the findings of each data chapter and reflect on the wider implications for the study of the deep Earth. I also discuss remaining questions that should be addressed by future studies and outline how such studies may build upon the findings of this thesis. This chapter is structured around the aims formulated in Chapter 1 (see section 1.5), with concluding remarks presented in section 6.6.

6.1. Temperature-dependence of the iron spin crossover in ferropericlase

The findings presented in Chapter 2 demonstrate that the spin crossover is highly sensitive to temperature, shifting to higher pressure and broadening with increasing temperature. As a result, lower-mantle ferropericlase is expected to be primarily in mixed-spin state between ~1,250 km depth and the core-mantle boundary. Substantial lateral variations in low-spin fraction exist between hot and cold regions, e.g., rising plumes and down-going slabs, as illustrated in figure 6.1.

The temperature-dependence of spin state is reflected in the spin crossover-induced softening of P-wave and bulk sound velocities: with increasing temperature, the softening shifts to higher pressures, broadens and its maximum magnitude decreases. This has major implications for seismic velocities in the lower mantle, because it results in a reduced-temperature sensitivity of P-wave and bulk sound velocities in regions with mixed-spin ferropericlase. Consequentially, thermal structures in the lower half of the mantle may become less pronounced or even invisible in P-wave tomography models compared to S-wave tomography models. This could help to explain discrepancies in the imaging of plumes (Montelli et al., 2006), as well as slabs (Shephard et al., 2017; Shephard et al., 2021) in the mid-lower mantle using P-waves versus S-waves.

The temperature-dependence of the spin crossover is also expected to affect mantle dynamics, as a result of the increase in density that occurs across the transition from HS to LS state. Because of the positive Clapeyron slope of the spin crossover, this increase occurs at shallower depths in colder regions of the mantle. Similar to the olivine polymorphic transformations in the transition zone (i.e., olivine to wadsleyite to ringwoodite), the spin crossover should thus help to drive mantle convection (Faccenda & Dal Zilio, 2017).

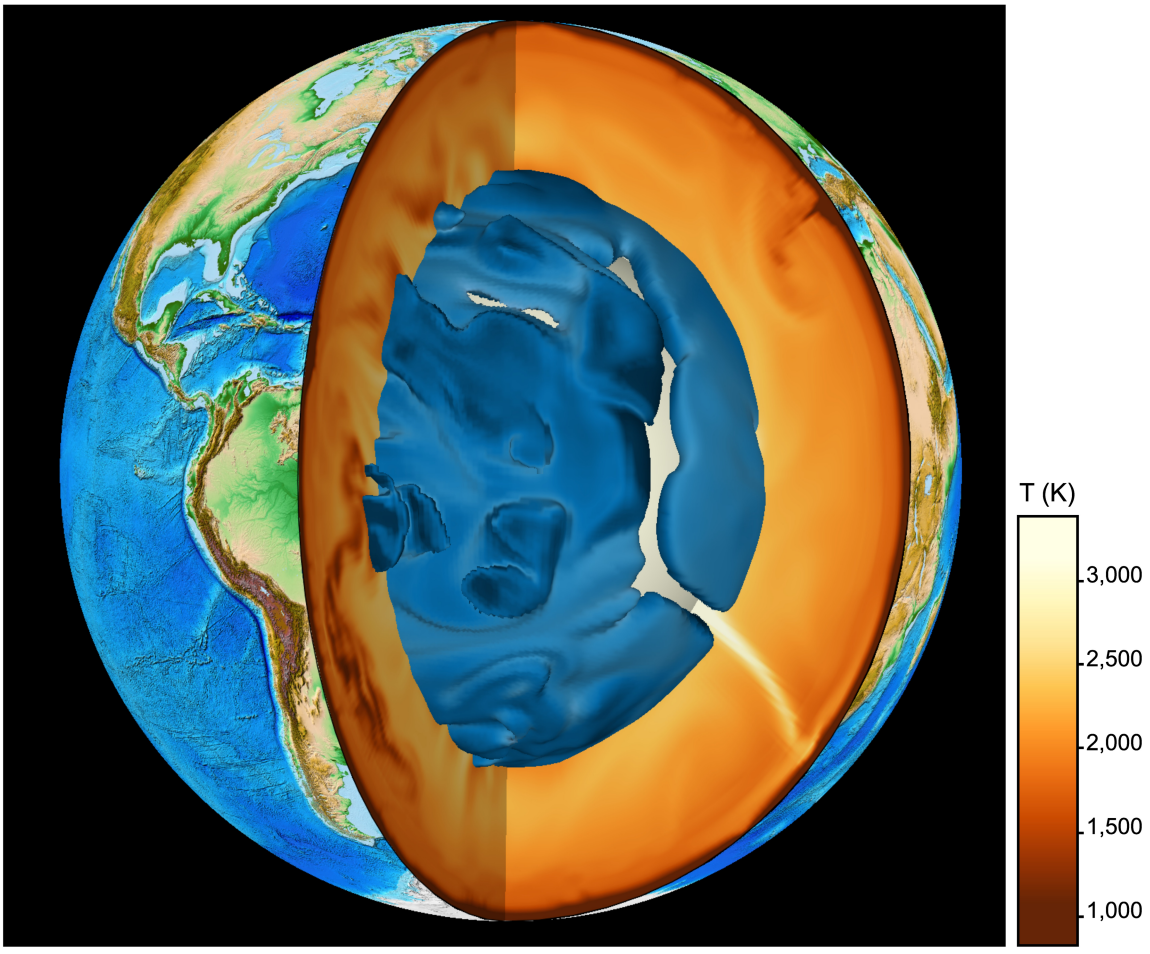

Figure 6.1 Three-dimensional model of the Earth, with the blue surface showing the contour of a low-spin fraction of n = 0.4 in ferropericlase, corresponding to where the spin crossover-induced effects on seismic velocities are largest. The cross-sections show temperature variations in the mantle (Davies et al., 2012), illustrating the temperature-sensitivity of the spin crossover. The figure is based on the results from Chapter 2 and made with the GPlates software (Müller et al., 2018), courtesy of Paula Koelemeijer.

6.2. Effect of iron content on the elastic behaviour of ferropericlase across the iron spin crossover

The spin crossover does not only depend on temperature, but is also strongly affected by the iron content of ferropericlase (Chapter 4). At ambient temperature, the bulk modulus softening broadens and shifts to higher pressures with increasing iron content (fig. 6.2). I also found that the maximum magnitude of the softening is largest for moderately iron-enriched compositions (i.e., $(Mg_{1-x}Fe_x)O$ with $x \approx 0.4$). Iron partitioning between ferropericlase and bridgmanite varies with pressure, temperature, oxygen fugacity, bulk iron content and spin state (Huang et al., 2021; Muir & Brodholt, 2016) and it is thus likely that a range of ferropericlase compositions exist in the Earth. The properties of iron-enriched ferropericlase are of particular interest for regions in the lowermost mantle. Firstly, because the iron content of ferropericlase is expected to increase with depth in an isochemical lower mantle (Muir & Brodholt, 2016; Xu et al., 2017). In addition, strongly iron-enriched material containing iron-rich ferropericlase might exist close to the core-mantle boundary (Liu et al., 2016; Otsuka & Karato, 2012), possibly producing the anomalous seismic characteristics of ultra-low velocity zones (Finkelstein et al., 2018; Wicks et al., 2017; Yu & Garnero, 2018).

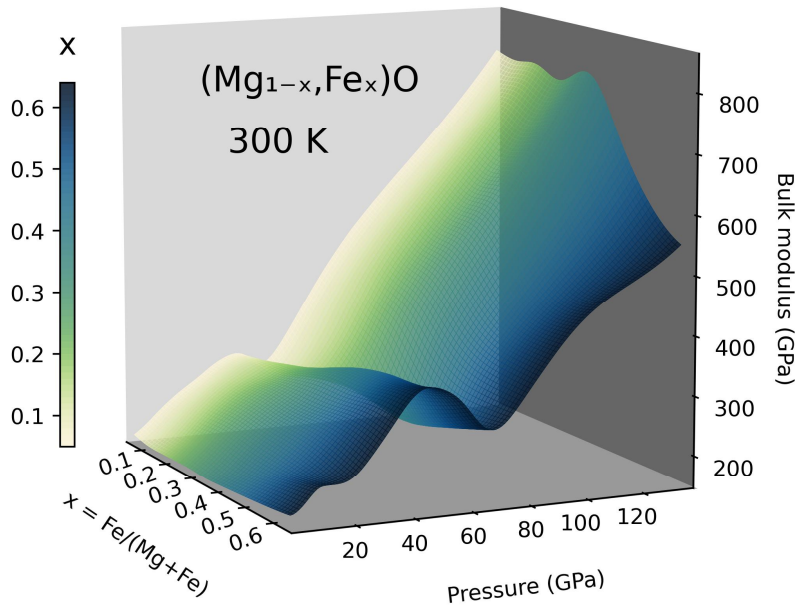

Figure 6.2 Changes in the bulk modulus of ferropericlase as a function of pressure and iron content at 300 K, inferred from experimental data by trained Mixture Density Networks (see Chapter 4). The softening caused by the spin crossover has a maximum magnitude for $x \approx 0.4$.

The shift of the spin crossover to higher pressures with increasing temperature and iron content and the amplification of the bulk modulus softening for moderately iron-enriched compositions suggests that it might strongly affect the properties of iron-rich ferropericlase in the lowermost mantle, resulting in reduced compressional and bulk wave velocities. To fully understand these effects, an essential next step is to constrain the elastic properties of iron-rich ferropericlase across the spin crossover at mantle temperatures. However, experimentally determining the elastic properties of materials at the extreme pressures and temperatures of the lowermost mantle is exceedingly difficult (Marquardt & Thomson, 2020). Accessing the full range of mantle pressures and temperatures is much more straightforward with computational techniques, but these require approximations and empirical constraints. Calculations of the thermoelastic properties of iron-rich ferropericlase across the spin crossover are expected to be particularly challenging because of the strongly correlated nature of iron, requiring careful consideration of, amongst others, choice of exchange correlation functional, magnetic state and distribution of iron atoms in the crystal lattice (e.g. Méndez et al., 2022; Speziale et al., 2005; Umemoto et al., 2008). Therefore, a combined approach as presented in Chapter 2, where theoretical computations are calibrated with experimental benchmarks, should produce the most accurate constraints for seismic studies.

6.3. Effects of stress-strain partitioning in polymineralic mantle rocks on the iron spin crossover

Stress-strain partitioning between individual minerals in polyphase mantle rocks determines the bulk rheologic and elastic properties of lower mantle materials (Karato, 2008) and is therefore an important factor in geodynamics and seismology. In Chapter 5, I demonstrated that stress-strain partitioning in an aggregate of bridgmanite and ferropericlase is strongly dependent on temperature. At ambient temperature, bridgmanite forms a load-bearing framework, determining the strain rate of ferropericlase, while at mantle-like temperatures, stresses are homogenized and the elastic behaviour of both minerals is consistent with single-phase results. Waves passing through the lower mantle impose small stresses and strains on the individual grains that compose the rock. This is thought to result primarily in reversible elastic deformation, governed by the bulk

elastic properties of the rock (Buchen, 2021). My findings in Chapter 5 are an indication that the bulk elastic properties of lower mantle rocks might be best described by the Reuss (i.e., iso-stress) bound (Reuss, 1929). However, further work is required to confirm this, since stress-strain partitioning might change for the frequency of seismic waves (Buchen, 2021).

The effect of compression rate on the elastic properties of materials can be investigated with pressure cycling experiments in dynamic diamond anvil cells, such as those reported in Chapter 2 (Jenei et al., 2019; Marquardt et al., 2018; Méndez et al., 2020). When combined with time-resolved X-ray diffraction in a radial diffraction geometry, it is possible to quantify the evolution of stress and strain in polycrystalline materials during pressure cycling (Buchen et al., 2023; Huston et al., 2024). To get accurate constraints on stress-strain partitioning in the lower mantle, it is important that such experiments are conducted at high temperatures or at the very least, that differential stresses are reduced through temperature-annealing. I found that the spin crossover in ferropericlase is sensitive to confining stress and occurs at higher pressure when bridgmanite forms a load-bearing framework. Laser-annealing homogenizes stresses and reduces the spin crossover pressure. Whether seismic waves passing through polymineralic rocks in the lower mantle could induce changes in the spin state of ferropericlase by changing the local pressure, would be an interesting query for future studies.

6.4. Predicted characteristics of the spin crossover signal in seismic observations

Recognizing the signal of the spin crossover in seismic observations and mapping the spin state of the lower mantle is important for seismic inversions of the thermochemical structure of the mantle and for geodynamic modelling. The contrasting effects of the spin crossover on the bulk and shear modulus of ferropericlase form the basis of its characteristic seismic signal, leading to high ratios of V_S to V_C and V_P..

As shown in Chapter 2, the spin crossover produces a strong negative anomaly in the correlation between radially-averaged V_C and V_S variations, as well as a moderate increase of the ratio between V_S and V_P variations at mid-lower mantle depths for an isochemical pyrolitic mantle model.

However, these features are partly obscured in data-based seismic tomography models, due to their limited resolution resulting from heterogeneous data coverage and inherent damping of the tomographic inversion. Hence, it is important to take realistic tomographic resolution into account when searching for the spin crossover signal in tomographic models. Nonetheless, the negative anomaly in S-C correlation promises to be a useful tool to map the spin crossover in seismic tomography models, particularly if the detail of such models can be improved. While this is challenging, due to the computational cost of improving resolution for models at high frequencies, global full-waveform inversion is now starting to become feasible, as evidenced by model *GLAD-M25* (Lei et al., 2020).

An alternative approach to constraining the occurrence and distribution of the spin crossover in the lower mantle is to look for its signal directly in seismic travel-time data. In Chapter 3, I showed that the spin crossover-induced delays in P-wave arrivals cause a characteristic increase in the ratio between travel-time anomalies of S- and P-waves ($\Delta S/\Delta P$). Because of the temperature dependence of the spin crossover, this signal is expected to occur at greater epicentral distances (i.e., greater depths) in hotter regions of the lower mantle and might thus be used in the future to constrain the temperature distribution of the mantle.

6.5. Evidence for the occurrence of the spin crossover in the lower mantle from seismic observations

Since the spin crossover in ferropericlase was first observed experimentally (Badro et al., 2003), many studies have observed a marked, albeit gradual, effect on seismic velocities (Crowhurst et al., 2008; Marquardt et al., 2009a; Wu & Wentzcovitch, 2014; Yang et al., 2015) and on that basis predicted that the spin crossover could produce a detectable seismic signal in the Earth's mantle. However, it is only in the last three years that the first evidence from seismic observations for the occurrence of the spin crossover in the lower mantle has been reported (Cobden et al., 2024; Kennett, 2021; Shephard et al., 2021; Trautner et al., 2023).

Kennett (2021) reported a change in the slope of the elastic modulus ratio G/K as a function of scaled pressure P/K around 1550 km depth in the *ak135* body-wave model of radial Earth structure,

which they attributed to the spin crossover. Shephard et al. (2021) produced vote maps of regions with fast and slow wave speeds from four P-wave tomography models and four S-wave tomography models and suggested that differences in the relative abundances of such regions between the P- and S-wave models at mid-lower mantle depths are caused by the spin crossover. Cobden et al. (2024) compared the fit of hypothetical mantle models for a wide range of compositions and temperatures to global full-waveform tomography model *GLAD-M25* and found that models including the effects of the spin crossover on the properties of ferropericlase produced the best fit. In Chapter 2 (based on Trautner et al. (2023)), the fit between synthetic tomography models for a pyrolitic lower mantle and tomography model *SP12RTS*, which inverted jointly for V_S and V_P variations, is shown to improve significantly when the effects of the spin crossover are included. Finally, I demonstrated in Chapter 3 that a spin-crossover induced increase in the ratio between travel-time anomalies of S- and P-waves with epicentral distance is in qualitative agreement with observations from a global set of travel-time measurements.

Given the variety of methods and types of seismic data used in these studies, the cumulative evidence for the seismic detectability of the spin crossover in Earth's mantle seems robust. So far, studies have largely focussed on the effects of the spin crossover on 1D average velocity structure, although the temperature-dependence of the seismic expression has started to be explored (see Shephard et al. (2021) and Chapter 3). Investigating the geographical distribution of the spin crossover signal in seismic observations and linking it to lateral and vertical temperature variations in the lower mantle will be a pivotal next step. It is important, however, that the effects of potential chemical heterogeneities on the iron content and thus spin state of ferropericlase are considered in such studies.

6.6. Concluding remarks

Studying the inner workings of the Earth is important to improve our understanding of the dynamic processes that have linked the surface and deep interior throughout the formation and evolution of our planet. Seismic observations hold a wealth of information about the composition and thermal state of the deep Earth, but the key to accessing this lies in a detailed understanding of the physical

properties of mantle materials. By mapping how the spin crossover affects the properties of ferropericlase in *P-T-X* space and showing how these effects manifest in seismic data, I hope to have contributed to this pursuit in a small way. There is certainly more to be done on these topics, as discussed in the previous sections. However, the strong evidence for the occurrence of the spin crossover in Earth's lower mantle presented here and in other recent studies warrants consideration of its effects on mantle properties in seismic inversions and geodynamic models. This is increasingly appreciated by the scientific community, with effects of the spin crossover recently being included in self-consistent thermodynamics computations (Stixrude & Lithgow-Bertelloni, 2024) and inversions for the thermo-chemical state of the mantle (Cobden et al., 2024; Deng et al., 2023). Many questions regarding the processes governing Earth's deep interior remain, but as quantitative constraints on the physical properties of mantle minerals advance and seismic resolution improves, we get closer to resolving them.

RES ARDUA VETUSTIS NOVITATEM DARE, NOVIS AUCTORITATEM, OBSOLETIS NITOREM, OBSCURIS LUCEM, FASTIDITIS GRATIAM, DUBIIS FIDEM, OMNIBUS VERO NATURAM ET NATURAE SUA OMNIA. ITAQUE ETIAM NON ASSECUTIS VOLUISSE ABUNDE PULCHRUM ATQUE MAGNIFICUM EST.

"It is a challenging endeavour to give novelty to things long-established, authority to what is new, shine to the trite, insight to the obscure, esteem to what is disdained, confidence to the unresolved, to give to all things their particular nature and to nature all her facets. Therefore, even not having been successful, to have had the intention is abundantly honourable and indeed commendable."

Pliny the Elder, *Naturalis Historia*, Dedication (Book 1)

References

Allègre, C. J. & Turcotte, D. L. (1986). Implications of a two-component marble-cake mantle. *Nature*, *323*, (6084), 123-127. https://doi.org/10.1038/323123a0

Ammann, M. W., Brodholt, J. P. & Dobson, D. P. (2011). Ferrous iron diffusion in ferro-periclase across the spin transition. *Earth and Planetary Science Letters*, *302*, (3), 393-402. https://doi.org/10.1016/j.epsl.2010.12.031

Andrault, D., Fiquet, G., Itié, J.-P., Richet, P., Gillet, P., Häusermann, D. & Hanfland, M. (1998). Thermal pressure in the laser-heated diamond-anvil cell: An X-ray diffraction study. *European Journal of Mineralogy*, *10*, (5), 931-940. https://doi.org/10.1127/ejm/10/5/0931

Angel, R. J. (2000). Equations of State. In R. M. Hazen and R. T. Downs (Eds.), *High-temperature and high-pressure crystal chemistry* (pp. 35-60). Washington, DC: The Mineralogical Society of America.

Antonangeli, D., Siebert, J., Aracne, C. M., Farber, D. L., Bosak, A., Hoesch, M., Krisch, M., Ryerson, F. J., Fiquet, G. & Badro, J. (2011). Spin Crossover in Ferropericlase at High Pressure: A Seismologically Transparent Transition? *Science*, *331*, (6013), 64-67. https://doi.org/10.1126/science.1198429

Badro, J., Fiquet, G., Guyot, F., Rueff, J.-P., Struzhkin, V. V., Vankó, G. & Monaco, G. (2003). Iron Partitioning in Earth's Mantle: Toward a Deep Lower Mantle Discontinuity. *Science*, *300*, (5620), 789-791. https://doi.org/10.1126/science.1081311

Badro, J., Rueff, J.-P., Vankó, G., Monaco, G., Fiquet, G. & Guyot, F. (2004). Electronic Transitions in Perovskite: Possible Nonconvecting Layers in the Lower Mantle. *Science*, *305*, (5682), 383-386. https://doi.org/10.1126/science.1098840

Badro, J. (2014). Spin Transitions in Mantle Minerals. *Annual Review of Earth and Planetary Sciences*, *42*, (1), 231-248. https://doi.org/10.1146/annurev-earth-042711-105304

Ballaran, T. B., Kurnosov, A., Glazyrin, K., Frost, D. J., Merlini, M., Hanfland, M. & Caracas, R. (2012). Effect of chemistry on the compressibility of silicate perovskite in the lower mantle. *Earth and Planetary Science Letters*, *333-334*, 181-190. https://doi.org/10.1016/j.epsl.2012.03.029

Ballmer, M. D., Houser, C., Hernlund, J. W., Wentzcovitch, R. M. & Hirose, K. (2017). Persistence of strong silica-enriched domains in the Earth's lower mantle. *Nature Geoscience*, *10*, (3), 236-240. https://doi.org/10.1038/ngeo2898

Beyreuther, M., Barsch, R., Krischer, L., Megies, T., Behr, Y. & Wassermann, J. (2010). ObsPy: A Python Toolbox for Seismology. *Seismological research letters*, *81*, (3), 530-533. https://doi.org/10.1785/gssrl.81.3.530

Birch, F. (1947). Finite elastic strain of cubic crystals. *Physical review*, *71*, (11), 809-824. https://doi.org/10.1103/PhysRev.71.809

Bishop, C. M. (1995). *Neural networks for pattern recognition*. Oxford: Oxford University Press.

Blöchl, P. E. (1994). Projector augmented-wave method. *Physical Review B*, *50*, (24), 17953-17979. https://doi.org/10.1103/PhysRevB.50.17953

Buchen, J. (2021). Seismic Wave Velocities in Earth's Mantle from Mineral Elasticity. In H. Marquardt, M. D. Ballmer, S. Cottaar and J. Konter (Eds.), *Mantle Convection and Surface Expressions* (pp. 51-95). Washington, DC: American Geophysical Union.

Buchen, J., Wang, B., Satta, N., Trautner, V., Criniti, G., San José Méndez, A., Liermann, H.-P. & Marquardt, H. (2023). Stress and Strain Partitioning in Polycrystalline Materials at High Pressures and Seismic Frequencies. *AGU Fall Meeting Abstracts.*

Burns, R. G. (1993). *Mineralogical applications of crystal field theory*. Cambridge: Cambridge University Press.

Cammarano, F., Marquardt, H., Speziale, S. & Tackley, P. J. (2010). Role of iron-spin transition in ferropericlase on seismic interpretation: A broad thermochemical transition in the mid mantle? *Geophysical Research Letters*, *37*, L03308. https://doi.org/10.1029/2009gl041583

Catalli, K., Shim, S.-H., Prakapenka, V. B., Zhao, J., Sturhahn, W., Chow, P., Xiao, Y., Liu, H., Cynn, H. & Evans, W. J. (2010). Spin state of ferric iron in $MgSiO_3$ perovskite and its effect on elastic properties. *Earth and Planetary Science Letters*, *289*, (1-2), 68-75. https://doi.org/10.1016/j.epsl.2009.10.029

Chang, Y.-Y., Jacobsen, S. D., Lin, J.-F., Bina, C. R., Thomas, S.-M., Wu, J., Shen, G., Xiao, Y., Chow, P., Frost, D. J., McCammon, C. A. & Dera, P. (2013). Spin transition of Fe^{3+} in Al-bearing phase D: An alternative explanation for small-scale seismic scatterers in the mid-lower mantle. *Earth and Planetary Science Letters*, *382*, 1-9. https://doi.org/10.1016/j.epsl.2013.08.038

Chaves, C. A. M., Ritsema, J. & Koelemeijer, P. (2021). Comparing ray-theoretical and finite-frequency teleseismic traveltimes: implications for constraining the ratio of S-wave to P-wave velocity variations in the lower mantle. *Geophysical Journal International*, *224*, (3), 1540-1552. https://doi.org/https://doi.org/10.1093/gji/ggaa534

Chen, B., Jackson, J. M., Sturhahn, W., Zhang, D., Zhao, J., Wicks, J. K. & Murphy, C. A. (2012). Spin crossover equation of state and sound velocities of $(Mg_{0.65}Fe_{0.35})O$ ferropericlase to 140 GPa. *Journal of Geophysical Research: Solid Earth*, *117*, B08208. https://doi.org/10.1029/2012jb009162

Cheng, Y., Wang, X., Zhang, J., Yang, K., Zhang, C., Zeng, Z. & Lin, H. (2018). Investigation of iron spin crossover pressure in Fe-bearing MgO using hybrid functional. *Journal of Physics: Condensed Matter*, *30*, 155403. https://doi.org/10.1088/1361-648x/aab4b5

Cobden, L., Thomas, C. & Trampert, J. (2015). Seismic Detection of Post-perovskite Inside the Earth. In A. Khan and F. Deschamps (Eds.), *The Earth's Heterogeneous Mantle : a geophysical, geodynamical, and geochemical perspective* (pp. 391-440). Springer Cham.

Cobden, L., Zhuang, J., Lei, W., Wentzcovitch, R., Trampert, J. & Tromp, J. (2024). Full-waveform tomography reveals iron spin crossover in Earth's lower mantle. *Nature Communications*, *15*, (1), https://doi.org/10.1038/s41467-024-46040-1

Coelho, A. A. (2018). TOPAS and TOPAS-Academic: an optimization program integrating computer algebra and crystallographic objects written in C++. *Journal of Applied Crystallography*, *51*, (1), 210-218. https://doi.org/10.1107/s1600576718000183

Cordier, P., Gouriet, K., Weidner, T., Van Orman, J., Castelnau, O., Jackson, J. M. & Carrez, P. (2023). Periclase deforms more slowly than bridgmanite under mantle conditions. *Nature*, *613*, (7943), 303-307. https://doi.org/10.1038/s41586-022-05410-9

Criniti, G., Kurnosov, A., Boffa Ballaran, T. & Frost, D. J. (2021). Single-Crystal Elasticity of $MgSiO_3$ Bridgmanite to Mid-Lower Mantle Pressure. *Journal of Geophysical Research: Solid Earth*, *126*, (5), e2020JB020967. https://doi.org/10.1029/2020jb020967

Crowhurst, J. C., Brown, J. M., Goncharov, A. F. & Jacobsen, S. D. (2008). Elasticity of (Mg,Fe)O Through the Spin Transition of Iron in the Lower Mantle. *Science*, *319*, (5862), 451-453. https://doi.org/10.1126/science.1149606

Datchi, F., Loubeyre, P. & Letoullec, R. (2000). Extended and accurate determination of the melting curves of argon, helium, ice (H_2O), and hydrogen (H_2). *Physical Review B*, *61*, (10), 6535-6546. https://doi.org/10.1103/physrevb.61.6535

Davies, D. R., Goes, S., Davies, J. H., Schuberth, B. S. A., Bunge, H. P. & Ritsema, J. (2012). Reconciling dynamic and seismic models of Earth's lower mantle: The dominant role of thermal heterogeneity. *Earth and Planetary Science Letters*, *353-354*, 253-269. https://doi.org/10.1016/j.epsl.2012.08.016

Day, J. M. D., Jones, T. D. & Nicklas, R. W. (2022). Mantle sources of ocean islands basalts revealed from noble gas isotope systematics. *Chemical geology*, *587*, 120626. https://doi.org/10.1016/j.chemgeo.2021.120626

Deng, X., Xu, Y., Hao, S., Ruan, Y., Zhao, Y., Wang, W., Ni, S. & Wu, Z. (2023). Compositional and thermal state of the lower mantle from joint 3D inversion with seismic tomography and mineral elasticity. *Proceedings of the National Academy of Sciences*, *120*, (26), e2220178120. https://doi.org/10.1073/pnas.2220178120

Deschamps, F. & Trampert, J. (2003). Mantle tomography and its relation to temperature and composition. *Physics of the Earth and Planetary Interiors*, *140*, (4), 277-291. https://doi.org/10.1016/j.pepi.2003.09.004

Deschamps, F., Li, Y. & Tackley, P. J. (2015). Large-Scale Thermo-chemical Structure of the Deep Mantle: Observations and Models. In A. Khan and F. Deschamps (Eds.), *The Earth's Heterogeneous Mantle : a geophysical, geodynamical, and geochemical perspective* (pp. 479-515). Springer Cham.

Dewaele, A., Belonoshko, A. B., Garbarino, G., Occelli, F., Bouvier, P., Hanfland, M. & Mezouar, M. (2012). High-pressure–high-temperature equation of state of KCl and KBr. *Physical Review B*, *85*, 214105. https://doi.org/10.1103/physrevb.85.214105

Dong, W., Glazyrin, K., Khandarkhaeva, S., Fedotenko, T., Bednarčík, J., Greenberg, E., Dubrovinsky, L., Dubrovinskaia, N. & Liermann, H.-P. (2022). $Fe_{0.79}Si_{0.07}B_{0.14}$ metallic glass gaskets for high-pressure research beyond 1 Mbar. *Journal of Synchrotron Radiation*, *29*, (5), 1167-1179. https://doi.org/10.1107/s1600577522007573

Dudarev, S. L., Botton, G. A., Savrasov, S. Y., Humphreys, C. J. & Sutton, A. P. (1998). Electron-energy-loss spectra and the structural stability of nickel oxide: An LSDA+U study. *Physical Review B*, *57*, (3), 1505-1509. https://doi.org/10.1103/PhysRevB.57.1505

Dziewonski, A. M. & Anderson, D. L. (1981). Preliminary reference Earth model. *Physics of the Earth and Planetary Interiors*, *25*, (4), 297-356. https://doi.org/10.1016/0031-9201(81)90046-7

Faccenda, M. & Dal Zilio, L. (2017). The role of solid–solid phase transitions in mantle convection. *Lithos*, *268-271*, 198-224. https://doi.org/10.1016/j.lithos.2016.11.007

Fei, H., Liu, Z., Mccammon, C. & Katsura, T. (2020). Oxygen Vacancy Substitution Linked to Ferric Iron in Bridgmanite at 27 GPa. *Geophysical Research Letters*, *47*, (6), e2019GL086296. https://doi.org/10.1029/2019gl086296

Fei, H., Faul, U. & Katsura, T. (2021). The grain growth kinetics of bridgmanite at the topmost lower mantle. *Earth and Planetary Science Letters*, *561*, 116820. https://doi.org/10.1016/j.epsl.2021.116820

Fei, Y., Mao, H.-k., Shu, J. & Hu, J. (1992). P-V-T equation of state of magnesiowüstite $(Mg_{0.6}Fe_{0.4})O$. *Physics and Chemistry of Minerals*, *18*, (7), 416-422. https://doi.org/10.1007/BF00200964

Fei, Y., Ricolleau, A., Frank, M., Mibe, K., Shen, G. & Prakapenka, V. (2007a). Toward an internally consistent pressure scale. *Proceedings of the National Academy of Sciences*, *104*, (22), 9182-9186. https://doi.org/10.1073/pnas.0609013104

Fei, Y., Zhang, L., Corgne, A., Watson, H., Ricolleau, A., Meng, Y. & Prakapenka, V. (2007b). Spin transition and equations of state of (Mg, Fe)O solid solutions. *Geophysical Research Letters*, *34*, L17307. https://doi.org/10.1029/2007gl030712

Finkelstein, G. J., Jackson, J. M., Sturhahn, W., Zhang, D., Alp, E. E. & Toellner, T. S. (2017). Single-crystal equations of state of magnesiowüstite at high pressures. *American Mineralogist*, *102*, (8), 1709-1717. https://doi.org/10.2138/am-2017-5966

Finkelstein, G. J., Jackson, J. M., Said, A., Alatas, A., Leu, B. M., Sturhahn, W. & Toellner, T. S. (2018). Strongly Anisotropic Magnesiowüstite in Earth's Lower Mantle. *Journal of Geophysical Research: Solid Earth*, *123*, (6), 4740-4750. https://doi.org/10.1029/2017jb015349

Forte, A. M., Simmons, N. A. & Grand, S. P. (2015). Constraints on Seismic Models from Other Disciplines - Constraints on 3-D Seismic Models from Global Geodynamic Observables: Implications for the Global Mantle Convective Flow. In G. Schubert (Eds.), *Treatise on Geophysics* (pp. 853-907). The Netherlands: Elsevier.

Fu, S., Yang, J., Zhang, Y., Okuchi, T., Mccammon, C., Kim, H. I., Lee, S. K. & Lin, J. F. (2018). Abnormal Elasticity of Fe-Bearing Bridgmanite in the Earth's Lower Mantle. *Geophysical Research Letters*, *45*, (10), 4725-4732. https://doi.org/10.1029/2018gl077764

Fukui, H., Tsuchiya, T. & Baron, A. Q. R. (2012). Lattice dynamics calculations for ferropericlase with internally consistent LDA+*U* method. *Journal of Geophysical Research: Solid Earth*, *117*, B12202. https://doi.org/10.1029/2012jb009591

Fukui, H., Baron, A. Q. R., Ishikawa, D., Uchiyama, H., Ohishi, Y., Tsuchiya, T., Kobayashi, H., Matsuzaki, T., Yoshino, T. & Katsura, T. (2017). Pressure dependence of transverse acoustic phonon energy in ferropericlase across the spin transition. *Journal of Physics: Condensed Matter*, *29*, 245401. https://doi.org/10.1088/1361-648x/aa7026

Fyfe, W. S. (1960). The possibility of d-electron coupling in olivine at high pressures. *Geochimica et cosmochimica acta*, *19*, (2), 141-143. https://doi.org/10.1016/0016-7037(60)90046-6

Garnero, E. J., Mcnamara, A. K. & Shim, S.-H. (2016). Continent-sized anomalous zones with low seismic velocity at the base of Earth's mantle. *Nature Geoscience*, *9*, (7), 481-489. https://doi.org/10.1038/ngeo2733

Girard, J., Amulele, G., Farla, R., Mohiuddin, A. & Karato, S.-i. (2016). Shear deformation of bridgmanite and magnesiowüstite aggregates at lower mantle conditions. *Science*, *351*, (6269), 144-147. https://doi.org/10.1126/science.aad3113

Glazyrin, K., Miyajima, N., Smith, J. S. & Lee, K. K. M. (2016). Compression of a multiphase mantle assemblage: Effects of undesirable stress and stress annealing on the iron spin state crossover in ferropericlase. *Journal of Geophysical Research: Solid Earth*, *121*, (5), 3377-3392. https://doi.org/10.1002/2015jb012321

Glazyrin, K., Sinmyo, R., Bykova, E., Bykov, M., Cerantola, V., Longo, M., Mccammon, C. A., Prakapenka, V. B. & Dubrovinsky, L. (2017). Critical behavior of $Mg_{1-x}Fe_xO$ at the pressure-induced iron spin-state crossover. *Physical Review B*, *95*, 214412. https://doi.org/10.1103/physrevb.95.214412

Goldstein, J. I., Newbury, D. E., Michael, J. R., Ritchie, N. W. M., Scott, J. H. J. & Joy, D. C. (2018). *Scanning Electron Microscopy and X-Ray Microanalysis*. New York, NY: Springer New York.

Gülcher, A. J. P., Ballmer, M. D. & Tackley, P. J. (2021). Coupled dynamics and evolution of primordial and recycled heterogeneity in Earth's lower mantle. *Solid Earth*, *12*, (9), 2087-2107. https://doi.org/10.5194/se-12-2087-2021

Hamada, M., Kamada, S., Ohtani, E., Sakamaki, T., Mitsui, T., Masuda, R., Hirao, N., Ohishi, Y. & Akasaka, M. (2021). Synchrotron Mössbauer spectroscopic and X-ray diffraction study of ferropericlase in the high-pressure range of the lower mantle region. *Physical Review B*, *103*, 174108. https://doi.org/10.1103/PhysRevB.103.174108

Handy, M. R. (1994). Flow laws for rocks containing two non-linear viscous phases: A phenomenological approach. *Journal of structural geology*, *16*, (3), 287-301. https://doi.org/10.1016/0191-8141(94)90035-3

Hill, R. (1952). The Elastic Behaviour of a Crystalline Aggregate. *Proceedings of the Physical Society. Section A*, *65*, (5), 349-354. https://doi.org/10.1088/0370-1298/65/5/307

Hirose, K., Sinmyo, R. & Hernlund, J. (2017). Perovskite in Earth's deep interior. *Science*, *358*, (6364), 734-738. https://doi.org/10.1126/science.aam8561

Holmström, E. & Stixrude, L. (2015). Spin crossover in ferropericlase from first-principles molecular dynamics. *Physical Review Letters*, *114*, 117202. https://doi.org/10.1103/PhysRevLett.114.117202

Huang, R., Boffa Ballaran, T., Mccammon, C. A., Miyajima, N., Dolejš, D. & Frost, D. J. (2021). The composition and redox state of bridgmanite in the lower mantle as a function of oxygen fugacity. *Geochimica et cosmochimica acta*, *303*, 110-136. https://doi.org/10.1016/j.gca.2021.02.036

Hung, S. H., Dahlen, F. A. & Nolet, G. (2000). Fréchet kernels for finite-frequency traveltimeséII. Examples. *Geophysical Journal International*, *141*, (1), 175-203. https://doi.org/10.1046/j.1365-246X.2000.00072.x

Huston, L. Q., Miyagi, L., Husband, R. J., Glazyrin, K., Kiessner, C., Wendt, M., Liermann, H. P. & Sturtevant, B. T. (2024). New dynamic diamond anvil cell for time-resolved radial x-ray diffraction. *Review of Scientific Instruments*, *95*, (4), https://doi.org/10.1063/5.0179799

Immoor, J., Miyagi, L., Liermann, H.-P., Speziale, S., Schulze, K., Buchen, J., Kurnosov, A. & Marquardt, H. (2022). Weak cubic $CaSiO_3$ perovskite in the Earth's mantle. *Nature*, *603*, (7900), 276-279. https://doi.org/10.1038/s41586-021-04378-2

Irifune, T., Shinmei, T., McCammon, C. A., Miyajima, N., Rubie, D. C. & Frost, D. J. (2010). Iron Partitioning and Density Changes of Pyrolite in Earth's Lower Mantle. *Science*, *327*, (5962), 193-195. https://doi.org/10.1126/science.1181443

Irifune, T. & Tsuchiya, T. (2015). 2.03 - Phase Transitions and Mineralogy of the Lower Mantle. In G. Schubert (Eds.), *Treatise on Geophysics* (pp. 33-60). Elsevier B.V.

Jackson, I., Webb, S., Weston, L. & Boness, D. (2005). Frequency dependence of elastic wave speeds at high temperature: a direct experimental demonstration. *Physics of the Earth and Planetary Interiors*, *148*, (1), 85-96. https://doi.org/10.1016/j.pepi.2004.08.004

Jackson, M. G., Blichert-Toft, J., Halldórsson, S. A., Mundl-Petermeier, A., Bizimis, M., Kurz, M. D., Price, A. A., Harðardóttir, S., Willhite, L. N., Breddam, K., Becker, T. W. & Fischer, R. A. (2020). Ancient helium and tungsten isotopic signatures preserved in mantle domains least modified by crustal recycling. *Proceedings of the National Academy of Sciences*, *117*, (49), 30993-31001. https://doi.org/10.1073/pnas.2009663117

Jacobsen, S. D., Reichmann, H.-J., Spetzler, H. A., Mackwell, S. J., Smyth, J. R., Angel, R. J. & McCammon, C. A. (2002). Structure and elasticity of single-crystal (Mg,Fe)O and a new method of generating shear waves for gigahertz ultrasonic interferometry. *Journal of Geophysical Research*, *107*, (B2), ECV 4-1 - ECV 4-14. https://doi.org/10.1029/2001jb000490

Jacobsen, S. D., Lin, J.-F., Angel, R. J., Shen, G., Prakapenka, V. B., Dera, P., Mao, H.-K. & Hemley, R. J. (2005). Single-crystal synchrotron X-ray diffraction study of wüstite and magnesiowüstite at lower-mantle pressures. *Journal of Synchrotron Radiation*, *12*, (5), 577-583. https://doi.org/10.1107/s0909049505022326

Jenei, Z., Liermann, H. P., Husband, R., Mendez, A. S. J., Pennicard, D., Marquardt, H., O'Bannon, E. F., Pakhomova, A., Konopkova, Z., Glazyrin, K., Wendt, M., Wenz, S., McBride, E. E., Morgenroth, W., Winkler, B., Rothkirch, A., Hanfland, M. & Evans, W. J. (2019). New dynamic diamond anvil cells for tera-pascal per second fast compression x-ray diffraction experiments. *Review of Scientific Instruments*, *90*, 065114. https://doi.org/10.1063/1.5098993

Kantor, I., Dubrovinsky, L., McCammon, C. A., Kantor, A., Pascarelli, S., Aquilanti, G., Crichton, W., Mattesini, M., Ahuja, R., Almeida, J. & Urusov, V. (2006). Pressure-induced phase transition in $Mg_{0.8}Fe_{0.2}O$ ferropericlase. *Physics and Chemistry of Minerals*, *33*, 35-44. https://doi.org/10.1007/s00269-005-0052-z

Kantor, I., Dubrovinsky, L., McCammon, C. A., Steinle-Neumann, G., Kantor, A., Skorodumova, N., Pascarelli, S. & Aquilanti, G. (2009). Short-range order and Fe clustering in $Mg_{1-x}Fe_xO$ under high pressure. *Physical Review B*, *80*, 014204. https://doi.org/10.1103/PhysRevB.80.014204

Karato, S.-i. (2008). *Deformation of earth materials: an introduction to the rheology of solid earth*. Cambridge: Cambridge University Press.

Kennett, B. L. N. (2021). The relative behaviour of bulk and shear modulus as an indicator of the iron spin transition in the lower mantle. *Earth and Planetary Science Letters*, *559*, 116808. https://doi.org/10.1016/j.epsl.2021.116808

Kiseeva, E. S., Korolev, N., Koemets, I., Zedgenizov, D. A., Unitt, R., Mccammon, C., Aslandukova, A., Khandarkhaeva, S., Fedotenko, T., Glazyrin, K., Bessas, D., Aprilis, G., Chumakov, A. I., Kagi, H. & Dubrovinsky, L. (2022). Subduction-related oxidation of the sublithospheric mantle evidenced by ferropericlase and magnesiowüstite diamond inclusions. *Nature Communications*, *13*, 7517. https://doi.org/10.1038/s41467-022-35110-x

Koelemeijer, P., Ritsema, J., Deuss, A. & Van Heijst, H.-J. (2016). SP12RTS: a degree-12 model of shear- and compressional-wave velocity for Earth's mantle. *Geophysical Journal International*, *204*, (2), 1024-1039. https://doi.org/10.1093/gji/ggv481

Koelemeijer, P., Schuberth, B. S. A., Davies, D. R., Deuss, A. & Ritsema, J. (2018). Constraints on the presence of post-perovskite in Earth's lowermost mantle from tomographic-geodynamic model comparisons. *Earth and Planetary Science Letters*, *494*, 226-238. https://doi.org/10.1016/j.epsl.2018.04.056

Komabayashi, T., Hirose, K., Nagaya, Y., Sugimura, E. & Ohishi, Y. (2010). High-temperature compression of ferropericlase and the effect of temperature on iron spin transition. *Earth and Planetary Science Letters*, *297*, (3-4), 691-699. https://doi.org/10.1016/j.epsl.2010.07.025

Kresse, G. & Furthmüller, J. (1996a). Efficiency of ab-initio total energy calculations for metals and semiconductors using a plane-wave basis set. *Computational Materials Science*, *6*, (1), 15-50. https://doi.org/https://doi.org/10.1016/0927-0256(96)00008-0

Kresse, G. & Furthmüller, J. (1996b). Efficient iterative schemes for ab initio total-energy calculations using a plane-wave basis set. *Physical Review B*, *54*, (16), 11169-11186. https://doi.org/10.1103/PhysRevB.54.11169

Kresse, G. & Joubert, D. (1999). From ultrasoft pseudopotentials to the projector augmented-wave method. *Physical Review B*, *59*, (3), 1758-1775. https://doi.org/10.1103/PhysRevB.59.1758

Kurnosov, A., Marquardt, H., Frost, D. J., Ballaran, T. B. & Ziberna, L. (2017). Evidence for a Fe^{3+}-rich pyrolitic lower mantle from (Al,Fe)-bearing bridgmanite elasticity data. *Nature*, *543*, (7646), 543-546. https://doi.org/10.1038/nature21390

Lay, T. (2015). 1.22 - Deep Earth Structure: Lower Mantle and D". In G. Schubert (Eds.), *Treatise on Geophysics* (pp. 683-723). Elsevier B.V.

Lei, W., Ruan, Y., Bozdağ, E., Peter, D., Lefebvre, M., Komatitsch, D., Tromp, J., Hill, J., Podhorszki, N. & Pugmire, D. (2020). Global adjoint tomography—model GLAD-M25. *Geophysical Journal International*, *223*, (1), 1-21. https://doi.org/10.1093/gji/ggaa253

Leng, K., Nissen-Meyer, T., Driel, V., Martin, Hosseini, K. & Al-Attar, D. (2019). AxiSEM3D: broad-band seismic wavefields in 3-D global earth models with undulating discontinuities. *Geophysical Journal International*, *217*, (3), 2125-2146. https://doi.org/10.1093/gji/ggz092

Li, M., Mcnamara, A. K., Garnero, E. J. & Yu, S. (2017). Compositionally-distinct ultra-low velocity zones on Earth's core-mantle boundary. *Nature Communications*, *8*, 177. https://doi.org/10.1038/s41467-017-00219-x

Liermann, H.-P., Konôpková, Z., Morgenroth, W., Glazyrin, K., Bednarčik, J., Mcbride, E. E., Petitgirard, S., Delitz, J. T., Wendt, M., Bican, Y., Ehnes, A., Schwark, I., Rothkirch, A.,

Tischer, M., Heuer, J., Schulte-Schrepping, H., Kracht, T. & Franz, H. (2015). The Extreme Conditions Beamline P02.2 and the Extreme Conditions Science Infrastructure at PETRA III. *Journal of Synchrotron Radiation*, *22*, (4), 908-924. https://doi.org/10.1107/s1600577515005937

Lin, J.-F., Struzhkin, V. V., Jacobsen, S. D., Hu, M. Y., Chow, P., Kung, J., Liu, H., Mao, H.-K. & Hemley, R. J. (2005). Spin transition of iron in magnesiowüstite in the Earth's lower mantle. *Nature*, *436*, (7049), 377-380. https://doi.org/10.1038/nature03825

Lin, J.-F., Vankó, G., Jacobsen, S. D., Iota, V., Struzhkin, V. V., Prakapenka, V. B., Kuznetsov, A. & Yoo, C.-S. (2007a). Spin transition zone in Earth's lower mantle. *Science*, *317*, (5845), 1740-1743. https://doi.org/10.1126/science.1144997

Lin, J.-F., Speziale, S., Mao, Z. & Marquardt, H. (2013). Effects of the Electronic Spin Transitions of Iron in Lower Mantle Minerals: Implications for Deep Mantle Geophysics and Geochemistry. *Reviews of Geophysics*, *51*, (2), 244-275. https://doi.org/10.1002/rog.20010

Lin, J. F., Weir, S. T., Jackson, D. D., Evans, W. J., Vohra, Y. K., Qiu, W. & Yoo, C. S. (2007b). Electrical conductivity of the lower-mantle ferropericlase across the electronic spin transition. *Geophysical Research Letters*, *34*, L16305. https://doi.org/10.1029/2007gl030523

Liu, J., Li, J., Hrubiak, R. & Smith, J. S. (2016). Origins of ultralow velocity zones through slab-derived metallic melt. *Proceedings of the National Academy of Sciences*, *113*, (20), 5547-5551. https://doi.org/10.1073/pnas.1519540113

Longo, M., Mccammon, C. A. & Jacobsen, S. D. (2011). Microanalysis of the iron oxidation state in (Mg,Fe)O and application to the study of microscale processes. *Contributions to mineralogy and petrology*, *162*, (6), 1249-1257. https://doi.org/10.1007/s00410-011-0649-9

Mao, H. K., Hemley, R. J., Wu, Y., Jephcoat, A. P., Finger, L. W., Zha, C. S. & Bassett, W. A. (1988). High-Pressure Phase Diagram and Equation of State of Solid Helium from Single-Crystal X-Ray Diffraction to 23.3 GPa. *Physical Review Letters*, *60*, (25), 2649-2652. https://doi.org/10.1103/physrevlett.60.2649

Mao, W., Shu, J., Hu, J., Hemley, R. J. & Mao, H.-K. (2002). Displacive transition in magnesiowüstite. *Journal of Physics: Condensed Matter*, *14*, (44), 11349-11354. https://doi.org/10.1088/0953-8984/14/44/480

Mao, Z., Lin, J.-F., Liu, J. & Prakapenka, V. B. (2011). Thermal equation of state of lower-mantle ferropericlase across the spin crossover. *Geophysical Research Letters*, *38*, L23308. https://doi.org/10.1029/2011gl049915

Mao, Z., Lin, J. F., Yang, J., Inoue, T. & Prakapenka, V. B. (2015). Effects of the Fe^{3+} spin transition on the equation of state of bridgmanite. *Geophysical Research Letters*, *42*, (11), 4335-4342. https://doi.org/10.1002/2015gl064400

Mao, Z., Wang, F., Lin, J.-F., Fu, S., Yang, J., Wu, X., Okuchi, T., Tomioka, N., Prakapenka, V. B., Xiao, Y. & Chow, P. (2017). Equation of state and hyperfine parameters of high-spin bridgmanite in the Earth's lower mantle by synchrotron X-ray diffraction and Mossbauer spectroscopy. *American Mineralogist*, *102*, (2), 357-368. https://doi.org/10.2138/am-2017-5770

Marcondes, M. L., Zheng, F. & Wentzcovitch, R. M. (2020). Phonon dispersion throughout the iron spin crossover in ferropericlase. *Physical Review B*, *102*, (10), https://doi.org/10.1103/physrevb.102.104112

Marquardt, H., Speziale, S., Reichmann, H. J., Frost, D. J. & Schilling, F. R. (2009a). Single-crystal elasticity of $(Mg_{0.9}Fe_{0.1})O$ to 81 GPa. *Earth and Planetary Science Letters*, *287*, (3-4), 345-352. https://doi.org/10.1016/j.epsl.2009.08.017

Marquardt, H., Speziale, S., Reichmann, H. J., Frost, D. J., Schilling, F. R. & Garnero, E. J. (2009b). Elastic Shear Anisotropy of Ferropericlase in Earth's Lower Mantle. *Science*, *324*, (5924), 224-226. https://doi.org/10.1126/science.1169365

Marquardt, H. & Miyagi, L. (2015). Slab stagnation in the shallow lower mantle linked to an increase in mantle viscosity. *Nature Geoscience*, *8*, (4), 311-314. https://doi.org/10.1038/ngeo2393

Marquardt, H., Buchen, J., Mendez, A. S. J., Kurnosov, A., Wendt, M., Rothkirch, A., Pennicard, D. & Liermann, H. P. (2018). Elastic Softening of $(Mg_{0.8}Fe_{0.2})O$ Ferropericlase Across the Iron Spin Crossover Measured at Seismic Frequencies. *Geophysical Research Letters*, *45*, (14), 6862-6868. https://doi.org/10.1029/2018gl077982

Marquardt, H. & Thomson, A. R. (2020). Experimental elasticity of Earth's deep mantle. *Nature Reviews Earth & Environment*, *1*, (9), 455-469. https://doi.org/10.1038/s43017-020-0077-3

Martinez, I., Wang, Y., Guyot, F., Liebermann, R. C. & Doukhan, J. C. (1997). Microstructures and iron partitioning in $(Mg,Fe)SiO_3$ perovskite-(Mg,Fe)O magnesiowüstite assemblages: An analytical transmission electron microscopy study. *Journal of Geophysical Research: Solid Earth*, *102*, (B3), 5265-5280. https://doi.org/10.1029/96jb03188

Masters, G., Laske, G., Bolton, H. & Dziewonski, A. (2000). The Relative Behavior of Shear Velocity, Bulk Sound Speed, and Compressional Velocity in the Mantle: Implications for Chemical and Thermal Structure. In S.-I. Karato, A. M. Forte, R. C. Liebermann, G. Masters and L. Stixrude (Eds.), *Earth's Deep Interior: Mineral Physics and Tomography From the Atomic to the Global Scale* (pp. 63-87). Washington, DC: American Geophysical Union.

Matsui, M., Ito, E., Yamazaki, D., Yoshino, T., Guo, X., Shan, S., Higo, Y. & Funakoshi, K.-I. (2012). Static compression of $(Mg_{0.83},Fe_{0.17})O$ and $(Mg_{0.75},Fe_{0.25})O$ ferropericlase up to 58 GPa at 300, 700, and 1100 K. *American Mineralogist*, *97*, (1), 176-183. https://doi.org/10.2138/am.2012.3937

McCammon, C. A. (1994). A Mössbauer milliprobe: Practical considerations. *Hyperfine Interactions*, *92*, 1235-1239. https://doi.org/10.1007/bf02065761

McCammon, C. A., Peyronneau, J. & Poirier, J.-P. (1998). Low ferric iron content of (Mg,Fe)O at high pressures and temperatures. *Geophysical Research Letters*, *25*, (10), 1589-1592. https://doi.org/10.1029/98gl01178

Méndez, A. S. J., Marquardt, H., Husband, R. J., Schwark, I., Mainberger, J., Glazyrin, K., Kurnosov, A., Otzen, C., Satta, N., Bednarcik, J. & Liermann, H. P. (2020). A resistively-heated dynamic diamond anvil cell (RHdDAC) for fast compression x-ray diffraction experiments at high temperatures. *Review of Scientific Instruments*, *91*, 073906. https://doi.org/10.1063/5.0007557

Méndez, A. S. J., Trybel, F., Husband, R. J., Steinle-Neumann, G., Liermann, H.-P. & Marquardt, H. (2021). Bulk modulus of H_2O across the ice VII–ice X transition measured by time-resolved x-ray diffraction in dynamic diamond anvil cell experiments. *Physical Review B*, *103*, 064104. https://doi.org/10.1103/physrevb.103.064104

Méndez, A. S. J., Stackhouse, S., Trautner, V., Wang, B., Satta, N., Kurnosov, A., Husband, R., Glazyrin, K., Liermann, H. P. & Marquardt, H. (2022). Broad elastic softening of (Mg,Fe)O ferropericlase across the iron spin crossover and a mixed-spin lower mantle. *Journal of Geophysical Research: Solid Earth*, *127*, (8), e2021JB023832. https://doi.org/10.1029/2021jb023832

Miyagi, L. & Wenk, H.-R. (2016). Texture development and slip systems in bridgmanite and bridgmanite + ferropericlase aggregates. *Physics and Chemistry of Minerals*, *43*, (8), 597-613. https://doi.org/10.1007/s00269-016-0820-y

Miyagi, L. (2021). Experimental Deformation of Lower Mantle Rocks and Minerals. In H. Marquardt, M. D. Ballmer, S. Cottaar and J. Konter (Eds.), *Mantle Convection and Surface Expressions* (pp. 21-50). Washington, DC: American Geophysical Union.

Montelli, R., Nolet, G., Dahlen, F. A. & Masters, G. (2006). A catalogue of deep mantle plumes: New results from finite-frequency tomography. *Geochemistry, Geophysics, Geosystems*, *7*, (11), Q11007. https://doi.org/10.1029/2006gc001248

Mosca, I., Cobden, L., Deuss, A., Ritsema, J. & Trampert, J. (2012). Seismic and mineralogical structures of the lower mantle from probabilistic tomography. *Journal of Geophysical Research: Solid Earth*, *117*, B06304. https://doi.org/10.1029/2011jb008851

Muir, J. M. R. & Brodholt, J. P. (2015). Elastic properties of ferropericlase at lower mantle conditions and its relevance to ULVZs. *Earth and Planetary Science Letters*, *417*, 40-48. https://doi.org/10.1016/j.epsl.2015.02.023

Muir, J. M. R. & Brodholt, J. P. (2016). Ferrous iron partitioning in the lower mantle. *Physics of the Earth and Planetary Interiors*, *257*, 12-17. https://doi.org/10.1016/j.pepi.2016.05.008

Mukhopadhyay, S. & Parai, R. (2019). Noble Gases: A Record of Earth's Evolution and Mantle Dynamics. *Annual Review of Earth and Planetary Sciences*, *47*, 389-419. https://doi.org/10.1146/annurev-earth-053018-060238

Müller, R. D., Cannon, J., Qin, X., Watson, R. J., Gurnis, M., Williams, S., Pfaffelmoser, T., Seton, M., Russell, S. H. J. & Zahirovic, S. (2018). GPlates: Building a Virtual Earth Through Deep Time. *Geochemistry, Geophysics, Geosystems*, *19*, (7), 2243-2261. https://doi.org/https://doi.org/10.1029/2018GC007584

Murakami, M., Hirose, K., Kawamura, K., Sata, N. & Ohishi, Y. (2004). Post-Perovskite Phase Transition in $MgSiO_3$. *Science (American Association for the Advancement of Science)*, *304*, (5672), 855-858. https://doi.org/10.1126/science.1095932

Murakami, M. (2005). Post-perovskite phase transition and mineral chemistry in the pyrolitic lowermost mantle. *Geophysical Research Letters*, *32*, L03304. https://doi.org/10.1029/2004gl021956

Murakami, M., Ohishi, Y., Hirao, N. & Hirose, K. (2012). A perovskitic lower mantle inferred from high-pressure, high-temperature sound velocity data. *Nature*, *485*, (7396), 90-94. https://doi.org/10.1038/nature11004

Murnaghan, F. D. (1944). The Compressibility of Media under Extreme Pressures. *Proceedings of the National Academy of Sciences*, *30*, (9), 244-247. https://doi.org/10.1073/pnas.30.9.244

Nomura, R., Ozawa, H., Tateno, S., Hirose, K., Hernlund, J., Muto, S., Ishii, H. & Hiraoka, N. (2011). Spin crossover and iron-rich silicate melt in the Earth's deep mantle. *Nature*, *473*, (7346), 199-202. https://doi.org/10.1038/nature09940

Nosé, S. (1984). A unified formulation of the constant temperature molecular dynamics methods. *The Journal of Chemical Physics*, *81*, (1), 511-519. https://doi.org/10.1063/1.447334

Oganov, A. R., Brodholt, J. P. & Price, G. D. (2001). Ab initio elasticity and thermal equation of state of $MgSiO_3$ perovskite. *Earth and Planetary Science Letters*, *184*, (3), 555-560. https://doi.org/https://doi.org/10.1016/S0012-821X(00)00363-0

Oganov, A. R. & Ono, S. (2004). Theoretical and experimental evidence for a post-perovskite phase of $MgSiO_3$ in Earth's D″ layer. *Nature*, *430*, (6998), 445-448. https://doi.org/10.1038/nature02701

Ohta, K., Hirose, K., Onoda, S. & Shimizu, K. (2007). The effect of iron spin transition on electrical conductivity of (Mg,Fe)O magnesiowüstite. *Proceedings of the Japan Academy, Series B*, *83*, (3), 97-100. https://doi.org/10.2183/pjab.83.97

Okuda, Y., Ohta, K., Sinmyo, R., Hirose, K. & Ohishi, Y. (2020). Anomalous compressibility in (Fe,Al)-bearing bridgmanite: implications for the spin state of iron. *Physics and Chemistry of Minerals*, *47*, 40. https://doi.org/10.1007/s00269-020-01109-3

Otsuka, K. & Karato, S.-I. (2012). Deep penetration of molten iron into the mantle caused by a morphological instability. *Nature*, *492*, (7428), 243-246. https://doi.org/10.1038/nature11663

Otsuka, K., Longo, M., McCammon, C. A. & Karato, S.-i. (2013). Ferric iron content of ferropericlase as a function of composition, oxygen fugacity, temperature and pressure: Implications for redox conditions during diamond formation in the lower mantle. *Earth and Planetary Science Letters*, *365*, 7-16. https://doi.org/10.1016/j.epsl.2012.11.030

Pennicard, D., Smoljanin, S., Pithan, F., Sarajlic, M., Rothkirch, A., Yu, Y., Liermann, H. P., Morgenroth, W., Winkler, B., Jenei, Z., Stawitz, H., Becker, J. & Graafsma, H. (2018). LAMBDA 2M GaAs—A multi-megapixel hard X-ray detector for synchrotrons. *Journal of instrumentation*, *13*, C01026. https://doi.org/10.1088/1748-0221/13/01/C01026

Perdew, J. P. & Zunger, A. (1981). Self-interaction correction to density-functional approximations for many-electron systems. *Physical Review B*, *23*, (10), 5048.

Persson, K., Bengtson, A., Ceder, G. & Morgan, D. (2006). *Ab initio* study of the composition dependence of the pressure-induced spin transition in the $(Mg_{1-x},Fe_x)O$ system. *Geophysical Research Letters*, *33*, (16), https://doi.org/10.1029/2006gl026621

Piet, H., Badro, J., Nabiei, F., Dennenwaldt, T., Shim, S.-H., Cantoni, M., Hébert, C. & Gillet, P. (2016). Spin and valence dependence of iron partitioning in Earth's deep mantle. *Proceedings of the National Academy of Sciences*, *113*, (40), 11127-11130. https://doi.org/10.1073/pnas.1605290113

Prescher, C., McCammon, C. & Dubrovinsky, L. (2012). MossA: a program for analyzing energy-domain Mössbauer spectra from conventional and synchrotron sources. *Journal of Applied Crystallography*, *45*, (2), 329-331. https://doi.org/10.1107/S0021889812004979

Prescher, C. & Prakapenka, V. B. (2015). DIOPTAS: a program for reduction of two-dimensional X-ray diffraction data and data exploration. *High Pressure Research*, *35*, (3), 223-230. https://doi.org/10.1080/08957959.2015.1059835

Raissi, M., Perdikaris, P. & Karniadakis, G. E. (2019). Physics-informed neural networks: A deep learning framework for solving forward and inverse problems involving nonlinear partial differential equations. *Journal of Computational Physics*, *378*, 686-707. https://doi.org/10.1016/j.jcp.2018.10.045

Reuss, A. (1929). Berechnung der Fließgrenze von Mischkristallen auf Grund der Plastizitätsbedingung für Einkristalle. *Zeitschrift für angewandte Mathematik und Mechanik*, *9*, (1), 49-58. https://doi.org/10.1002/zamm.19290090104

Richet, P., Mao, H. K. & Bell, P. M. (1989). Bulk moduli of magnesiowüstites from static compression measurements. *Journal of Geophysical Research: Solid Earth*, *94*, (B3), 3037-3045. https://doi.org/10.1029/jb094ib03p03037

Rijal, A., Cobden, L., Trampert, J., Jackson, J. M. & Valentine, A. (2021). Inferring material properties of the lower mantle minerals using Mixture Density Networks. *Physics of the Earth and Planetary Interiors*, *319*, 106784. https://doi.org/10.1016/j.pepi.2021.106784

Rijal, A. (2023). Applications of machine learning to mineral physics data and the inference of the thermochemical structure of the Earth's mantle. Doctoral dissertation, Utrecht University.

Ringwood, A. E. (1962). A model for the upper mantle. *Journal of Geophysical Research*, *67*, (2), 857-867. https://doi.org/10.1029/jz067i002p00857

Ritsema, J. & van Heijst, H.-J. (2002). Constraints on the correlation of P- and S-wave velocity heterogeneity in the mantle from P, PP, PPP and PKPab traveltimes. *Geophysical Journal International*, *149*, (2), 482-489. https://doi.org/10.1046/j.1365-246X.2002.01631.x

Rosenhauer, M., Mao, H. K. & Woermann, E. (1976). Compressibility of magnesiowüstite $(Mg_{0.6}Fe_{0.4})O$ to 264 kbar. *Year book / Carnegie Institution of Washington*, *75*, 513-515.

Rudolph, M. L., Lekić, V. & Lithgow-Bertelloni, C. (2015). Viscosity jump in Earth's mid-mantle. *Science*, *350*, (6266), 1349-1352. https://doi.org/doi:10.1126/science.aad1929

Saha, S., Bengtson, A., Crispin, K. L., Van Orman, J. A. & Morgan, D. (2011). Effects of spin transition on diffusion of Fe^{2+} in ferropericlase in Earth's lower mantle. *Physical Review B*, *84*, 184102. https://doi.org/10.1103/physrevb.84.184102

Saha, S., Bengtson, A. & Morgan, D. (2013). Effect of anomalous compressibility on Fe diffusion in ferropericlase throughout the spin crossover in the lower mantle. *Earth and Planetary Science Letters*, *362*, 1-5. https://doi.org/10.1016/j.epsl.2012.11.032

Schifferle, L., Speziale, S., Winkler, B., Milman, V. & Lobanov, S. S. (2024). Reduced charge transfer in mixed-spin ferropericlase inferred from its high-pressure refractive index. *American Mineralogist*, *109*, (7), 1145-1152. https://doi.org/10.2138/am-2023-9100

Shannon, R. D. (1976). Revised effective ionic radii and systematic studies of interatomic distances in halides and chalcogenides. *Acta Crystallographica Section A*, *32*, (5), 751-767. https://doi.org/10.1107/S0567739476001551

Shephard, G. E., Matthews, K. J., Hosseini, K. & Domeier, M. (2017). On the consistency of seismically imaged lower mantle slabs. *Scientific Reports*, *7*, 10976. https://doi.org/10.1038/s41598-017-11039-w

Shephard, G. E., Houser, C., Hernlund, J. W., Valencia-Cardona, J. J., Trønnes, R. G. & Wentzcovitch, R. M. (2021). Seismological expression of the iron spin crossover in ferropericlase in the Earth's lower mantle. *Nature Communications*, *12*, 5905. https://doi.org/10.1038/s41467-021-26115-z

Shim, S.-H., Duffy, T. S. & Shen, G. (2000). The equation of state of $CaSiO_3$ perovskite to 108 GPa at 300 K. *Physics of the Earth and Planetary Interiors*, *120*, (4), 327-338. https://doi.org/10.1016/s0031-9201(00)00154-0

Singh, A. K. & Takemura, K. (2001). Measurement and analysis of nonhydrostatic lattice strain component in niobium to 145 GPa under various fluid pressure-transmitting media. *Journal of Applied Physics*, *90*, (7), 3269-3275. https://doi.org/10.1063/1.1397283

Sinmyo, R., Hirose, K., Nishio-Hamane, D., Seto, Y., Fujino, K., Sata, N. & Ohishi, Y. (2008a). Partitioning of iron between perovskite/postperovskite and ferropericlase in the lower mantle. *Journal of Geophysical Research*, *113*, B11204. https://doi.org/10.1029/2008JB005730

Sinmyo, R., Ozawa, H., Hirose, K., Yasuhara, A., Endo, N., Sata, N. & Ohishi, Y. (2008b). Ferric iron content in (Mg,Fe)SiO3 perovskite and post-perovskite at deep lower mantle conditions. *American Mineralogist*, *93*, (11-12), 1899-1902. https://doi.org/10.2138/am.2008.2806

Sinmyo, R. & Hirose, K. (2010). The Soret diffusion in laser-heated diamond-anvil cell. *Physics of the Earth and Planetary Interiors*, *180*, (3-4), 172-178. https://doi.org/10.1016/j.pepi.2009.10.011

Sinmyo, R. & Hirose, K. (2013). Iron partitioning in pyrolitic lower mantle. *Physics and Chemistry of Minerals*, *40*, (2), 107-113. https://doi.org/10.1007/s00269-012-0551-7

Sinmyo, R., McCammon, C. & Dubrovinsky, L. (2017). The spin state of Fe^{3+} in lower mantle bridgmanite. *American Mineralogist*, *102*, (6), 1263-1269. https://doi.org/10.2138/am-2017-5917

Solomatova, N. V., Jackson, J. M., Sturhahn, W., Wicks, J. K., Zhao, J., Toellner, T. S., Kalkan, B. & Steinhardt, W. M. (2016). Equation of state and spin crossover of (Mg,Fe)O at high pressure, with implications for explaining topographic relief at the core-mantle boundary. *American Mineralogist*, *101*, (5), 1084-1093. https://doi.org/10.2138/am-2016-5510

Speziale, S., Milner, A., Lee, V. E., Clark, S. M., Pasternak, M. P. & Jeanloz, R. (2005). Iron spin transition in Earth's mantle. *Proceedings of the National Academy of Sciences*, *102*, (50), 17918-17922. https://doi.org/10.1073/pnas.0508919102

Speziale, S., Lee, V. E., Clark, S. M., Lin, J. F., Pasternak, M. P. & Jeanloz, R. (2007). Effects of Fe spin transition on the elasticity of (Mg, Fe)O magnesiowüstites and implications for the seismological properties of the Earth's lower mantle. *Journal of Geophysical Research*, *112*, B10212. https://doi.org/10.1029/2006jb004730

Stacey, F. D., Brennan, B. J. & Irvine, R. D. (1981). Finite strain theories and comparisons with seismological data. *Geophysical Surveys*, *4*, (3), 189-232. https://doi.org/10.1007/bf01449185

Stixrude, L. & Lithgow-Bertelloni, C. (2011). Thermodynamics of mantle minerals - II. Phase equilibria. *Geophysical Journal International*, *184*, (3), 1180-1213. https://doi.org/10.1111/j.1365-246x.2010.04890.x

Stixrude, L. & Lithgow-Bertelloni, C. (2022). Thermal expansivity, heat capacity and bulk modulus of the mantle. *Geophysical Journal International*, *228*, (2), 1119-1149. https://doi.org/https://doi.org/10.1093/gji/ggab394

Stixrude, L. & Lithgow-Bertelloni, C. (2024). Thermodynamics of mantle minerals – III: the role of iron. *Geophysical Journal International*, *237*, (3), 1699-1733. https://doi.org/10.1093/gji/ggae126

Sturhahn, W., Jackson, J. M. & Lin, J. F. (2005). The spin state of iron in minerals of Earth's lower mantle. *Geophysical Research Letters*, *32*, L12307. https://doi.org/10.1029/2005gl022802

Sun, T., Umemoto, K., Wu, Z., Zheng, J.-C. & Wentzcovitch, R. M. (2008). Lattice dynamics and thermal equation of state of platinum. *Physical Review B*, *78*, 024304. https://doi.org/10.1103/physrevb.78.024304

Sun, Y., Zhuang, J. & Wentzcovitch, R. M. (2022). Thermodynamics of spin crossover in ferropericlase: an improved LDA+U_{sc} calculation. *Electronic Structure*, *4*, 014008. https://doi.org/10.1088/2516-1075/ac522b

Takemura, K. (2021). Hydrostaticity in high pressure experiments: some general observations and guidelines for high pressure experimenters. *High Pressure Research*, *41*, (2), 155-174. https://doi.org/10.1080/08957959.2021.1903457

Tange, Y., Nishihara, Y. & Tsuchiya, T. (2009). Unified analyses for *P-V-T* equation of state of MgO: A solution for pressure-scale problems in high *P-T* experiments. *Journal of Geophysical Research: Solid Earth*, *114*, B03208. https://doi.org/10.1029/2008jb005813

Tange, Y., Kuwayama, Y., Irifune, T., Funakoshi, K. I. & Ohishi, Y. (2012). *P-V-T* equation of state of $MgSiO_3$ perovskite based on the MgO pressure scale: A comprehensive reference for mineralogy of the lower mantle. *Journal of Geophysical Research: Solid Earth*, *117*, B06201. https://doi.org/10.1029/2011jb008988

Thielmann, M., Golabek, G. J. & Marquardt, H. (2020). Ferropericlase Control of Lower Mantle Rheology: Impact of Phase Morphology. *Geochemistry, Geophysics, Geosystems*, *21*, e2019GC008688. https://doi.org/10.1029/2019GC008688

Toby, B. H. & Von Dreele, R. B. (2013). *GSAS-II*: the genesis of a modern open-source all purpose crystallography software package. *Journal of Applied Crystallography*, *46*, (2), 544-549. https://doi.org/10.1107/s0021889813003531

Trautner, V. E., Stackhouse, S., Turner, A. R., Koelemeijer, P., Davies, D. R., Méndez, A. S. J., Satta, N., Kurnosov, A., Liermann, H.-P. & Marquardt, H. (2023). Compressibility of ferropericlase at high-temperature: Evidence for the iron spin crossover in seismic tomography. *Earth and Planetary Science Letters*, *618*, 118296. https://doi.org/10.1016/j.epsl.2023.118296

Trautner, V. E., Rijal, A., Plueckthun, C., Satta, N., Koemets, E., Buchen, J., Wang, B., Glazyrin, K., Cobden, L. & Marquardt, H. (2024). Iron Content-Dependence of Ferropericlase Elastic Properties Across the Spin Crossover From Novel Experiments and Machine Learning. *Geophysical Research Letters*, *51*, (22), e2024GL111276. https://doi.org/10.1029/2024gl111276

Tschauner, O., Ma, C., Beckett, J. R., Prescher, C., Prakapenka, V. B. & Rossman, G. R. (2014). Discovery of bridgmanite, the most abundant mineral in Earth, in a shocked meteorite. *Science*, *346*, (6213), 1100-1102. https://doi.org/10.1126/science.1259369

Tsuchiya, T., Wentzcovitch, R. M., Da Silva, C. R. S. & De Gironcoli, S. (2006). Spin Transition in Magnesiowüstite in Earth's Lower Mantle. *Physical Review Letters*, *96*, 198501. https://doi.org/10.1103/physrevlett.96.198501

Umemoto, K., Wentzcovitch, R. M., Yu, Y. G. & Requist, R. (2008). Spin transition in (Mg,Fe)SiO_3 perovskite under pressure. *Earth and Planetary Science Letters*, *276*, (1-2), 198-206. https://doi.org/10.1016/j.epsl.2008.09.025

Uts, I., Glazyrin, K. & Lee, K. K. M. (2013). Effect of laser annealing of pressure gradients in a diamond-anvil cell using common solid pressure media. *Review of Scientific Instruments*, *84*, 103904. https://doi.org/10.1063/1.4821620

Valencia-Cardona, J. J., Shukla, G., Wu, Z., Houser, C., Yuen, D. A. & Wentzcovitch, R. M. (2017). Influence of the iron spin crossover in ferropericlase on the lower mantle geotherm. *Geophysical Research Letters*, *44*, (10), 4863-4871. https://doi.org/10.1002/2017gl073294

Voigt, W. (1928). *Lehrbuch der Kristallphysik*. Leibzig: Teubner.

Walter, M. J., Thomson, A. R. & Smith, E. M. (2022). Geochemistry of silicate and oxide inclusions in sublithospheric diamonds. *Reviews in Mineralogy and Geochemistry*, *88*, (1), 393-450. https://doi.org/10.2138/rmg.2022.88.07

Wang, B. (2022). Batch Peaks Fitting Script in Python for Time-Resolved XRD Data Analysis (v1.0.0) [Software]. Zenodo. https://doi.org/10.5281/zenodo.7457445

Wang, X., Tsuchiya, T. & Hase, A. (2015). Computational support for a pyrolitic lower mantle containing ferric iron. *Nature Geoscience*, *8*, (7), 556-559. https://doi.org/10.1038/ngeo2458

Waszek, L., Schmerr, N. C. & Ballmer, M. D. (2018). Global observations of reflectors in the mid-mantle with implications for mantle structure and dynamics. *Nature Communications*, *9*, 385. https://doi.org/10.1038/s41467-017-02709-4

Watt, J. P., Davies, G. F. & O'Connell, R. J. (1976). The elastic properties of composite materials. *Reviews of Geophysics*, *14*, (4), 541-563. https://doi.org/10.1029/RG014i004p00541

Waychunas, G. A., Dollase, W. A. & Ross II, C. R. (1994). Short-range order measurements in MgO-FeO and MgO-$LiFeO_2$, solid solutions byDLS simulation-assisted EXAFS analysis. *American Mineralogist*, *79*, (3-4), 274-288.

Wentzcovitch, R. M., Justo, J. F., Wu, Z., Da Silva, C. R. S., Yuen, D. A. & Kohlstedt, D. (2009). Anomalous compressibility of ferropericlase throughout the iron spin cross-over. *Proceedings of the National Academy of Sciences*, *106*, (21), 8447-8452. https://doi.org/10.1073/pnas.0812150106

Westrenen, W. v., Li, J., Fei, Y., Frank, M. R., Hellwig, H., Komabayashi, T., Mibe, K., Minarik, W. G., Orman, J. A. V., Watson, H. C., Funakoshi, K.-i. & Schmidt, M. W. (2005). Thermoelastic properties of $(Mg_{0.64}Fe_{0.36})O$ ferropericlase based on in situ X-ray diffraction to 26.7GPa and 2173K. *Physics of the Earth and Planetary Interiors*, *151*, (1-2), 163-176. https://doi.org/10.1016/j.pepi.2005.03.001

Wicks, J. K., Jackson, J. M. & Sturhahn, W. (2010). Very low sound velocities in iron-rich (Mg,Fe)O: Implications for the core-mantle boundary region. *Geophysical Research Letters*, *37*, L15304. https://doi.org/10.1029/2010gl043689

Wicks, J. K., Jackson, J. M., Sturhahn, W. & Zhang, D. (2017). Sound velocity and density of magnesiowüstites: Implications for ultralow-velocity zone topography. *Geophysical Research Letters*, *44*, 2148-2158. https://doi.org/10.1002/2016gl071225

Wolf, A. S., Jackson, J. M., Dera, P. & Prakapenka, V. B. (2015). The thermal equation of state of (Mg, Fe)SiO_3 bridgmanite (perovskite) and implications for lower mantle structures. *Journal of Geophysical Research: Solid Earth*, *120*, (11), 7460-7489. https://doi.org/10.1002/2015jb012108

Wu, X., Wu, Y., Lin, J. F., Liu, J., Mao, Z., Guo, X., Yoshino, T., Mccammon, C., Prakapenka, V. B. & Xiao, Y. (2016). Two-stage spin transition of iron in FeAl-bearing phase D at lower mantle. *Journal of Geophysical Research: Solid Earth*, *121*, (9), 6411-6420. https://doi.org/10.1002/2016jb013209

Wu, Z., Justo, J. F. & Wentzcovitch, R. M. (2013). Elastic anomalies in a spin-crossover system: ferropericlase at lower mantle conditions. *Physical Review Letters*, *110*, 228501. https://doi.org/10.1103/PhysRevLett.110.228501

Wu, Z. & Wentzcovitch, R. M. (2014). Spin crossover in ferropericlase and velocity heterogeneities in the lower mantle. *Proceedings of the National Academy of Sciences*, *111*, (29), 10468-10472. https://doi.org/10.1073/pnas.1322427111

Wu, Z. (2016). Velocity structure and composition of the lower mantle with spin crossover in ferropericlase. *Journal of Geophysical Research: Solid Earth*, *121*, (4), 2304-2314. https://doi.org/10.1002/2015jb012667

Xu, S., Lin, J. F. & Morgan, D. (2017). Iron partitioning between ferropericlase and bridgmanite in the Earth's lower mantle. *Journal of Geophysical Research: Solid Earth*, *122*, (2), 1074-1087. https://doi.org/10.1002/2016jb013543

Xu, W., Lithgow-Bertelloni, C., Stixrude, L. & Ritsema, J. (2008). The effect of bulk composition and temperature on mantle seismic structure. *Earth and Planetary Science Letters*, *275*, (1), 70-79. https://doi.org/10.1016/j.epsl.2008.08.012

Yang, J., Tong, X., Lin, J.-F., Okuchi, T. & Tomioka, N. (2015). Elasticity of Ferropericlase across the Spin Crossover in the Earth's Lower Mantle. *Scientific Reports*, *5*, 17188. https://doi.org/10.1038/srep17188

Yang, J., Lin, J. F., Jacobsen, S. D., Seymour, N. M., Tkachev, S. N. & Prakapenka, V. B. (2016). Elasticity of ferropericlase and seismic heterogeneity in the Earth's lower mantle. *Journal of Geophysical Research: Solid Earth*, *121*, 8488-8500. https://doi.org/10.1002/2016jb013352

Yang, K., Wang, X., Zhang, J., Cheng, Y., Zhang, C., Zeng, Z. & Lin, H. (2021). Entropic broadening of the spin-crossover pressure in ferropericlase. *Physical Review B*, *103*, 224105. https://doi.org/10.1103/physrevb.103.224105

Yen, C. E., Williams, Q. & Kunz, M. (2020). Thermal Pressure in the Laser-Heated Diamond Anvil Cell: A Quantitative Study and Implications for the Density Versus Mineralogy Correlation of the Mantle. *Journal of Geophysical Research: Solid Earth*, *125*, (10), e2020JB020006. https://doi.org/10.1029/2020jb020006

Yu, S. & Garnero, E. J. (2018). Ultralow Velocity Zone Locations: A Global Assessment. *Geochemistry, Geophysics, Geosystems*, *19*, (2), 396-414. https://doi.org/10.1002/2017GC007281

Zhang, J. & Kostak, P. (2002). Thermal equation of state of magnesiowüstite $(Mg_{0.6}Fe_{0.4})O$. *Physics of the Earth and Planetary Interiors*, *129*, (3), 301-311. https://doi.org/10.1016/S0031-9201(01)00296-5

Zhang, S., Cottaar, S., Liu, T., Stackhouse, S. & Militzer, B. (2016). High-pressure, temperature elasticity of Fe- and Al-bearing $MgSiO_3$: Implications for the Earth's lower mantle. *Earth and Planetary Science Letters*, *434*, 264-273. https://doi.org/10.1016/j.epsl.2015.11.030

Zhu, F., Liu, J., Lai, X., Xiao, Y., Prakapenka, V., Bi, W., Alp, E. E., Dera, P., Chen, B. & Li, J. (2020). Synthesis, Elasticity, and Spin State of an Intermediate $MgSiO_3$-$FeAlO_3$ Bridgmanite: Implications for Iron in Earth's Lower Mantle. *Journal of Geophysical Research: Solid Earth*, *125*, (7), e2020JB019964. https://doi.org/10.1029/2020jb019964

Zhuravlev, K. K., Jackson, J. M., Wolf, A. S., Wicks, J. K., Yan, J. & Clark, S. M. (2010). Isothermal compression behavior of (Mg,Fe)O using neon as a pressure medium. *Physics and Chemistry of Minerals*, *37*, (7), 465-474. https://doi.org/10.1007/s00269-009-0347-6

Appendix A. Supplemental information for Chapter 2

A.1. Line-width analysis to determine non-hydrostaticity

To evaluate the stress condition of our high-temperature experiments, which did not have a pressure-transmitting medium, we obtained the product of elastic anisotropy factor (S) and uniaxial stress component (t) from a line-shift analysis of the utilized reflections (Singh & Takemura, 2001). To calculate deviatoric stress in a sample, S of the material and its dependence on temperature and pressure must be well-constrained, which is currently not the case for platinum and $(Mg_{0.8}Fe_{0.2})O$ at our experimental conditions. Notwithstanding, the product St can be used as an indicator of the magnitude of uniaxial stress, with Shim et al. (2000) proposing a St value between -0.005 and 0.005 as a criterion for quasi-hydrostaticity. Most of our measurements yield St values between approximately -0.01 and 0.01 for both platinum and ferropericlase (fig. A.1), exceeding the limit of $|St| \leq 0.005$. This indicates non-hydrostatic stresses of moderate magnitude were present during some of the measurements. The ramp measured in cell RH2 at 1100 K forms an exception, with St values of -0.016 in ferropericlase, indicating a high differential stress. Because the volumes derived from the $(111)_{Fp}$ and $(220)_{Fp}$ reflections are closest to the volumes measured during the pressure oscillation experiments at the same temperature with lower St values of around -0.006, we chose to use these reflections only for the ramp at 1100 K.

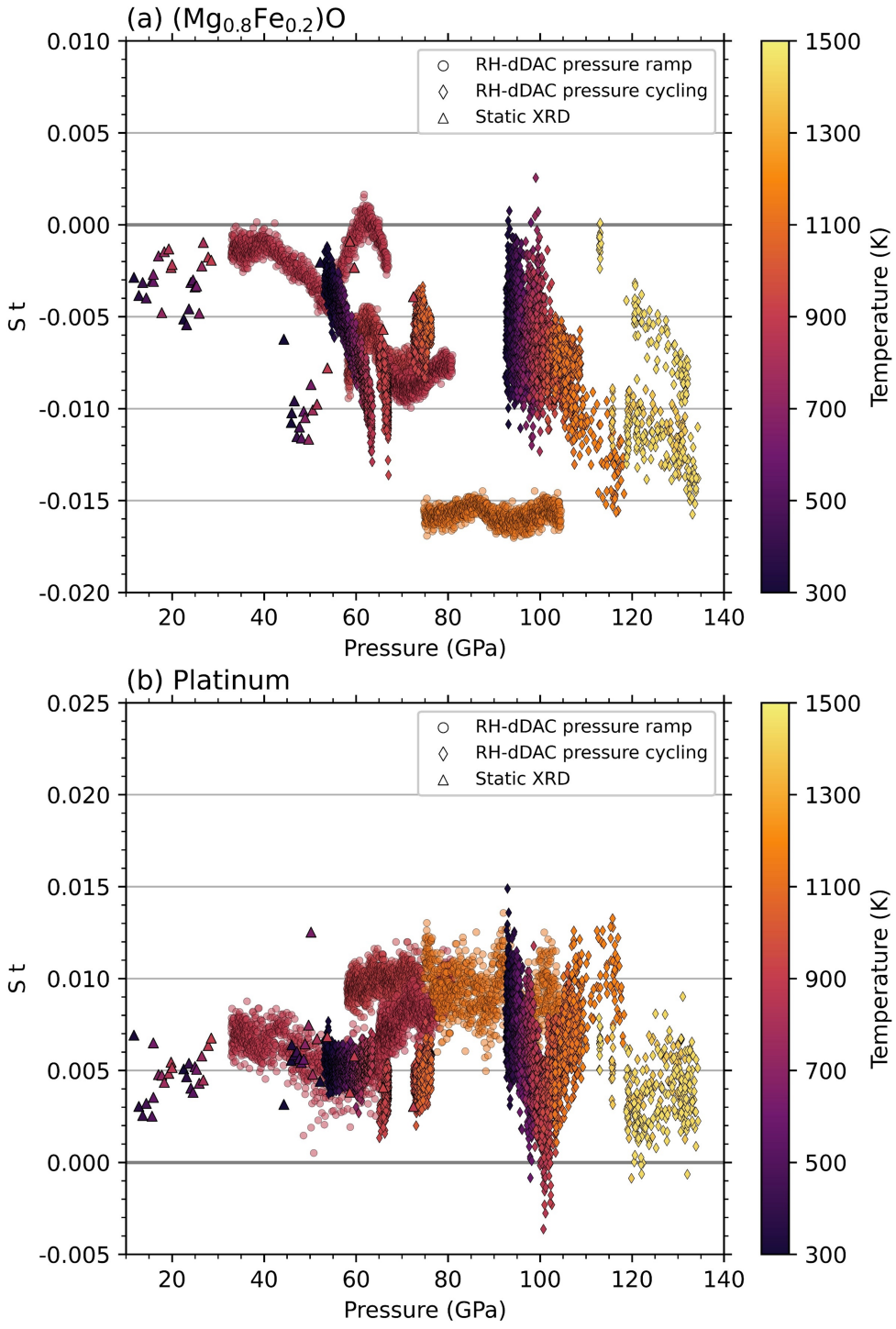

Figure A.1 Product of elastic anisotropy *S* and uniaxial stress component *t* as a function of pressure for (a) ferropericlase, and (b) platinum, obtained from a line-shift analysis of the all data collected in the RH-dDAC. *St* values can be used as an indicator of the magnitude of deviatoric stress.

A.2. Supporting figures

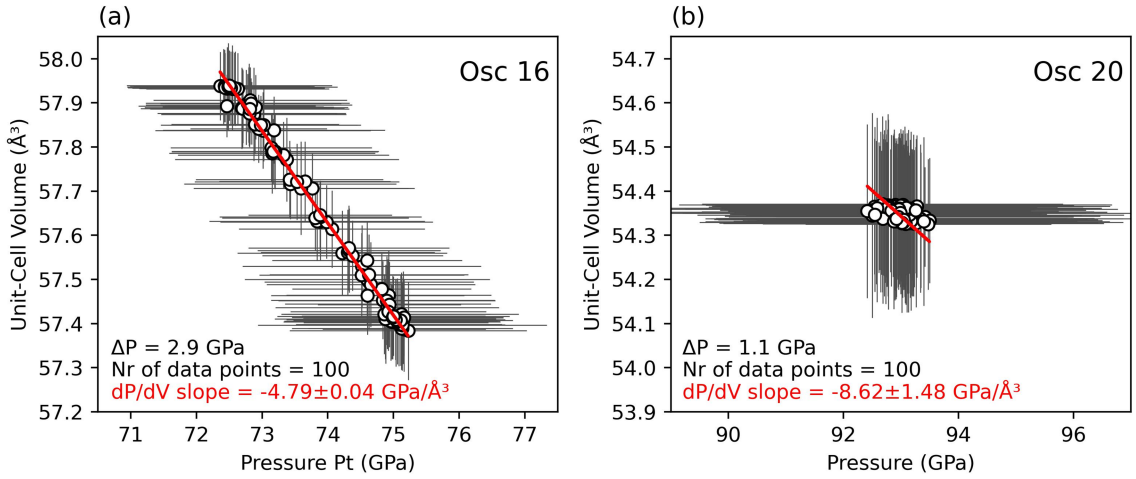

Figure A.2 Unit-cell volume of ferropericlase as a function of pressure for data points from oscillations experiments in a) RH1, and b) RH2. A linear regression line to the data is shown in red. For the oscillation experiment in RH2, the pressure range over which pressure was cycled is smaller than the uncertainties in the pressure determination, resulting in a large error in the slope of the regression line. Consequently, no reliable bulk modulus value could be extracted from these data.

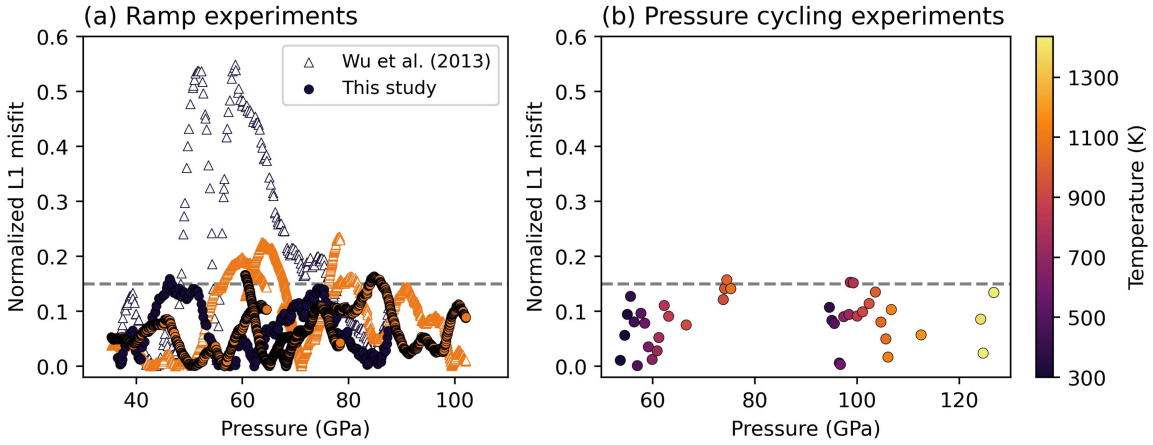

Figure A.3 L1 misfit between the experimental and theoretical bulk moduli, normalised with the experimental value. a) Misfit between the experimental ramps and the computations from Wu et al. (2013) (open triangles) and the computational results from this study (filled circles). b) Misfit between the bulk modulus values derived from pressure cycling experiments and the computational results from this study. The misfit with the new computations from this study for both ramp and pressure cycling experiments is not more than 0.15 (dashed grey line) at any pressure.

Appendix B. Supplemental information for Chapter 3

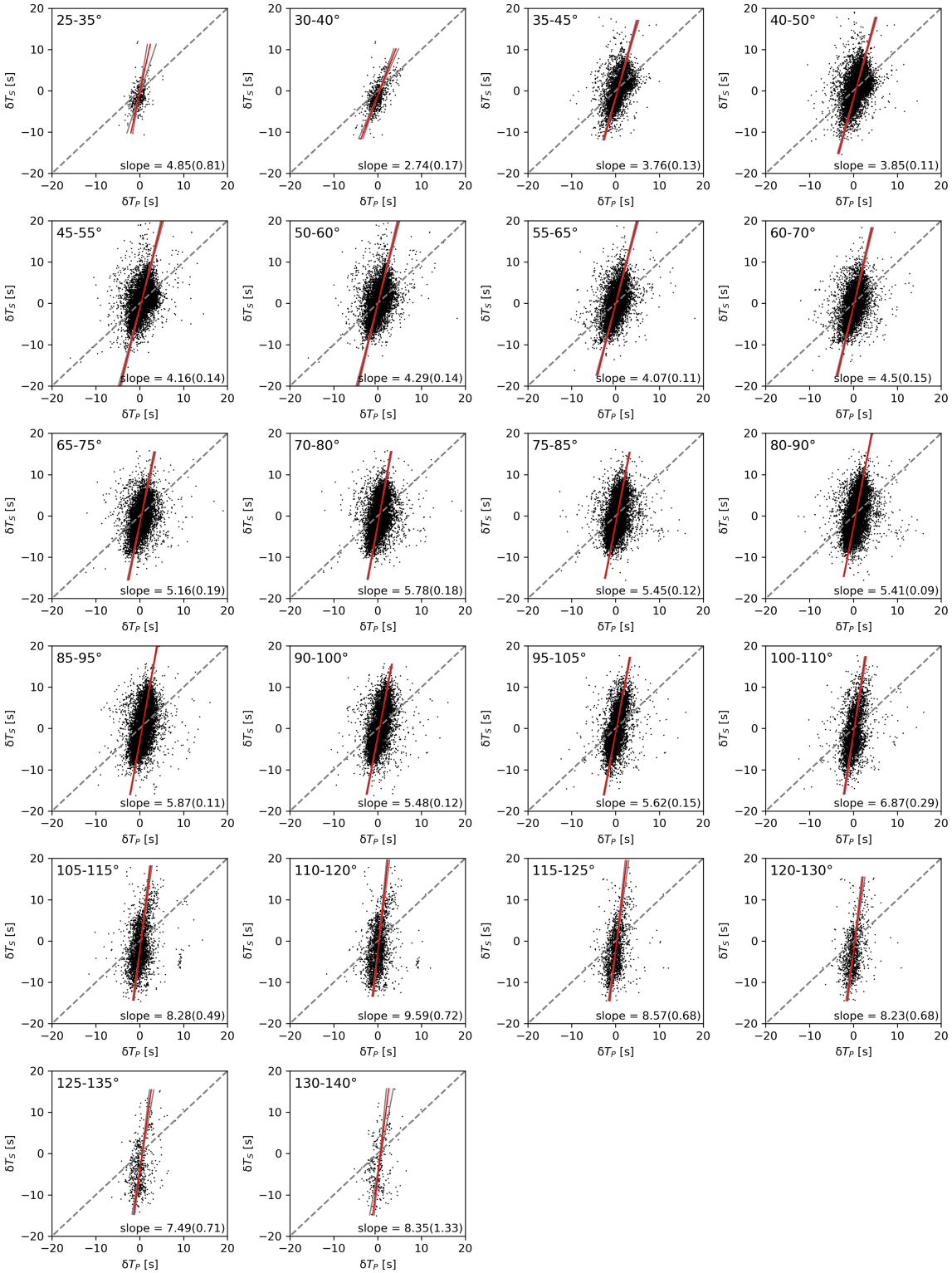

Figure B.1 Travel-time anomalies of direct P- and S-waves (δT_S versus δT_P) for common source-receiver pairs in 10° epicentral distance bins, with best-fitting lines (red), determined by PCA. The solid grey lines show the uncertainty in the slopes of the best-fitting lines (two standard deviations), determined with a boot-strapping routine.

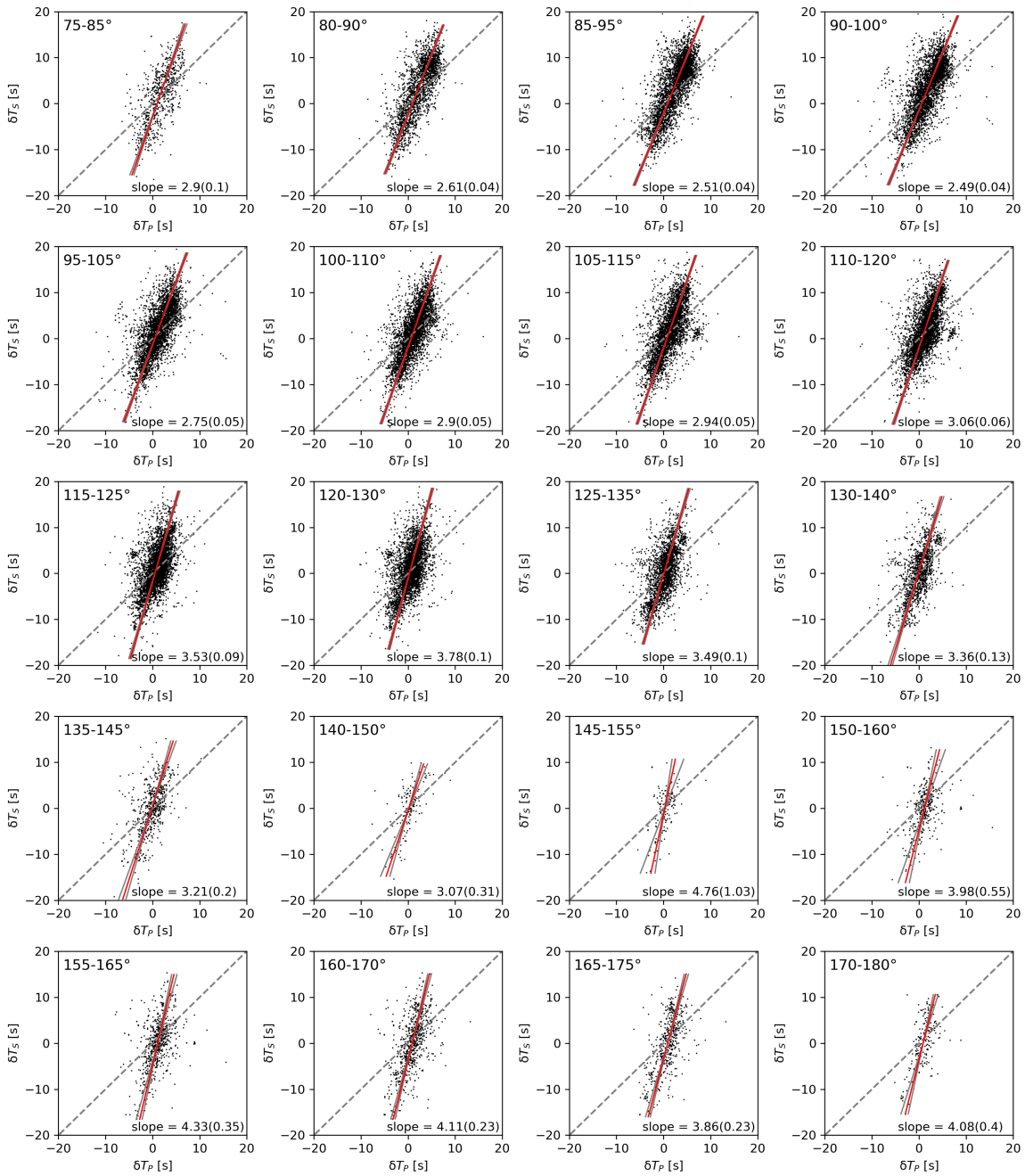

Figure B.2 Travel-time anomalies of surface-reflected P- and S-waves (δT_{SS} versus δT_{PP}) for common source-receiver pairs in 10° epicentral distance bins, with best-fitting lines (red), determined by PCA (red). The solid grey lines show the uncertainty in the slopes of the best-fitting lines (two standard deviations), determined with a boot-strapping routine.

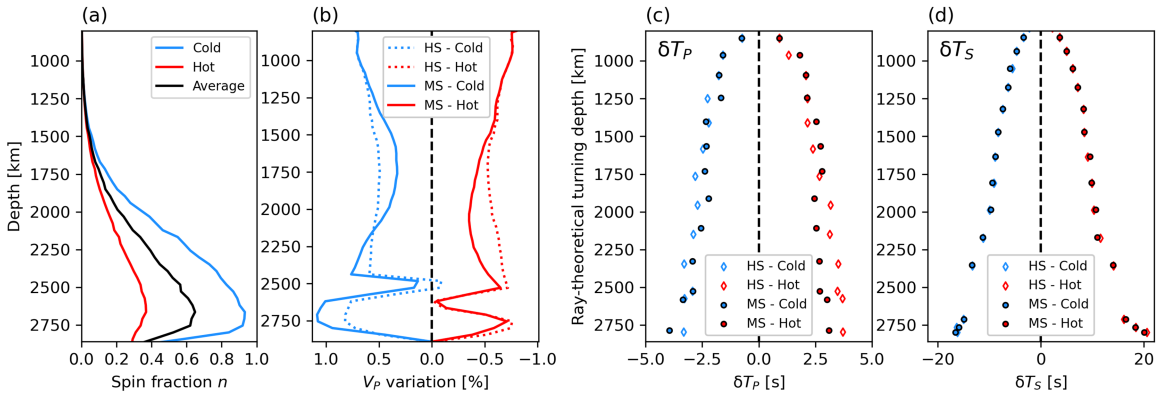

Figure B.3 Effect of temperature on the signal of the spin crossover in seismic travel-times. (a) Low spin fraction n as a function of depth for the cold, hot and average temperature profiles (from Trautner et al., 2023). (b) Variations in V_P for cold (blue) and hot (red) velocity profiles with respect to the average geotherm, for MS (solid line) and HS (dotted line) models with post-perovskite. (c,d) P and S travel-time anomalies for the cold (blue) and hot (red) models with respect to the average geotherm model, as a function of ray-theoretical turning depth. Results are shown for MS models (filled circles) and HS models (open diamonds) with post-perovskite.

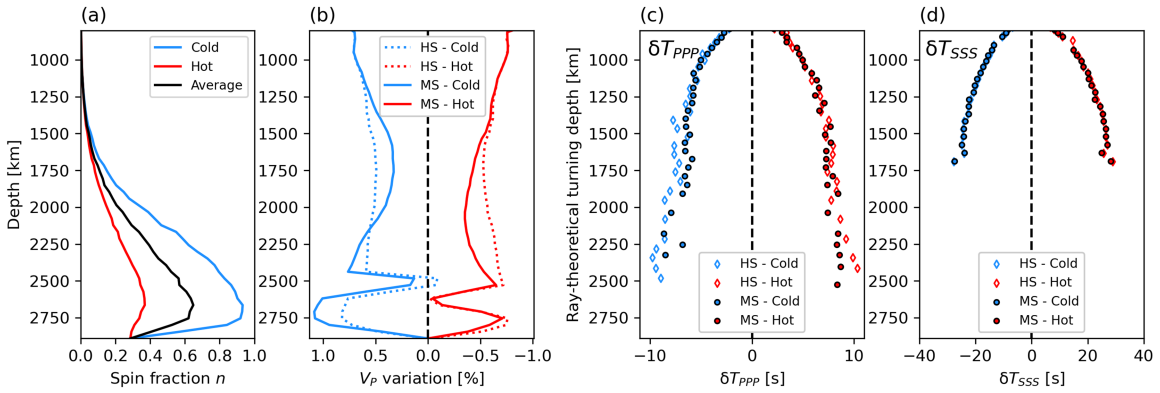

Figure B.4 Effect of temperature on the signal of the spin crossover in seismic travel-times. (a) Low spin fraction n as a function of depth for the cold, hot and average temperature profiles (from Trautner et al., 2023). (b) Variations in V_P for cold (blue) and hot (red) velocity profiles with respect to the average geotherm, for MS (solid line) and HS (dotted line) models with post-perovskite. (c,d) *PPP* and *SSS* travel-time anomalies for the cold (blue) and hot (red) models with respect to the average geotherm model, as a function of ray-theoretical turning depth. Results are shown for MS models (filled circles) and HS models (open diamonds) with post-perovskite.

Appendix C. Supplemental information for Chapter 4

C.1. Sample synthesis and characterization

Two samples of $(Mg_{1-x}Fe_x)O$ with $x_{Fe} = 0.40$ and $x_{Fe} = 0.59$ were synthesized from stoichiometric mixtures of MgO and Fe_2O_3. For the synthesis of the Fp40 sample a similar procedure as reported by Longo et al. (2011) was followed. The starting materials were first dissolved in HNO_3 under a constant flux of nitrogen gas, while cooling in an ice-bath to prevent oxidation. Next, NH_4OH was added to precipitate fine-grained oxide powders, before removing excess HNO_3 and NH_4OH from the obtained gels using a Bunsen burner. The starting materials of the Fp59 sample were simply ground in a zirconium mortar (94.7% ZrO_2 + 5.3% Yr_2O_3). The stoichiometric mixtures were pressed into pellets and equilibrated in a gas-mixing furnace under CO_2/CO at 1300 °C, where the Fp40 and Fp59 samples were treated for a duration of approximately 23 and 48 hours at $\log(f_{O2}) = -9.6$ and -9.7, respectively. After recovery from the gas-mixing furnace, the polycrystalline samples were reground to a fine powder and characterized using Mössbauer spectroscopy, X-ray powder diffraction (XRD) and electron microprobe analysis. Mössbauer spectroscopy measurements were conducted at Bayerisches Geoinstitut, Bayreuth, Germany (McCammon, 1994) to identify any remnant Fe^{3+} and magnetic components in the samples. Mössbauer spectra were collected for velocities of ± 12 mm/s at room temperature, using a constant acceleration Mössbauer spectrometer with a 50 MCi ^{57}Co radiation source in a 6 μm Re matrix. Fitting of the spectra with MossA (Prescher et al., 2012) indicated that over 90% of the iron in both samples was present as Fe^{2+} (92.9 ± 2.1% and 91.2 ± 1.5% in Fp40 and Fp59, respectively) and no remnant magnetic phases could be observed. X-ray diffraction measurements at beamline P02.2 at PETRAIII, DESY, Germany confirmed the face-centered cubic structure of the samples at ambient conditions, with a zero-pressure volume (V_0) of 77.08 ± 0.03 Å^3 for Fp40 and 77.88 ± 0.06 Å^3 for Fp59. Analysis using a Cameca SX-5 FE electron microprobe at the Department of Earth Sciences, University of Oxford, United Kingdom revealed that the samples were chemically homogeneous at the length scale investigated, with compositions of $(Mg_{0.604(4)}Fe_{0.396(4)})O$ and $(Mg_{0.409(4)}Fe_{0.591(4)})O$ where the numbers in parentheses indicate the uncertainties in the last digit of atomic weight.

C.2. Effect of cubic-rhombohedral distortion on unit-cell volumes

To investigate the effect of the rhombohedral distortion on the unit-cell volume of the ferropericlase samples, the XRD patterns of run #3 and #5 (table 4.1) were fitted with a rhombohedral structure using Le Bail refinement in TOPAS (Coelho, 2018) at pressures above 30 GPa. We then normalized the rhombohedral unit-cell volume to the number of atoms in a unit-cell of (Mg,Fe)O in the cubic B1 space group (i.e., 8 atoms) to allow for comparison with the cubic unit-cell volume calculated from the individually fitted diffraction peaks. The difference between the rhombohedral and cubic unit-cell volumes is small compared to the uncertainties in pressure and volume (fig. C.1). The effect of the rhombohedral distortion is expected to be largest in run #5 because the sample had a high iron content, it was compressed to very high pressures and neon was used as a PTM, which should lead to larger deviatoric stresses compared to helium (Finkelstein et al., 2017), but we find that the effect on the unit-cell volume is negligible. Therefore, we decided it was acceptable to use the volumes for a cubic unit-cell calculated from the peak positions provided by the Python code (Wang, 2022), as refinement of time-resolved XRD data with TOPAS or other available crystallography softwares is very time consuming.

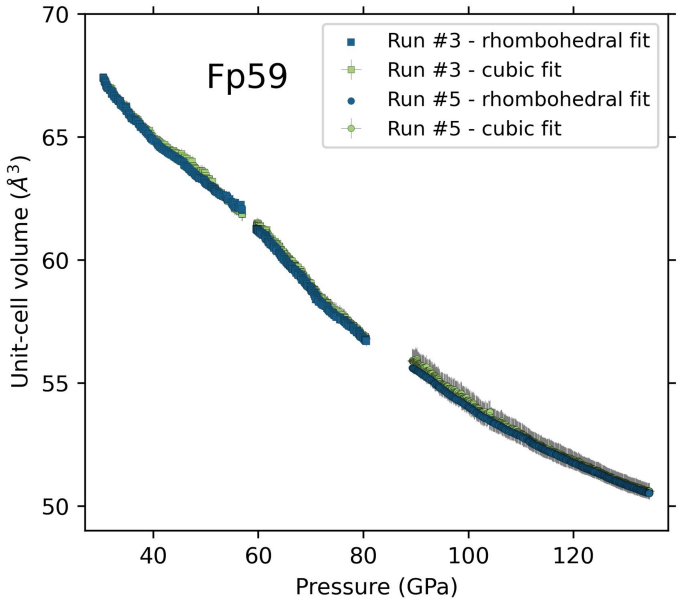

Figure C.1 Unit-cell volume as a function of pressure for runs #3 and #5 on Fp59, determined from fitting the XRD patterns with a cubic structure (green symbols) and a rhombohedral structure (blue symbols). The difference is smaller than the uncertainties.

C.3. Training of Mixture Density Networks and creation of training data set

In a Mixture Density Network, a conventional feed-forward neural network is combined with a Gaussian mixture model to find the posterior pdf at a given pressure and iron content (fig. C.2).

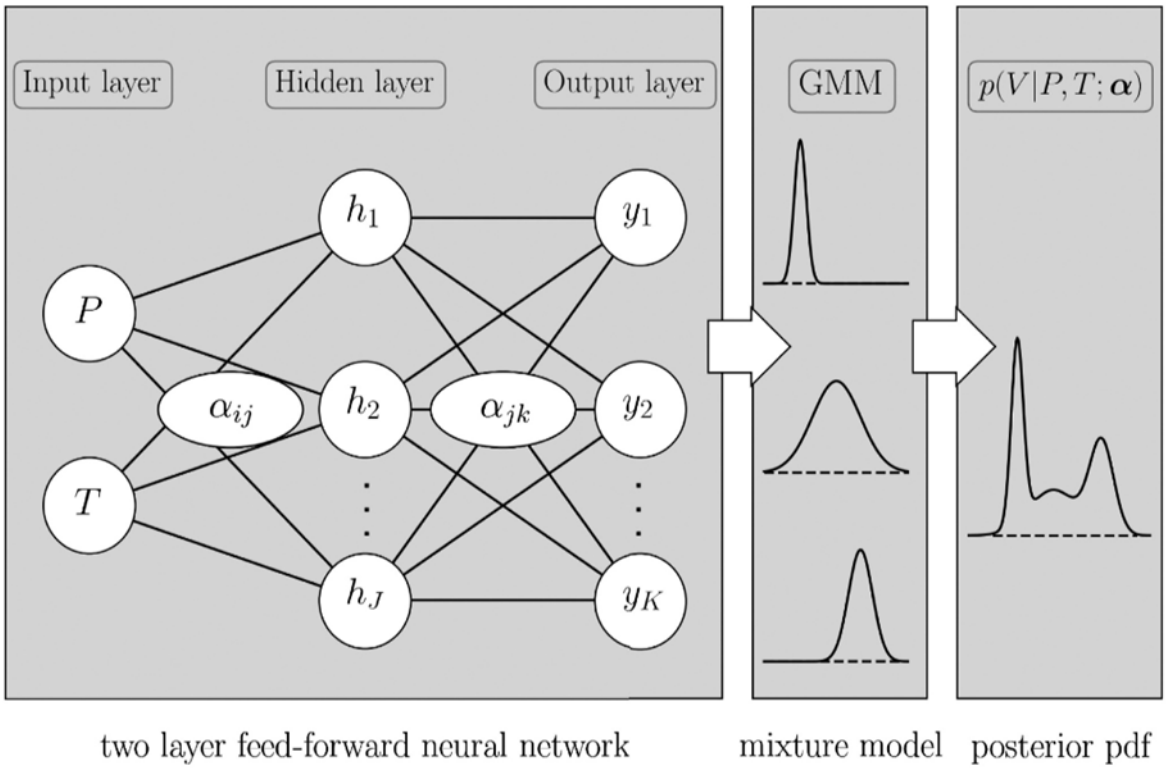

Figure C.2 Schematic representation of the architecture of a Mixture Density Network. A two-layer feed-forward neural network is combined with a Gaussian Mixture Model (GMM) to predict the posterior probability density function (pdf). *P* and *T* denote the network inputs (in this study these are pressure and iron content), *h* denotes the hidden nodes, *α* denotes weights and *y* denotes the outputs of the feed-forward network. These outputs are related to the mean, standard deviation and weight of each Gaussian kernel in the GMM. The final posterior pdf is produced by weighting each Gaussian. Figure from Rijal et al. (2021).

A test was performed to find the optimal network complexity that balances the ability of the MDN to capture complex trends in the data and the unwanted memorization of noise or errors particular to the training data set. A number of hidden nodes between 80 and 120 was found to produce the lowest monitoring errors (fig. C.3). For the training of all 10^3 MDNs the number of hidden nodes was randomly drawn from this range, while the number of Gaussian kernels used was 3-5. Because of the complicated dependency of ferropericlase material properties on pressure in the spin crossover region, the MDNs were trained using a mini-batch approach, where the training data is fed to the network in small chunks of 512 datapoints and the network parameters are updated iteratively (Rijal, 2023). This approach improves the generalization performance as measured by the error on the test set by adding noise to the learning process, which helps to escape local minima and saddle points.

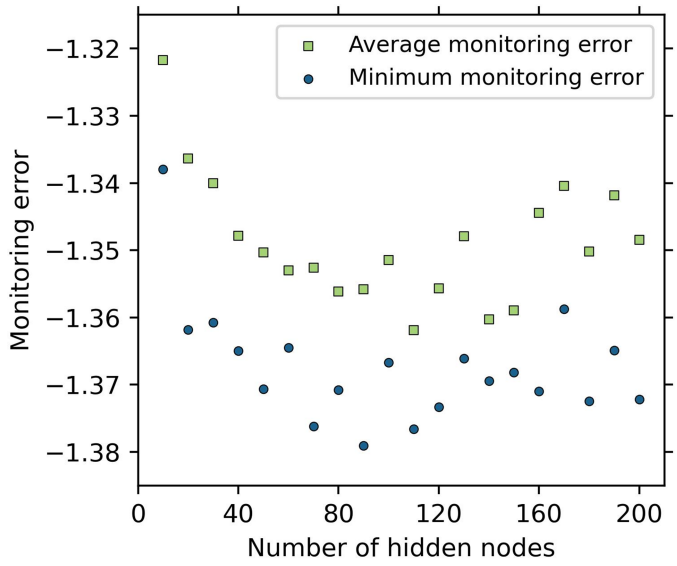

Figure C.3 Monitoring error as a function of the number of hidden nodes. For each number of hidden nodes 10 independent MDNs were trained and the average monitoring errors (green cubes) as well as the lowest value for each set of networks (blue circles) were determined. The minimum value in both curves can be used to derive the upper and lower bounds for the preferred range from which the number of hidden nodes to use in the training of the MDNs is randomly drawn.

The number of datapoints collected in time-resolved compression experiments as presented in this study and in Méndez et al. (2022) is one to two orders of magnitude larger than those measured in conventional compression experiments (table 4.2). To prevent a bias towards these data sets in the pdfs predicted by the MDNs we reduce the number of datapoints by sorting the data of each compression run into bins of 1 GPa and extracting the average pressure and unit-cell volume of the data in each bin. The resulting training data set (fig. C.4) consists of about 1300 individual datapoints.

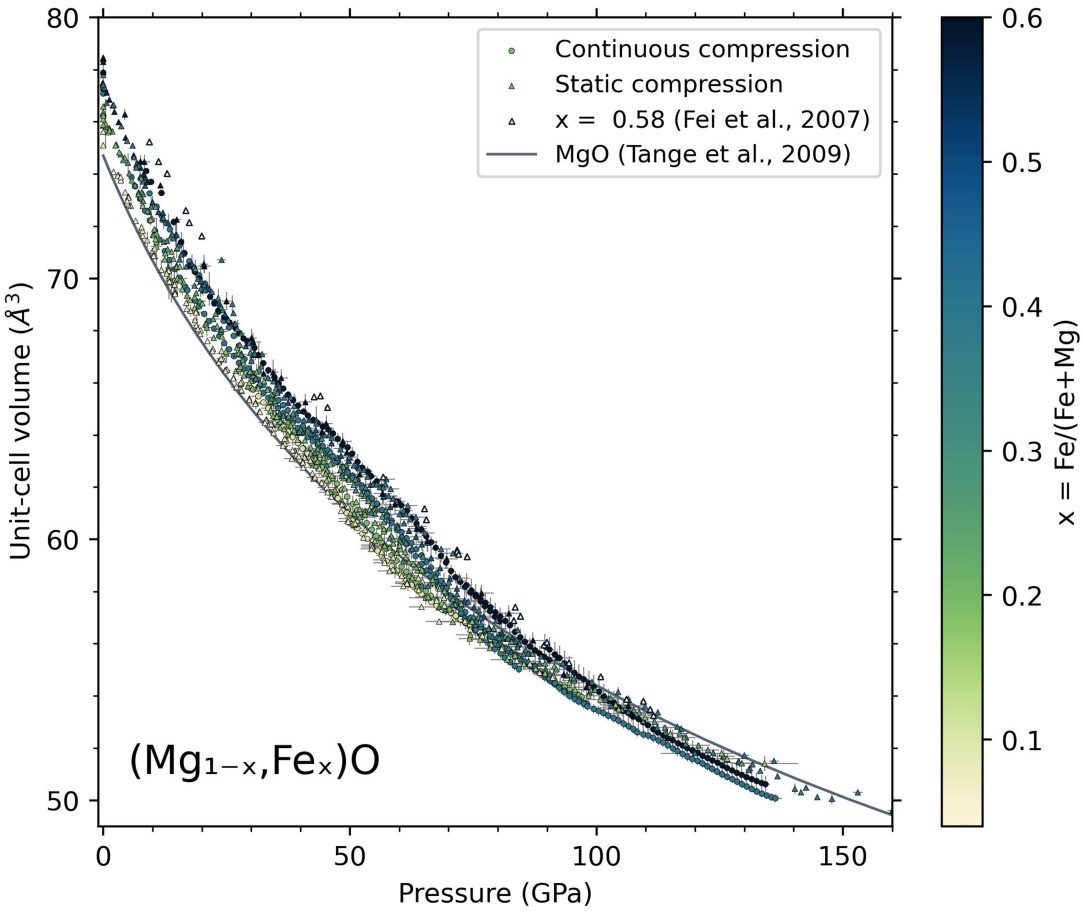

Figure C.4 Experimental *P-V-X*$_{Fe}$ data on ($Mg_{1-x}Fe_x$)O, including data from this study, used as input to train the MDNs (see table 4.2 for references). The number of datapoints from time-resolved continuous compression experiments (filled circles, Méndez et al. (2022) and this study) was reduced through a down-sampling procedure to prevent a bias of the MDN output towards these data sets due to their significantly larger size compared to other compression data (filled triangles). The equation of state for MgO (Tange et al., 2009) is shown as a solid grey line. Data for x_{Fe} = 0.58 from Fei et al. (2007b) (open triangles) below the spin crossover is shifted to significantly higher volumes compared to other results for similar compositions.

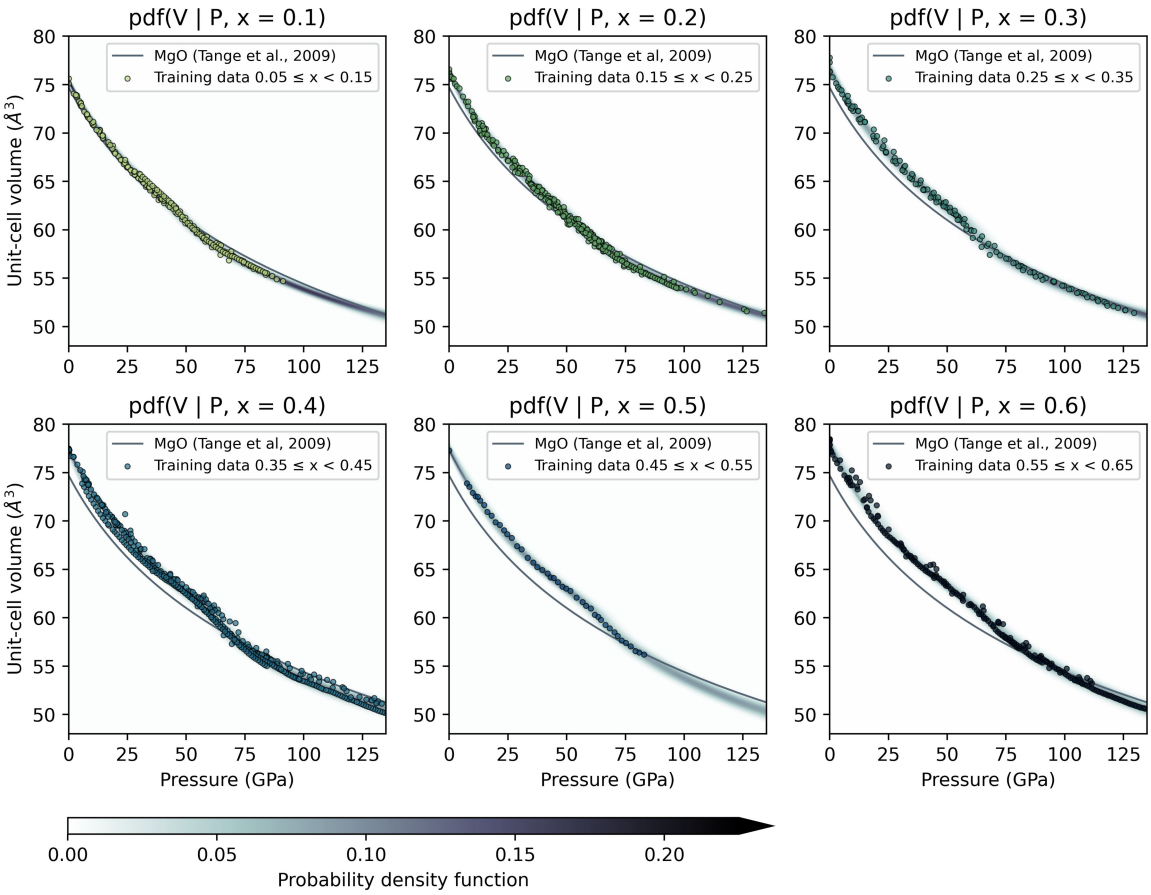

Figure C.5 Pdfs for the unit-cell volume of $(Mg_{1-x}Fe_x)O$ as a function of pressure predicted by MDNs for different iron contents. The MDNs were trained using experimental high-pressure data with x_{Fe} = 0.04-0.6. The colour scale corresponds to the value of the pdfs and the EoS of MgO (Tange et al., 2009) is shown as a grey line for reference. Coloured circles show the data used to train the MDNs, binned by iron content.

Appendix D. Supplemental information for Chapter 5

D.1. Pressure calculation and estimation of uncertainties

To determine the pressure of the sample in cell RT1 during the collection of diffraction images, a simple average of the pressure determined from platinum before and after measurement of the sample was taken (i.e. steps 3 and 5 of measurement protocol P1, see section 5.2.2). The uncertainty in pressure was estimated from the difference between the two pressure measurements and the average uncertainty of the measurements, propagated from the uncertainty in the unit-cell volumes of platinum.

Pressure for the measurements of the annealed sample in cell LH1 was determined from the pressure from platinum measured just before or just after the diffraction image of the sample was taken (i.e. step 3 for the image taken in step 4 and step 8 for the image taken in step 7 of protocol P2, see section 5.2.2). The pressures in cell LH1 determined from KCl in the diffraction images of the sample and the images of platinum differ by up to 13 GPa, with the pressure from platinum falling in between these values (fig. D.1). The uncertainty in pressure is therefore estimated from the difference between the pressures from KCl, which is much larger than the uncertainties in the pressures determined from platinum.

To estimate the pressure of the sample during the measurements at high-temperature, a simple average of the pressures determined from platinum before and after heating was calculated (i.e. steps 3 and 8 of protocol P2, see section 5.2.2), but with the inclusion of the thermal pressure term (see section 5.2.3). Like for the measurements at room temperature, uncertainties were estimated from the difference in the pressures determined from KCl.

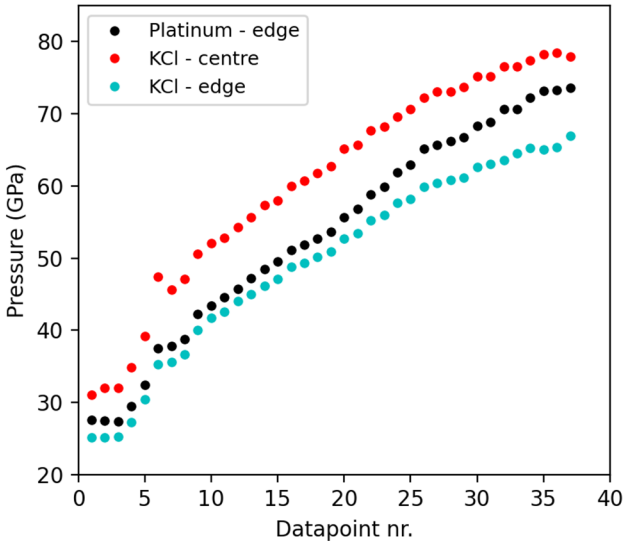

Figure D.1 Pressures calculated from the unit-cell volumes of platinum and KCl, measured during compression of cell LH1. Black and blue circles indicate platinum and KCl measured simultaneously at the edge of the sample chamber. Red circles show KCl measured with the sample near the centre of the sample chamber.

D.2. Supporting figures

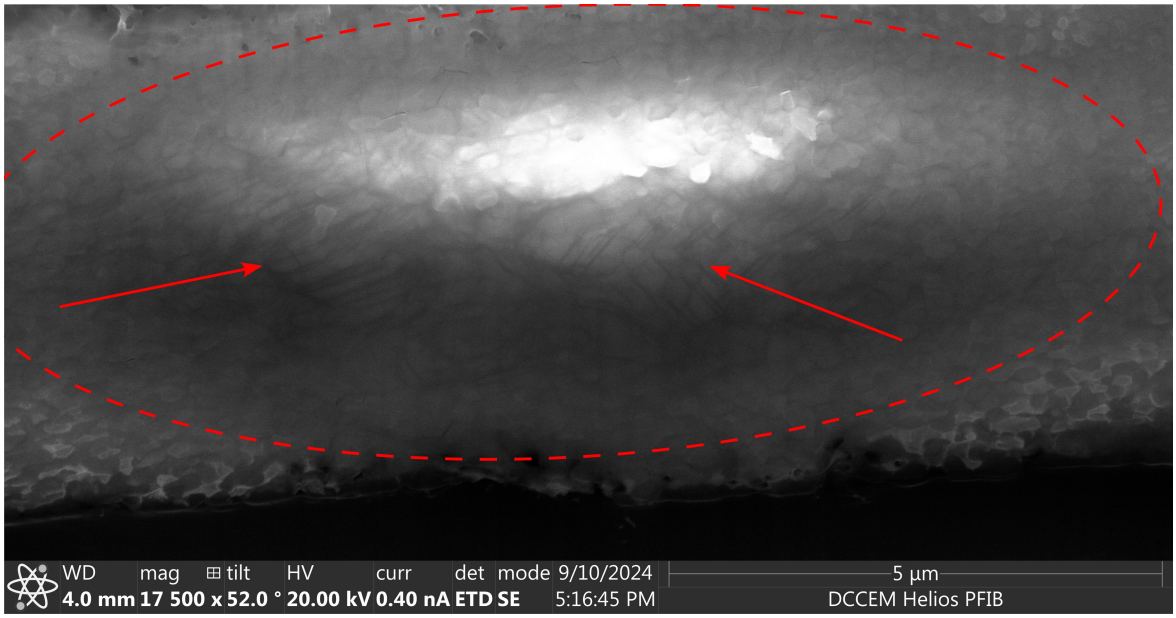

Figure D.2 Back-scattered electron image of a cross-section through spot 2, which was heated at ~2,200 K. In the centre of the hot-spot (dashed oval) the sample has recrystallized to bridgmanite with a larger grain size and changes in microstructure (indicated by arrows). Ferropericlase is only present in the rim of the heating spot (brighter grains).

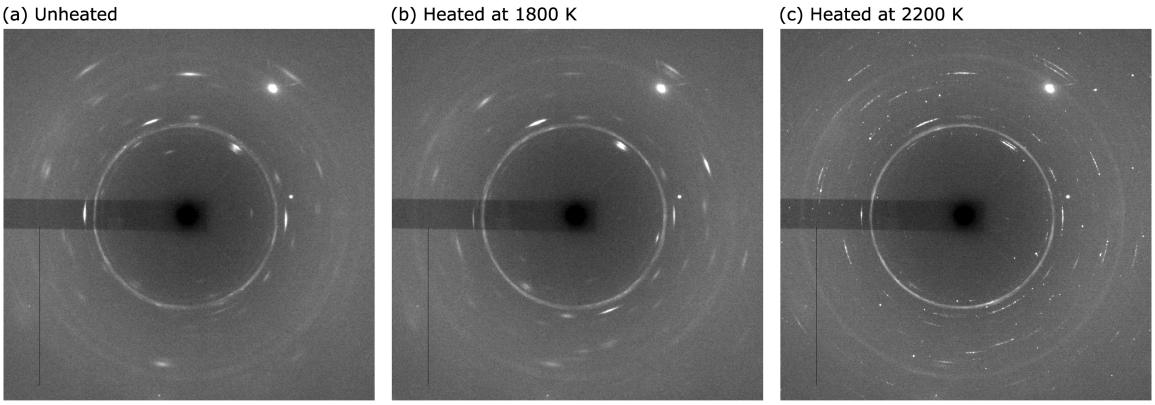

Figure D.3 Diffraction images of the sintered polycrystalline aggregate of bridgmanite and ferropericlase in KCl at 73.5 GPa. (a) Unheated area of the sample, showing diffraction rings with some texturing. (b) Area of the sample quenched from 1,800 K, showing no signs of recrystallization. (c) Area of the sample quenched from 2,200 K. The sample has become more textured (i.e. clearly distinguishable diffraction spots are visible), indicating recrystallization.

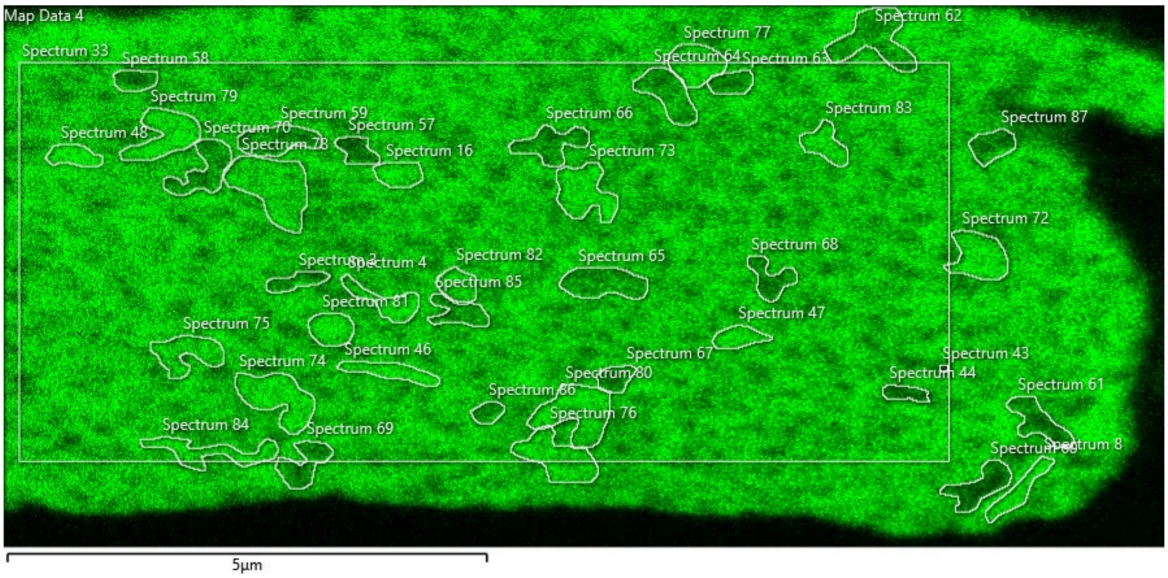

Figure D.4 X-ray map for Si of a cross-section of spot 1, showing the Si-rich and Si-poor regions for which elemental abundances were determined from EDS spectra, to constrain iron-partitioning between bridgmanite and ferropericlase. A total of 39 spectra were computed; spectrum 33 indicates the area from which the average composition of the sample was determined.

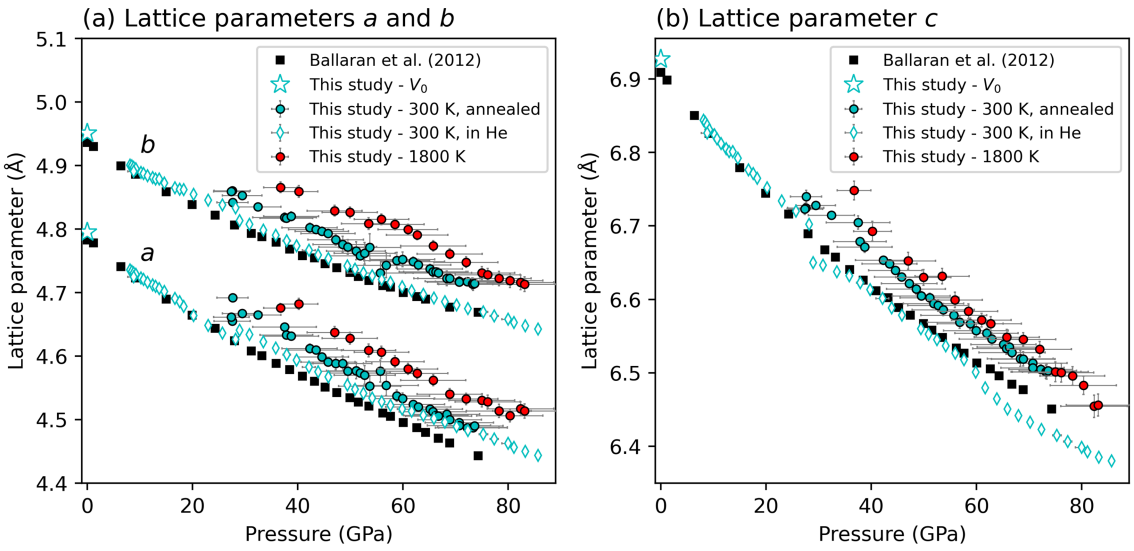

Figure D.5 Unit-cell lattice parameters (a) *a*, *b*, and (b) *c* of bridgmanite in the two-phase sample. Data collected at 300 K for cell RT1 with helium as pressure medium and no laser-annealing is shown with open diamonds. Data from cell LH1 are shown as blue and red filled circles, corresponding to measurements at 300 K with annealing and measurements at 1,800 K, respectively. The open star indicates ambient conditions in air. Data for single-crystal $(Mg_{0.96}Fe_{0.04})SiO_3$ (Ballaran et al., 2012) is also shown.